Elastic Photoproduction of J/ψ at the H1 Experiment at HERA

By

George Franklin Pope

B.A. (University of California, Berkeley) 1990

DISSERTATION

Submitted in partial satisfaction of the requirements for the degree of

DOCTOR OF PHILOSOPHY

in

Physics

in the

OFFICE OF GRADUATE STUDIES

of the

UNIVERSITY OF CALIFORNIA

DAVIS

Approved:

. . . .

. . . .

. . . .

Committee in Charge

March 1997

Abstract

A complete analysis of the elastic photoproduction of J/ψ is presented, using $2.7\,\mathrm{pb}^{-1}$ of data in the dileptonic decay modes of the J/ψ. Using a custom analysis program, a selection of low-multiplicity J/ψ events is extracted and the elastic cross section computed as a function of the photon-proton center-of-mass energy $W_{\gamma p}$. The resulting photoproduction cross section of $\sigma_{\gamma p} = 69.2 \pm 6.2 \pm 12.4\,\mathrm{nb}$ for the range $40\,\mathrm{GeV} < \mathrm{W}_{\gamma\mathrm{p}} < 200\,\mathrm{GeV}$ is inconsistent with the Vector Meson Dominance model. A new model using perturbative QCD is successful in describing the fast rise in the cross section with $W_{\gamma p}$. The t distribution for the elastic data is also examined, and is found to be consistent with a diffractive production mechanism, with a slope of $3.67 \pm 0.39 \pm 0.15\,\mathrm{GeV}^{-2}$, in general agreement with lower-energy data.

For my parents.

Thank you for everything.

Acknowledgements

We are grateful to the HERA machine group whose outstanding efforts made this experiment possible. We appreciate the immense effort of the engineers and technicians who constructed and maintained the detector. We thank the funding agencies for their financial support of the experiment. We wish to thank the DESY directorate for the support and hospitality extended to the non-DESY members of the Collaboration.

Contents

List of Tables

List of Figures

Chapter 1

Introduction

In 1974, in what was later to be called the November Revolution, two independent teams of physicists, one at SLAC, the other at Brookhaven, made the discovery of a fundamentally new kind of particle. This particle was called ‘J’ by the team at Brookhaven [1], and ‘psi’ by the Stanford [2] experimenters. Now known as the J/ψ, the particle was the first evidence for a new property of matter called charm. Four years earlier, theorists [3] had proposed the existence of a new quark, the charm quark, as an addition to the set of three previously known quarks, called up, down, and strange. The discovery of the J/ψ, determined to consist of a charm quark and an anti-charm quark in a bound state, confirmed the validity of this new theoretical concept.

The J/ψ has a mass of $3.097\,\mathrm{GeV/c^2}$ (we can adopt a system of measurement in which $c = 1$ so that mass and energy both have units of GeV) and a lifetime of about 10^{-20} sec. Its relatively large mass is due to the charmed quark being quite heavy, heavier in fact than a proton if one assumes that the quarks share the entire J/ψ mass. One of the early mysteries of the J/ψ was its lifetime, which, compared to other resonances like the ρ, is 1000 times that which was expected. The reason for this is that the J/ψ has very few options for decaying via the strong force, as shown in Figure 1.1. It is not massive enough to break into a pair of charmed mesons forming, for example, a D^+D^- state. The J/ψ cannot decay through one gluon, as it is colorless, and gluons are colored objects. It is also forbidden to decay through two gluons, or any even number of gluons, due to charge conjugation. The J/ψ can decay by converting into three gluons. However, this is a so-called Zweig-suppressed mode of decay. These are processes in which the associated diagram can be split into two pieces simply by cutting across gluon lines. Each gluon emission multiplies the probability of the process by the strong coupling constant, which is small (about 0.2) for the high mass scale of the charm quarks. Thus, the J/ψ lives for an unusually long time, between the electromagnetic and strong time scales.

The J/ψ also decays electromagnetically (see Figure 1.1e), when the charm and anti-charm quarks annihilate each other. This annihilation often results in an electron-positron pair or a muon-antimuon pair. Many experiments, including this work, focus on these decay modes as easily distinguished signatures of a J/ψ. Another option that the J/ψ has is for its charm quarks to decay. Like the strange quark, the charm quark is unstable and quickly decays into a lower-mass quark, in

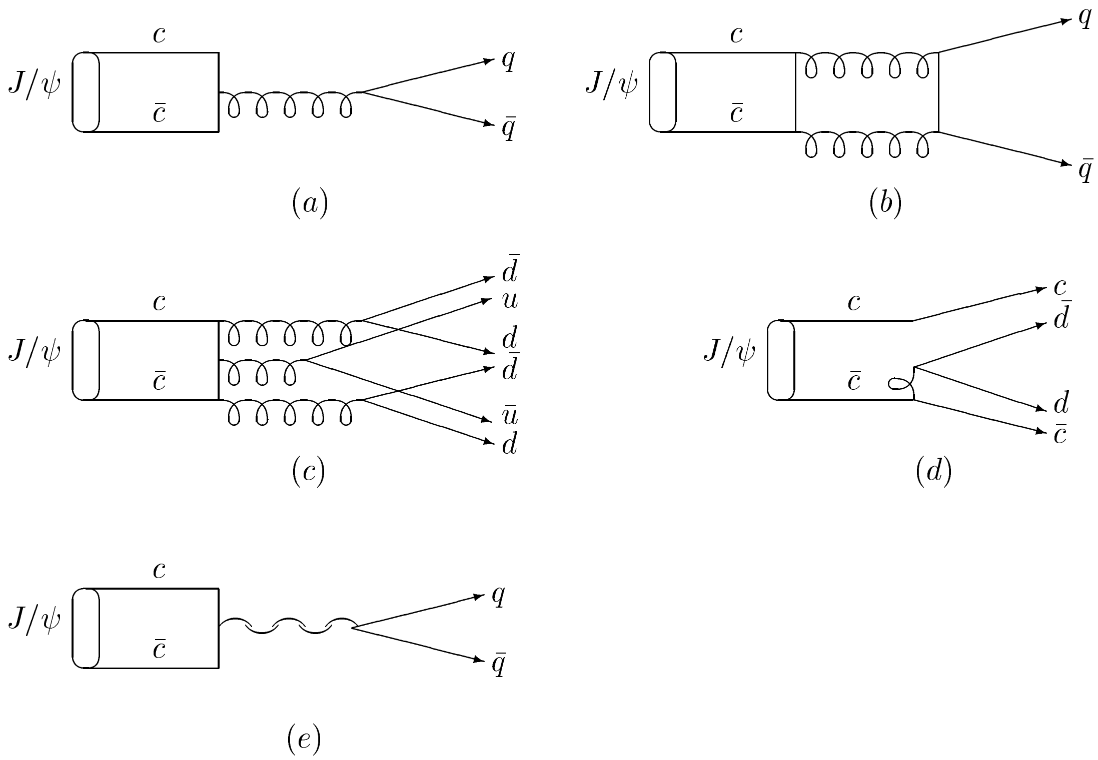

Figure 1.1: J/ψ decay via: (a) one gluon (forbidden by color); (b) two gluons (forbidden by charge conjugation); (c) three gluons (Zweig-suppressed); (d) D^+D^- production (forbidden by energy); (e) one photon (allowed).

this case the strange quark. However, this process is due to the weak force, and is much slower than any other process.

Although the J/ψ can be produced in any general hadron-hadron or electron-positron collision, of special interest is the photoproduction of J/ψ, where a nearly-real photon interacts with a proton or heavier nucleus. Aside from the basic appeal of studying the transition from a massless particle to one with large mass, there is also a case to be made for usefulness of events. A J/ψ may be created by any of a large number of decay or production mechanisms in a symmetric collision, whereas in a photoproduction experiment the vector mesons are much more likely to have resulted from a photon-proton interaction in which the kinematic variables are both reconstructible and in regions of interest. Experiments in the past have used broad-band photon beams on fixed targets [4, 6, 7, 8], and high-energy muon beams which interact with fixed targets via quasi-real photons [9, 10, 11, 12, 13, 14, 15]. One drawback that all of these experiments share is that the center-of-mass energy available in fixed-target experiments is considerably less than that from colliding beams of comparable energies.

The HERA collider offers a unique opportunity to study J/ψ photoproduction. With a proton beam of 820 GeV and an electron beam of 26.7 GeV, a center-of-mass energy of about 300 GeV is available, allowing the investigation of the structure of the proton on previously unexplored scales. HERA also has provided luminosities on the order of $10^{30}\,\mathrm{cm}^{-2}\,\mathrm{sec}^{-1}$, necessary for measuring the small photoproduction cross section of the J/ψ. Given this luminosity, even cross sections as low as 1 nb yield production rates on the order of one per hour.

Chapter 2

Kinematics

A fairly standard nomenclature for deep-inelastic scattering (DIS) will be used throughout this work. The reaction being studied is

$$e(k) + p(p_p) \rightarrow e(k') + p(p'_p) + J/\psi(p_{J/\psi}) \tag{2.1}$$

where k, k', p_p, p'_p, and $p_{J/\psi}$ are the respective four-momentum vectors (see Figure 2.1). Note that, for most purposes, we can express the J/ψ production mechanism as a two-step process described by the equations

$$e(k) \rightarrow e(k') + \gamma(q) \tag{2.2}$$

and

$$\gamma(q) + p(p_p) \rightarrow J/\psi(p_{J/\psi}) + p(p'_p). \tag{2.3}$$

It is the second process that is the focus of theoretical and experimental attention, and the reason for the term 'photoproduction'. The first reaction is understood as a simple QED process. q is the four-momentum of the photon emitted by the electron, given by

$$q = (k - k'). \tag{2.4}$$

The electron vertex of Eq. 2.2 is described by the variables y and Q^2, defined by

$$y = \frac{p_p \cdot q}{p_p \cdot k} = \frac{E_e - E_e'}{E_e} \tag{2.5}$$

and

$$Q^2 = -q^2 \tag{2.6}$$

which, after much algebra, reduces to

$$Q^2 = 4kk' \sin^2(\theta/2) \tag{2.7}$$

In this equation θ is the scattering angle of electron. Note that Q^2 will always be a positive quantity.

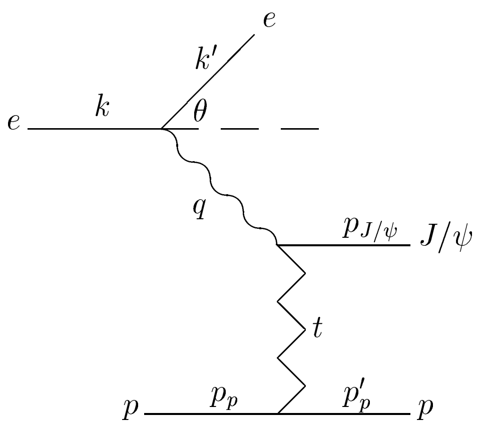

Figure 2.1: Feynman diagram for J/ψ production showing four-momenta.

The center-of-mass energy of the electron-proton system is given by

$$s = (k + p_p)^2 = m_e^2 + m_p^2 + 4E_pE_e \simeq 4E_pE_e, \tag{2.8}$$

a constant for fixed beam energies. The center-of-mass energy of the photon-proton system is also a useful variable. It is given by

$$W_{\gamma p}^2 = (q + p_p)^2, \tag{2.9}$$

which reduces to the form

$$W_{\gamma p}^2 = m_p^2 - Q^2 + 2E_p(E - p_z)_{J/\psi}. \tag{2.10}$$

If the scattered electron does not appear within the detector, we can assume that Q^2 is small enough to be safely dropped from this equation. Thus $W_{\gamma p}$ can be measured for every J/ψ event in the detector.

Reconstruction of y and Q^2 can be performed by means of the Jacquet-Blondel method [19]:

$$y_{JB} = \frac{\sum_i (E - p_z)_i}{2E_e} \tag{2.11}$$

and

$$Q_{JB}^2 = \frac{(\sum_i p_{x_i})^2 + (\sum_i p_{y_i})^2}{1 - y_{JB}}, \tag{2.12}$$

where the sum runs over all observed final state hadrons. The Jacquet-Blondel method works well for DIS events. For elastic photoproduction, however, there are no observed final state hadrons. Therefore we must rely on the scattered electron for computing these variables. If the electron is not detected due to the scattering angle being small, then Q^2 is small (less than $4\,\mathrm{GeV}^2$) and we can get an approximate value for y using $W_{\gamma p}$:

$$W_{\gamma p}^2 \simeq 2E_p(E - p_z)_{J/\psi} \simeq 4E_pE_ey. \tag{2.13}$$

Thus we have

$$y \simeq \frac{W_{\gamma p}^2}{s}. \tag{2.14}$$

We can describe the proton vertex (see Figure 2.1) by means of the four-momentum transfer variable t, defined by

$$t = (p_p - p_p')^2, \tag{2.15}$$

or, equivalently,

$$t = (q - p_{J/\psi})^2. \tag{2.16}$$

For low-Q^2 events, t is approximated by the p_t^2 of the J/ψ. This can be seen by using

$$q = (E_\gamma, 0, 0, -E_\gamma) \tag{2.17}$$

and applying E, p_t, and p_z conservation in the photon-proton system, yielding

$$E_\gamma \simeq \frac{(E - p_z)_{J/\psi}}{2}. \tag{2.18}$$

Substituting this equation into the expression for t, one arrives at the aforementioned approximation. For high-Q^2 events, the electron is typically seen in the detector, giving the four-vector q and allowing t to be computed exactly.

The variable x is also used to describe the proton vertex. There are several different definitions of this variable. Bjorken x,

$$x_B = \frac{Q^2}{2p_p \cdot q}, \tag{2.19}$$

is a scale variable first constructed by Bjorken in order to describe the q^2 behavior of the proton form factors in deep-inelastic scattering. [28] His reasoning was that the form factors must remain finite even as q and E_γ become arbitrarily large. Therefore, they must depend only on their ratio, which remains finite. This assumption has been proven to be valid over a large range of q^2. Bjorken's scaling hypothesis fit well with Feynman's parton model, in which particles could be thought of as collections of smaller objects called partons, each having a fraction of the particle's 4-momentum. For high-momentum collisions and fragmentation, the transverse components of the partons' momenta can be neglected. Thus, he defined Feynman x as [27]

$$x_F = \frac{p_z}{p_z(max)}. \tag{2.20}$$

The connection between Bjorken-x and Feynman-x is made when one considers the scattering between a lepton and one of the constituent partons of the proton. In that case we have [28]

$$(xp_p + q)^2 = m_{scat}^2 \simeq 0, \tag{2.21}$$

which expands to

$$x^2 m_p^2 + q^2 + 2xp_p \cdot q \simeq 0. \tag{2.22}$$

If the quantity $x^2 m_p^2$ is much smaller than q^2, then we can drop it and recover the definition of Bjorken-x. Thus the parton model implies scaling behavior. In the spirit of partons, we can also define a parton x

$$x_{I\!P} = \frac{(p_p - p_p') \cdot q}{p_p \cdot q}, \tag{2.23}$$

which is a scale variable for the photon-proton system analogous to y for the electron-proton system. It gives the momentum fraction of the parton (a pomeron in this case) involved in the scattering process. We can see the relationship between $x_{I\!P}$ and x_B by considering the center-of-mass energy of the photon-parton system, denoted by

$$\hat{s} = (q + x_{I\!P} p_p)^2 = -Q^2 + 2x_{I\!P} q \cdot p_p + x_{I\!P}^2 m_p^2. \tag{2.24}$$

The last term is small in almost all cases and can be safely dropped. Rearranging, we obtain

$$x_{I\!P} = \frac{\hat{s} + Q^2}{2p_p \cdot q}. \tag{2.25}$$

Also note that for small Q^2, the formula for $\hat{s}$ can be reworked to give

$$\hat{s} = s x_{I\!P} y, \tag{2.26}$$

a compact summary of the reaction. Usually, it is Bjorken x that appears in parton distribution functions, which give the probability of finding a given parton at a given momentum fraction x_B. These distribution functions are used in many cross section calculations. However, in some specific cases, another of the x definitions will be used. This is generally motivated by issues of kinematic reconstruction. Given the close relationship between the various definitions of x, the distinctions between them can usually be safely ignored by the reader.

Finally, we define the elasticity of each J/ψ event as

$$z = \frac{p_p \cdot p_{J/\psi}}{p_p \cdot k} = \frac{(E - p_z)_{J/\psi}}{2E_e y}, \tag{2.27}$$

with $z = 1$ being completely elastic. Inelastic processes will have a z somewhere between 0 and 1. Note that if the scattered electron is not seen in the detector, then the only way to obtain y is via the Jacquet-Blondel method or from $W_{\gamma p}$, and if $W_{\gamma p}$ is used the equation is reduced to $z = 1$.

Chapter 3

Theoretical Models of Photoproduction

As with other vector mesons, the photoproduction of the J/ψ involves the exchange of a pomeron, an entity carrying the quantum numbers of the vacuum. The exact nature of the pomeron is still a question open to discussion. Traditionally it has been considered a discrete particle, a constituent of the proton with measurable parton density. This is the so-called soft pomeron. However, there have been several attempts recently to model the pomeron as a digluon or gluon ladder. These QCD-inspired models, of course, are not useful for low-energy calculations. However, the relatively large mass of the charm quark sets the scale of J/ψ production high enough that perturbative QCD methods may be applied. Models using a gluonic, or hard, pomeron require as an input to their calculations the gluon density of the proton. Given the high proton beam energy, even a gluon carrying the entire mass of the J/ψ will have a value of x below 10^{-2}. Thus the perturbative QCD models directly connect J/ψ photoproduction with the low-x behavior of the gluon density of the proton, which is itself an active area of study at HERA.

3.1 J/ψ production mechanisms

In this study we are concerned with the elastic photoproduction of the J/ψ. However, photoproduction is a diffractive process, of which the purely elastic case is not the only component. It is important to remember that processes in which either the photon or the proton, or both, dissociate can fake an elastic event if the remnants do not register in the detector, escaping down the beam line, for example. The same is true of hard inelastic models, but the chance of contamination is much less because the momentum transfer is usually large enough to kick the remnants into the detector.

3.1.1 VMD

The vector meson dominance model (VMD, also seen as VDM) has been very successful in describing photoproduction cross sections [20] at the lower energies of previous experiments. It describes the process as shown in the diagrams of Figure 3.1. The main hypothesis of VMD [21] is that the electromagnetic matrix element is related to the hadronic matrix element as follows:

$$< A|j_\mu|p >= (\frac{1}{f})(\frac{m^2}{m^2 + Q^2}) < A|J_\mu|p >, \tag{3.1}$$

where $|A>$ is any hadronic state, $|p>$ is the initial proton state, and j_μ and J_μ are the electromagnetic current density and the J/ψ source density, respectively. The symbols m and f are the mass of the vector meson and a constant specific to that vector meson, respectively. The quantity

$$\frac{m^2}{m^2 + Q^2} = \left(1 + \frac{Q^2}{m^2}\right)^{-1}, \tag{3.2}$$

squared, represents the probability amplitude of the photon to fluctuate into a vector meson.

The reaction is completed with a Regge description [22] of hadronic elastic scattering. Using the additive quark model [23], the scattering amplitude is constructed from those of well-measured processes such as $\pi^+ p \to \pi^+ p$ and $\pi^- p \to \pi^- p$.

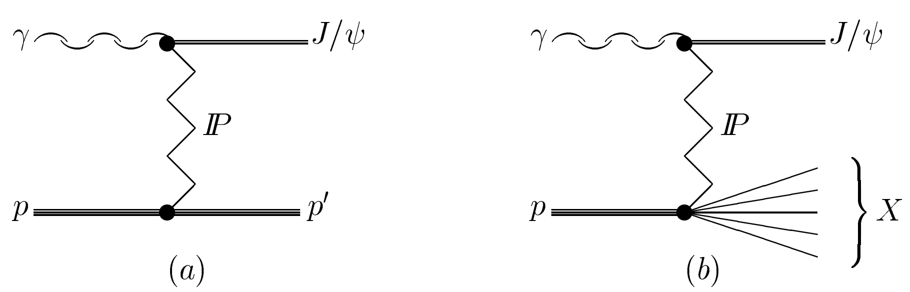

Figure 3.1: The vector meson dominance (VMD) description of a) elastic and b) proton dissociative J/ψ photoproduction.

VMD makes several predictions about the photoproduction process. Namely, it predicts a cross section which rises slowly with the center-of-mass energy:

$$\sigma_{elas} \sim \frac{s^{2\epsilon}}{b} \sim \frac{W_{\gamma p}^{4\epsilon}}{b}, \tag{3.3}$$

where ϵ can be obtained from either calculation [24] or by fits to lower-energy data [25], both of which give a value for ϵ of about 0.08. The parameter b appears in the differential cross section

$$\frac{d\sigma}{dt}(t=0) \sim e^{-bt} \tag{3.4}$$

and is predicted to have a slow variation with the center-of-mass energy:

$$b = b_0 + 2\alpha' ln\left(\frac{s}{s_0}\right), \tag{3.5}$$

where α' is taken to be $0.25\,\mathrm{GeV}^{-2}$. This effect is known as shrinkage. As b increases, the t distribution becomes sharper and 'shrinks' towards $t = 0$. An interesting comparison is to consider the classical picture of elastic scattering off a black disk [26]. Using the method of partial waves, we get (to first order):

$$\frac{d\sigma}{dq^2} \simeq \frac{\pi R^4}{4} e^{\frac{-R^2 q^2}{4}} \tag{3.6}$$

where q^2 is the momentum transfer (equivalent to t), and R is the radius of the black disk. Thus we see that the parameter b is proportional to the square of the classical radius of the target, and as b grows with energy, so does the radius.

A prediction for the elastic J/ψ photoproduction cross section may be obtained from VMD by projecting the fit to low-energy data up to HERA energies. At a $W_{\gamma p}$ of 100 GeV, the model gives a cross section of 33 nb.

3.1.2 Perturbative QCD

One of the most recent attempts [29] in using perturbative QCD (PQCD) makes use of the leading-log approximation (LLA), in which all possible gluon ladder diagrams are considered. This is in contrast to theories that model the pomeron as a two-gluon exchange, which can be done rigorously in perturbative QCD [30]. A diagram for the perturbative process is shown in Figure 3.2.

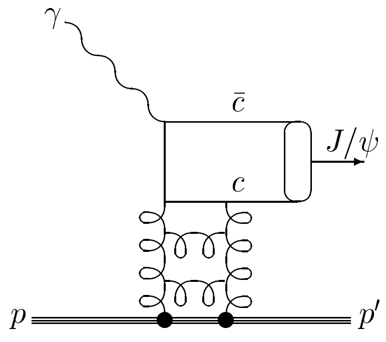

Figure 3.2: J/ψ photoproduction via a gluon ladder as described by perturbative QCD (PQCD) models.

The distinctive feature of the PQCD models is that they connect the cross section with the gluon distribution of the proton:

$$\sigma_{elas} \sim [xG(x, Q^2)]^2, \tag{3.7}$$

with the prediction that the longitudinal component of the cross section dominates. Real photons have pure transverse polarization, whereas photons with large Q^2 have a longitudinal component as well. Thus, the two-gluon model also predicts the behavior of the cross section with respect to Q^2:

$$\frac{d\sigma_L}{dt}(t=0) \sim Q^{-6}, \qquad Q^2 > m^2_{J/\psi}. \tag{3.8}$$

A recent perturbative QCD calculation [48] gives predictions for the cross section for elastic J/ψ photoproduction of 47 nb, 128 nb, and 262 nb at a $W_{\gamma p}$ of 100 GeV for the MRS(A'), GRV, and MRS(G) parton distribution sets, respectively. Therefore, although the predictive power of this model is somewhat limited by the uncertainty in the gluon distribution, it can in fact be used to distinguish between them, given a measurement of sufficient precision.

3.1.3 Color singlet model

The color singlet model [31] describes the inelastic production of J/ψ. It is discussed here both as a possible background to elastic production, and as an introduction to the open charm model. The color singlet model makes use of a process known as photon-gluon fusion (shown in Figure 3.3):

$$\gamma + gluon \rightarrow J/\psi + gluon \tag{3.9}$$

where the initial gluon comes from the proton and the final state gluon is required due to color conservation. It is this net color transfer from the proton that makes this model inelastic. There is no way that the proton can continue into the final state intact, as the proton is a colorless state and the removal of a single gluon from it leaves a colored state. The photon-gluon fusion process is calculated using perturbative QCD, which is possible due to the scale being set by the large mass of the charm quark.

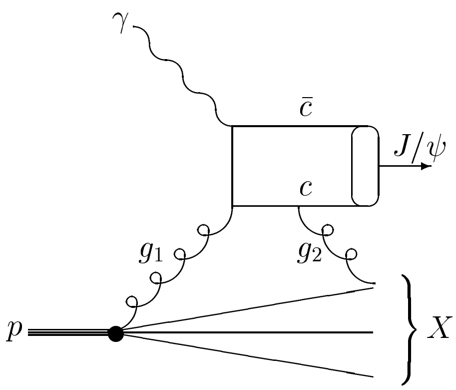

Figure 3.3: J/ψ photoproduction via photon-gluon fusion as described by the color singlet model.

The color singlet model has been reasonably successful in describing the shapes of various distributions in the inelastic J/ψ photoproduction data. However, it suffers from a normalization problem. Different normalization factors seem to be required for different experimental data sets. Note that this model also requires, like the PQCD models, the input of the gluon density of the proton.

The color singlet model predicts a fairly substantial cross section [32] of between 60 nb and 100 nb at HERA energies, depending on the input gluon density. However, due to its inelastic nature, both with the proton's forced dissociation and the emission of the hard final state gluon, this process will be heavily discriminated against in the event selection studied here.

3.1.4 Open charm model

The open charm model [33] for the elastic production of J/ψ is based on the color singlet model, with its photon-gluon fusion subprocess. However, in this case, the initial state gluon comes not from the proton, but from a pomeron emitted by the proton. Also, the final state gluon is connected back to the pomeron vertex, making the process elastic, with no net color transfer. Figure 3.4 shows a diagram for this process.

The open charm model is similar to the PQCD models described previously. However, there are some distinct differences. The main difference is that the gluons now come from a pomeron instead of a proton, requiring the input of a poorly known gluon distribution of the pomeron, or some other approximate treatment. Also, the open charm model requires a normalization factor just like its ancestors. The resulting cross section is nearly constant with energy.

Together with a model for inelastic photoproduction, the open charm model successfully describes [33] the increase of the cross section with photon energy and

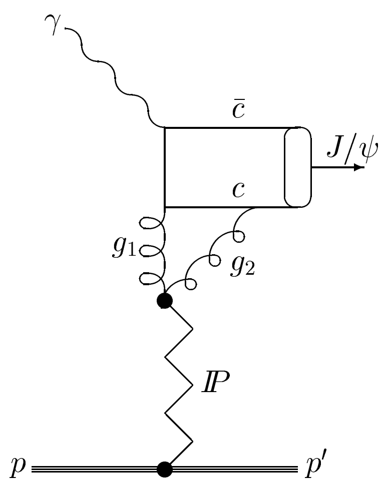

Figure 3.4: J/ψ photoproduction via photon-gluon fusion as described by the open charm model.

the z distribution in lower-energy data. However, a study of the t distribution shows that it begins to fail for t values greater than $1\,\mathrm{GeV}^2$. The open charm model gives a cross section of 5.04 nb for elastic J/ψ photoproduction at HERA energies.

3.2 Background processes

Aside from the previously mentioned diffractive and inelastic processes, the main contribution to the contamination of the elastic J/ψ sample is the QED generation of lepton pairs [34], shown in Figure 3.5. The QED process is:

$$\gamma + \gamma \to l^+ + l^-, \tag{3.10}$$

where one photon comes from the electron vertex and the other is emitted from the proton. The two-photon process is predicted to have an *ep* cross section (after acceptances) of less than 1 nb at HERA energies, which gives a photoproduction cross section within an order of magnitude of the various J/ψ production cross section predictions. However, when these events have a reconstructed mass near that of the J/ψ, they can not be distinguished from genuine elastic J/ψ production and decay into two leptons. Therefore this is expected to be a non-negligible background.

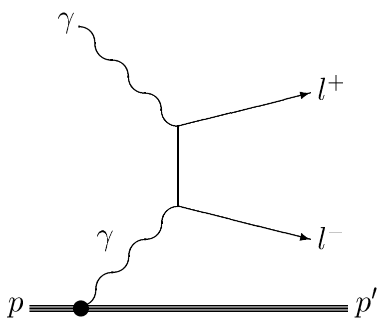

Figure 3.5: QED production of lepton pairs (l^+l^-) is the major background to elastic J/ψ photoproduction.

Other processes, such as b-quark decays and resolved photon events [32], can contribute to the background. However, these have relatively small cross sections and are discriminated against by the elastic event selection.

3.3 Summary of Theories

There is a wide range of predictions, from 5 to about 50 nb (or higher depending on the choice of gluon distribution function), for the elastic J/ψ photoproduction cross section. The inelastic models have a similar uncertainty, but a strong elastic selection will reduce their contributions to background levels. The QED process will also represent a background. An understanding of these contaminations is required in order to obtain a cross section for the purely elastic photoproduction process. Such a measurement would be of value in determining which, if any, of the elastic models gives a correct description of the data, and in the case of PQCD, how the gluon distribution behaves at low x.

Chapter 4

The H1 Detector

The H1 detector is an asymmetric, cylindrical, high-hermeticity detector. Its asymmetry is due to the large difference in energy of the colliding beams. The proton beam is at an energy of 820 GeV, while the electron beam has an energy of 26.7 GeV, resulting in a center-of-mass movement in the forward (proton) direction with a gamma (energy to mass ratio) of 2.86. From the center of the detector outwards, the H1 detector consists of a drift chamber tracking system, a liquid argon calorimeter, a superconducting solenoidal magnet providing a field of 1.2 T, and an iron yoke in the form of an octagonal barrel. Figure 4.1 shows a cutaway view of the detector, while Figures 4.2 and 4.3 show side and radial views, respectively. A complete description of the H1 detector is given elsewhere [35].

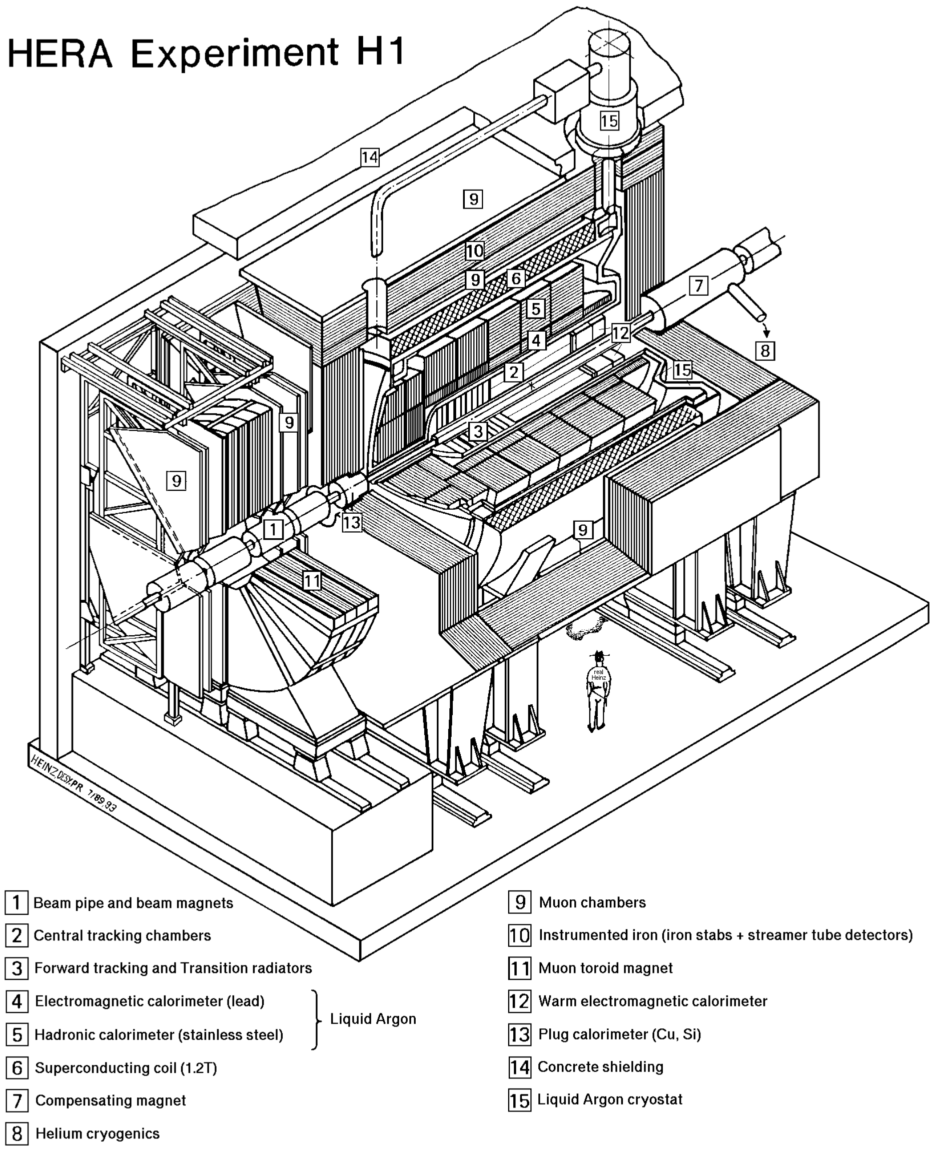

Figure 4.1: The H1 Detector at HERA - cutaway view.

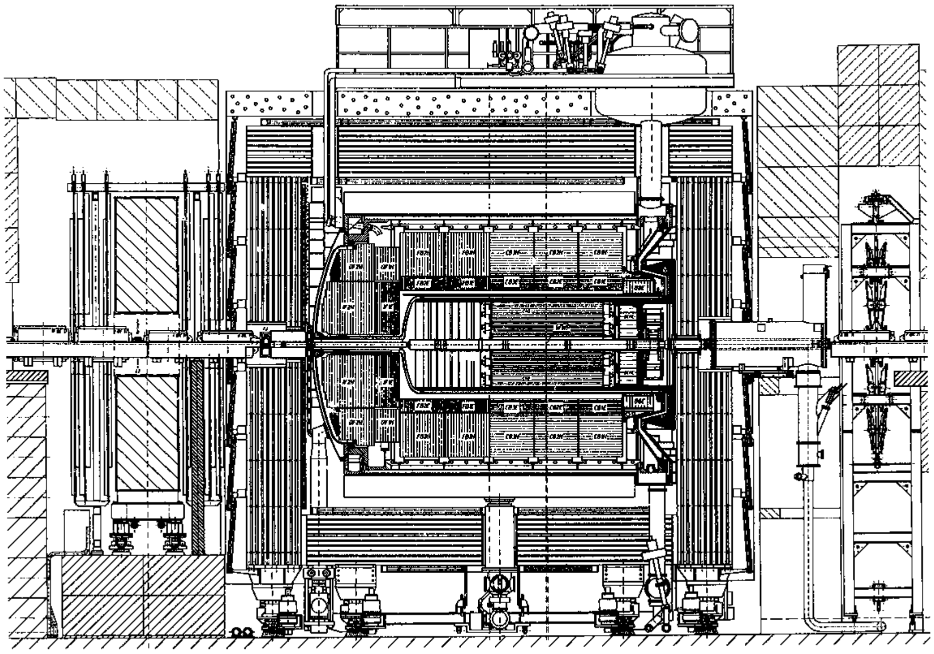

Figure 4.2: The H1 Detector at HERA - side view.

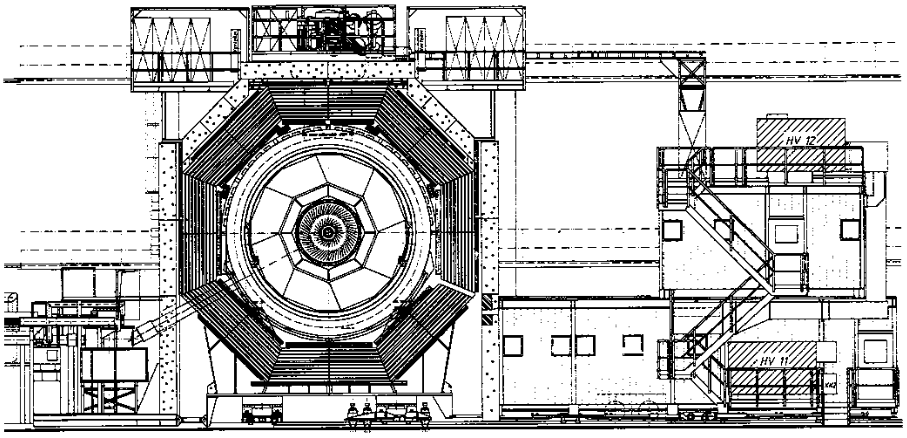

Figure 4.3: The H1 Detector at HERA - radial view.

4.1 Central and forward tracking

The drift chamber tracking system is broken into two separate detectors: the central and forward tracking detectors (CTD and FTD). These are composed of separate drift chambers and proportional chambers. Figure 4.4 shows a side view of the H1 tracking system.

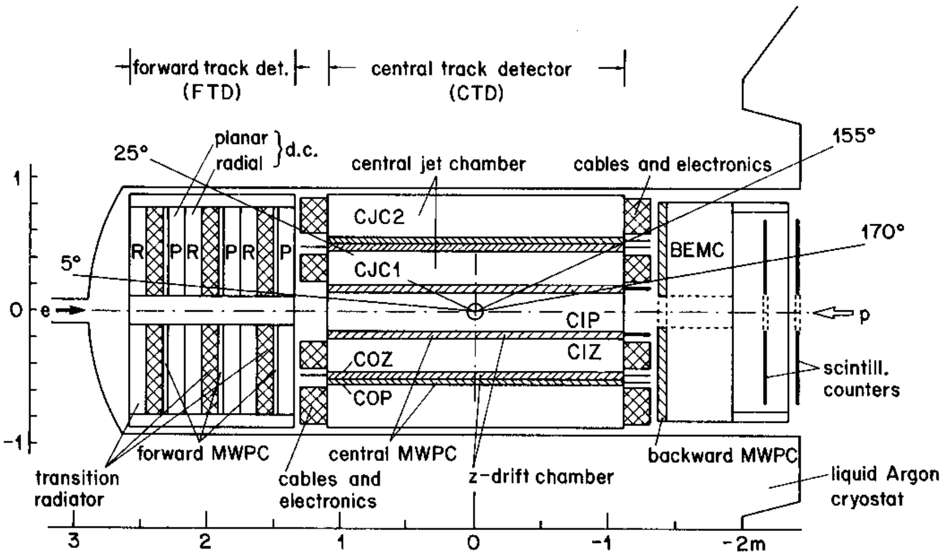

Figure 4.4: The H1 tracking system - side view.

A side view of a portion of the central tracking system is shown in Figure 4.5. The main element of the central tracking system is the central jet chamber (CJC), consisting of two large concentric drift chambers, CJC1 and CJC2, with radial cells (30 in CJC1, 60 in CJC2) containing wires running along the axial direction. CJC1 subtends the angular range of 10–170 degrees, and CJC2 covers the angular range of 25–155 degrees. However, pattern recognition and track reconstruction are poor in the very forward and very backward directions, where there are few space points. Hence the effective angular coverage of the CJC is between that of the CJC1 and CJC2. The CJC provides a spatial resolution of 170 μm in the $r-\phi$ plane, resulting in resolutions of 0.1 degrees in ϕ and $3 \cdot 10^{-5}$ in kappa, the track curvature. By using charge division, a resolution of 2.2 cm in z can be achieved.

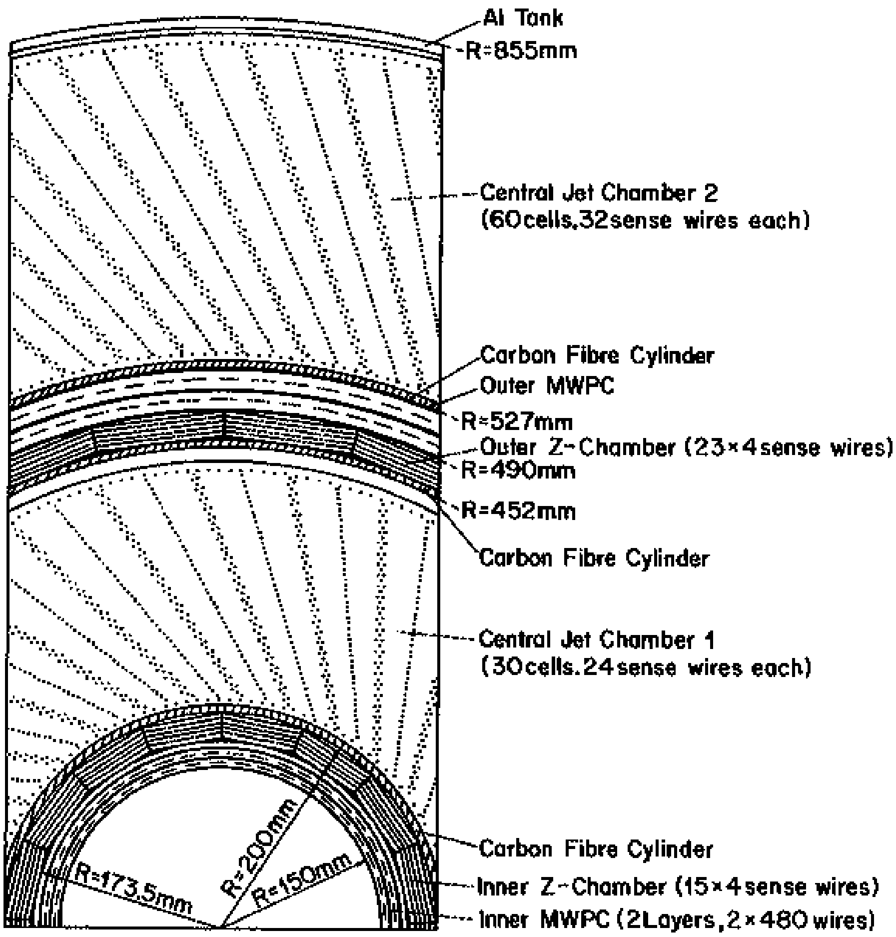

Figure 4.5: The central tracking system - radial view.

Measurement of the z coordinate is improved by two thin drift chambers, CIZ and COZ. The CIZ sits just inside CJC1, while COZ is in between CJC1 and CJC2. The CIZ (COZ) has 15 (24) rings along the z-axis, each having 16 (24) ϕ cells, as shown in Figure 4.6. With wires perpendicular to the z-axis, they have a resolution of about 300 μm in z. Using charge division, a ϕ resolution of 7.2 degrees is possible.

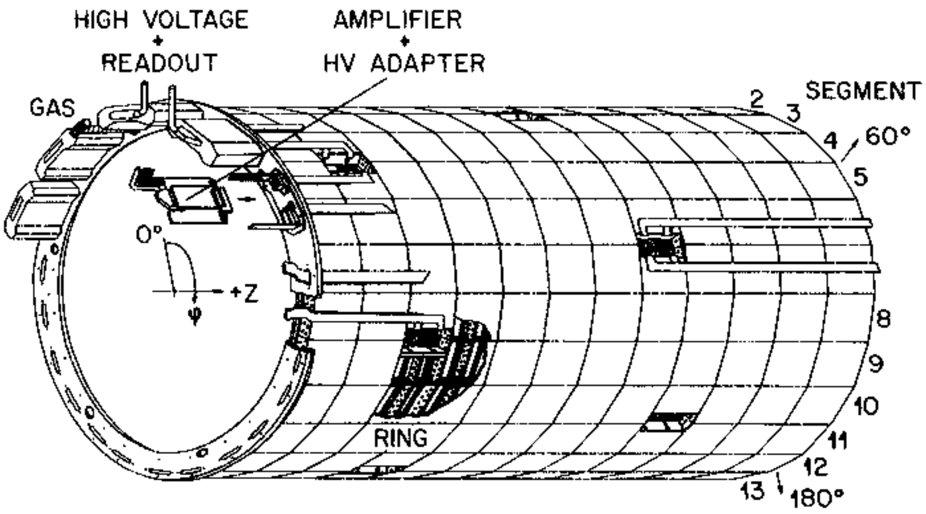

Figure 4.6: Schematic view of the COZ.

The CJC has a gas mixture of Ar-CO_2-CH_4 in the ratios of 89.5 : 9.5 : 1.0. The CIZ and COZ both have Ar-CH_4 gas mixtures, in the ratios of 80 : 20 and 50 : 50, respectively. Drift velocities for all of the drift chambers are about 50 mm/μs, which is of course too slow for triggering purposes considering the clock speed of

HERA. Bunches at HERA are spaced 96 ns apart, and a time resolution of a fraction of this is required for triggering.

Providing fast timing and supplementing the tracking system are proportional chambers. The central inner and outer proportional chambers (CIP and COP) sit just inside the CIZ, and between the COZ and CJC2, respectively. Each consists of two layers, with one anode plane and a cathode segmented into 480 (288) pads. Their gas mixture is Ar-C_2H_6-Freon (R12) in the ratio of 49.9 : 49.9 : 0.2. They have time resolutions of about 20 ns, and are used in fast track triggers.

Behind the CJC, and just in front of the BEMC, sits the backward proportional chamber (BPC). It has four anode wire planes which are rotated 45 degrees with respect to one another. This chamber does not have a segmented cathode; the anodes are read out. The BPC is used for track triggering (in a 3 out of 4 mode) and reconstruction, as the CJC is not as efficient in the very backward and very forward directions. By providing low-angle space points the BPC also allows the discrimination of electrons and photons in the BEMC. The BPC has a gas mixture of Ar-C_2H_6-R12 in the ratios of 49.9 : 49.9 : 0.2.

The forward tracking detector is composed of three supermodules, each containing planar and radial drift modules, a transition radiator, and a module of forward proportional chambers (FPCs). The arrangement of the modules is shown in Figure 4.7, and Figure 4.8 gives a detailed view of their construction. Each FPC module consists of two wire planes interleaved with three cathode planes, segmented into 384 ring-shaped pads of arclength $\pi/8$. The FPCs have a gas mixture of Ar-C_3H_8-C_2H_5OH in the ratios of $89.4 : 9.9 : 0.7$. The planar modules each have three drift chambers, with cells (32 per plane) oriented vertically and at ± 60 degrees to vertical. They have a gas mixture of Ar-C_3H_8-C_2H_5OH in the ratios of $89 : 10 : 1$, and give a single-point resolution of 150–170 μm. The radial modules have 48 sector cells covering the full 2π in ϕ, giving a resolution of 150–200 μm. They have a gas mixture of Ar-C_2H_6 in the ratio of $50 : 50$. The transition radiators consist of 400 polypropylene foils. X-rays generated by electrons passing through this detector are recorded in the radial chambers.

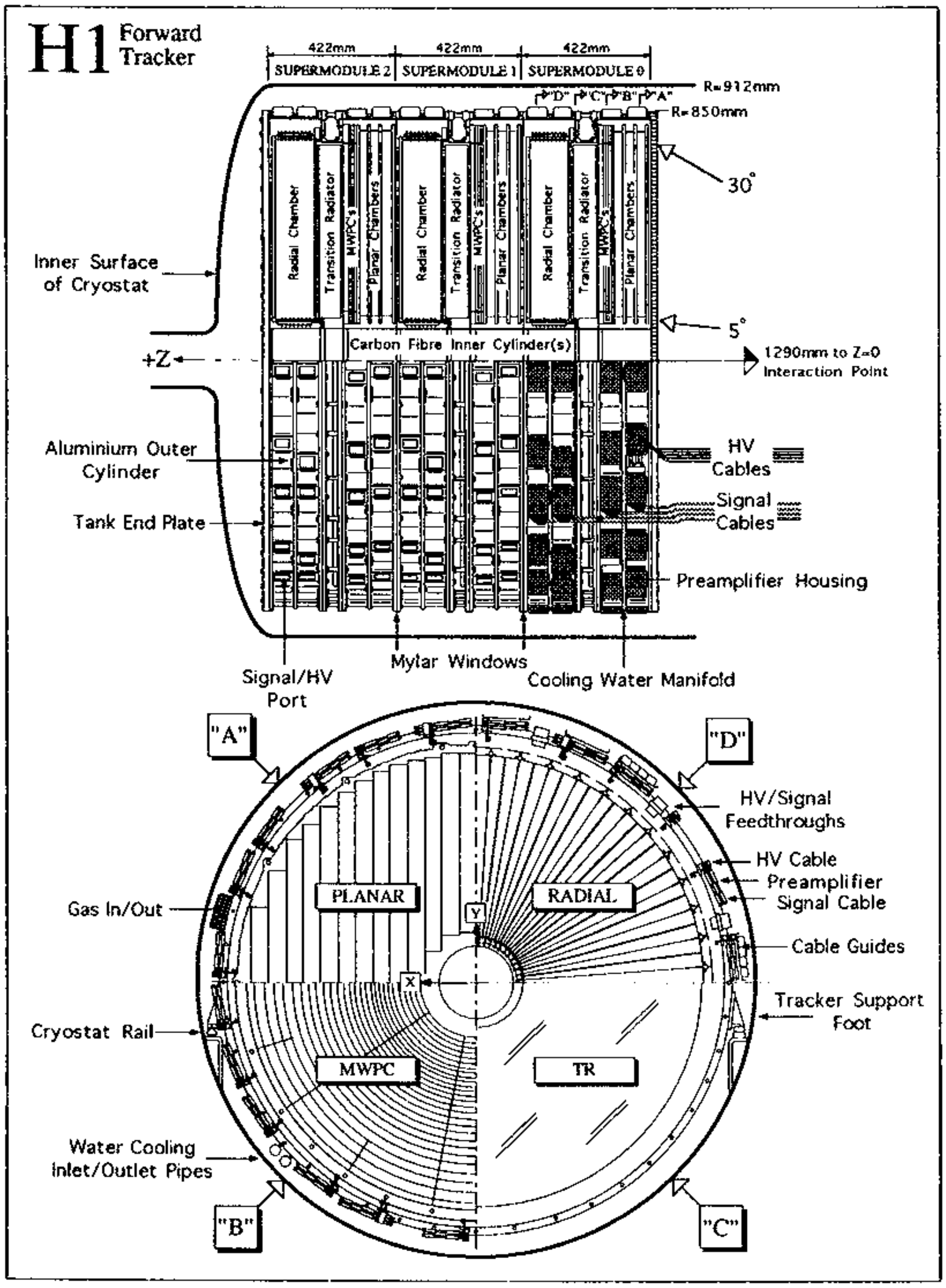

Figure 4.7: Layout of the forward tracker. Above is a side view of the supermodules, and below is a radial view showing the cell structure of the supermodule components, one per quadrant.

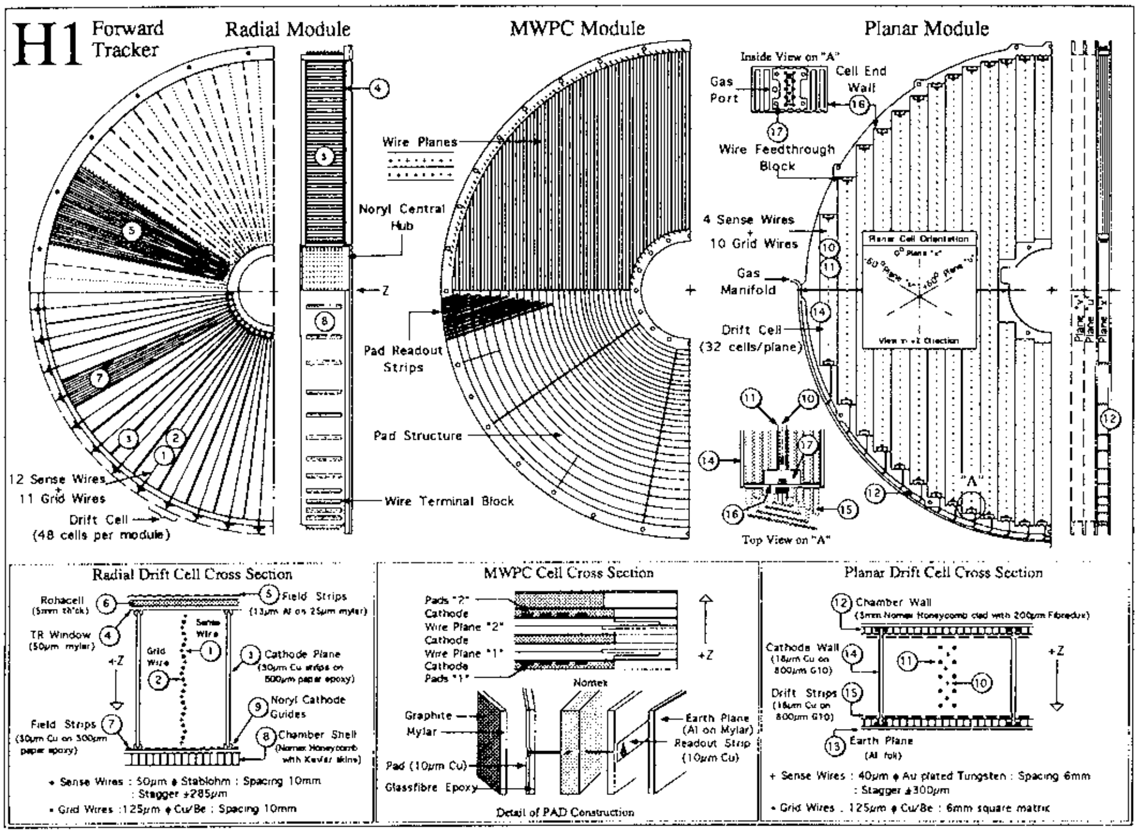

Figure 4.8: Detailed view of the construction of the supermodule components. Above are the radial and side views, and below are cell cross sections.

4.2 LAr calorimeter

The main calorimeter of the H1 detector is a fine-granularity liquid argon sampling calorimeter [36]. It sits in a cryostat which surrounds the central and forward tracking detectors, and is surrounded by the superconducting coil. The calorimeter is barrel-shaped in the central region of the detector, and closes to the beam pipe in the forward direction. It is broken into 8 wheel-like segments along the z direction, further segmented into 8 ϕ octants for those in the barrel region and two halves for the forward sections. Figures 4.9 and 4.10 show side and radial views of the calorimeter, respectively. As shown in Figure 4.11, the calorimeter has a theta-dependent thickness of between 20 and 30 radiation lengths (X_0), or between 5 and 8 attenuation lengths (λ) thick. It is segmented into towers such that each tower has a depth of about one interaction length.

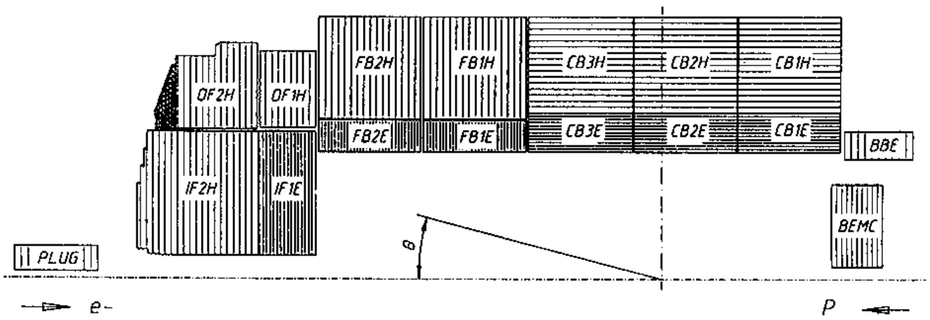

Figure 4.9: Side view of the liquid argon calorimeter showing LAr wheels, as well as plug and BEMC.

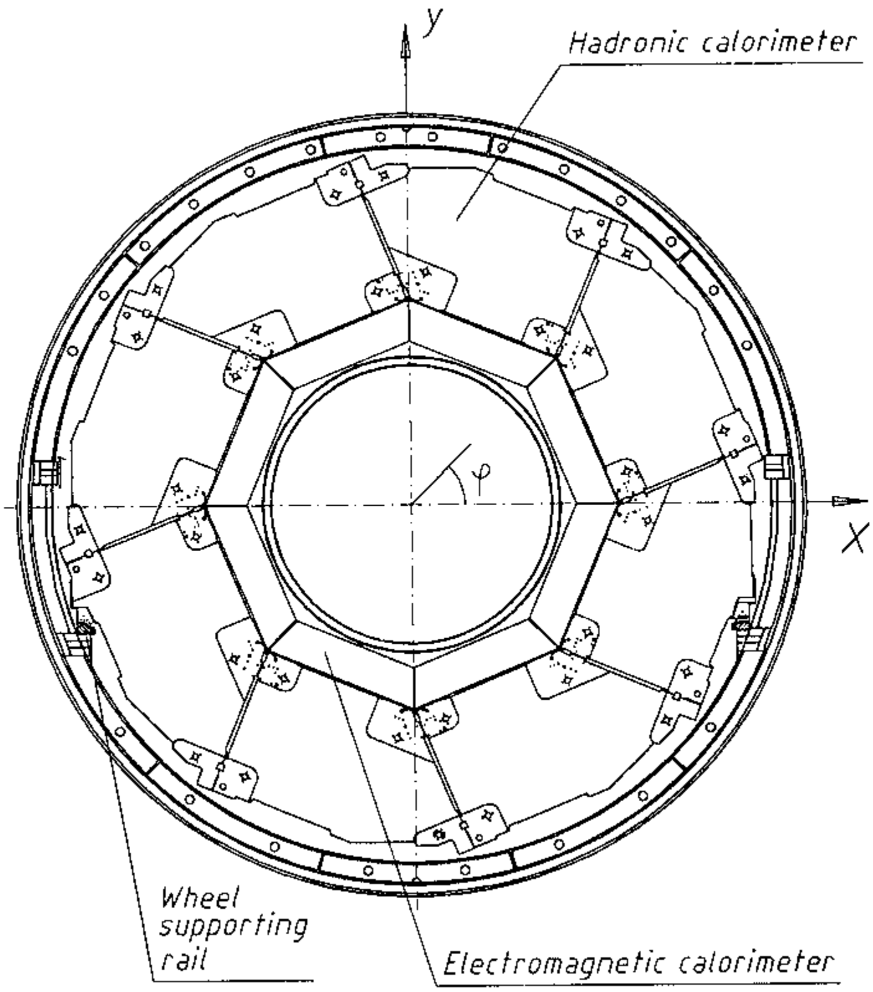

Figure 4.10: Radial view of the liquid argon calorimeter.

The LAr calorimeter has two components: an electromagnetic section and a hadronic section. The electromagnetic section consists of G10-Pb-G10 sandwiches separated by gaps of liquid argon, while the hadronic section has stacks of stainless steel plates. In the electromagnetic section, readout is achieved by copper pads alternating with high resistivity coatings (HRC) at high voltage. The hadronic

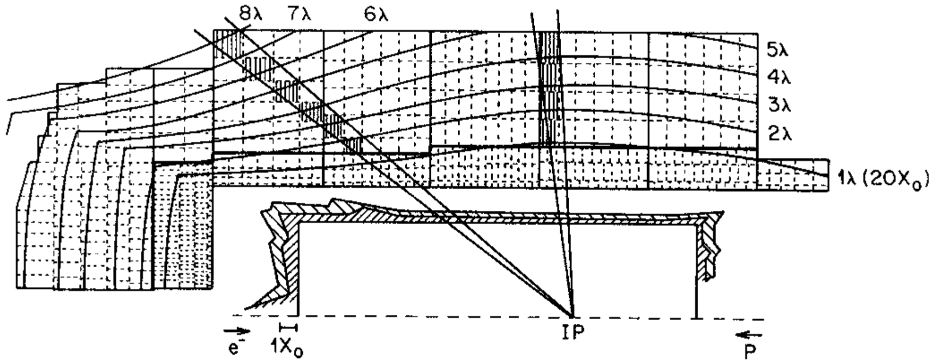

Figure 4.11: Iso-X_0 and iso-λ lines for the LAr calorimeter, including the material of the trackers and the cryostat wall (hashed areas). The dashed lines indicate the segmentation of the calorimeter.

section uses readout cells containing a G10 board with pads in the center, and HRC on the stainless steel. Figure 4.12 gives a schematic view of both types of cells. The calorimeter has about 65,000 electronic channels to be read out. Measurements using a test beam at CERN show that the calorimeter has an energy resolution of about $\frac{\sigma}{E} = \frac{11\%}{\sqrt{E}}$ for the electronic section and $\frac{\sigma}{E} = \frac{46\%}{\sqrt{E}}$ for the hadronic section.

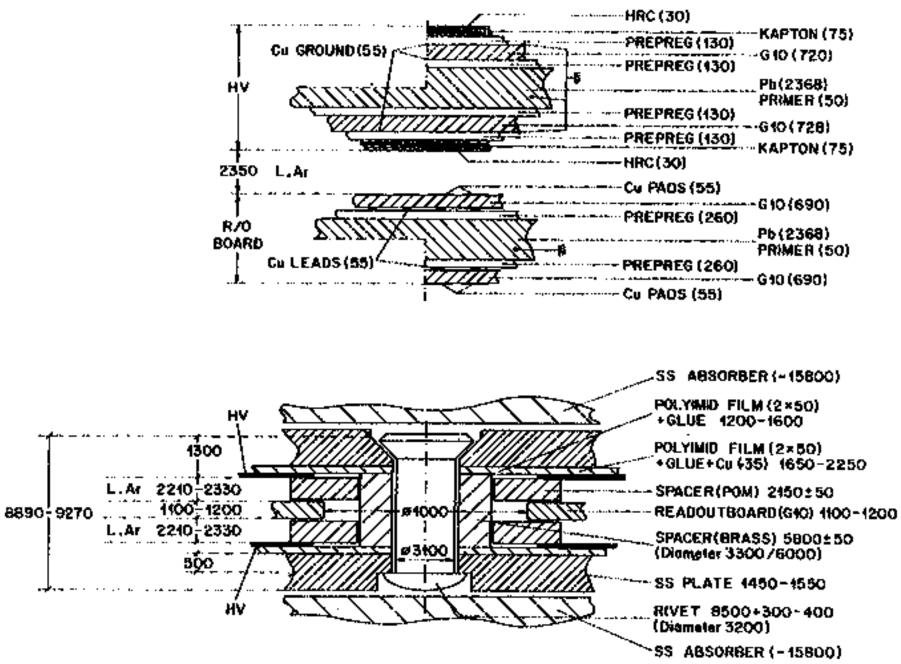

Figure 4.12: Schematic view of readout cell for electromagnetic (above) hadronic (below) sections of the LAr. All dimensions are in μm.

4.3 BEMC calorimeter

The BEMC is a lead-scintillator sandwich calorimeter [37] that sits behind (in the $-z$ direction of) the CJC, bringing calorimeter coverage in the backward direction to the beam pipe. A range of 151–176 degrees in theta is covered by the BEMC, corresponding to a pseudorapidity range of -1.6 to -2.9. As shown in Figure 4.13, the BEMC is barrel-shaped, and segmented into 88 stacks of mostly square cross-section, with stacks on the periphery of trapezoidal or triangular shape to match the circular perimeter. The stacks consist of 50 layers of SCSN-38 scintillator alternating with 2.5 mm plates of lead, giving a depth of 21.7 radiation lengths. Scintillation light passes through wavelength shifters running along the length of the stack into Hamamatsu S2575 photodiodes for readout. The BEMC has 472 readout channels. It has an energy resolution of about $\frac{\sigma}{E} = \frac{10\%}{\sqrt{E}}$.

4.4 Plug

The plug calorimeter is a Cu-Si calorimeter that sits forward of the FTD, filling the gap between the inner forward wheel of the LAr and the beampipe. It covers a range in theta of 58 mrad to 12.5 degrees. The plug is an octagonal barrel, and contains up to 8 planar modules (5 in 1994) consisting of a Cu-G10-Cu sandwich broken into a top and bottom half. This is shown in Figure 4.14. Each G10 readout board holds 42 silicon detectors of primarily square shape, with triangular and

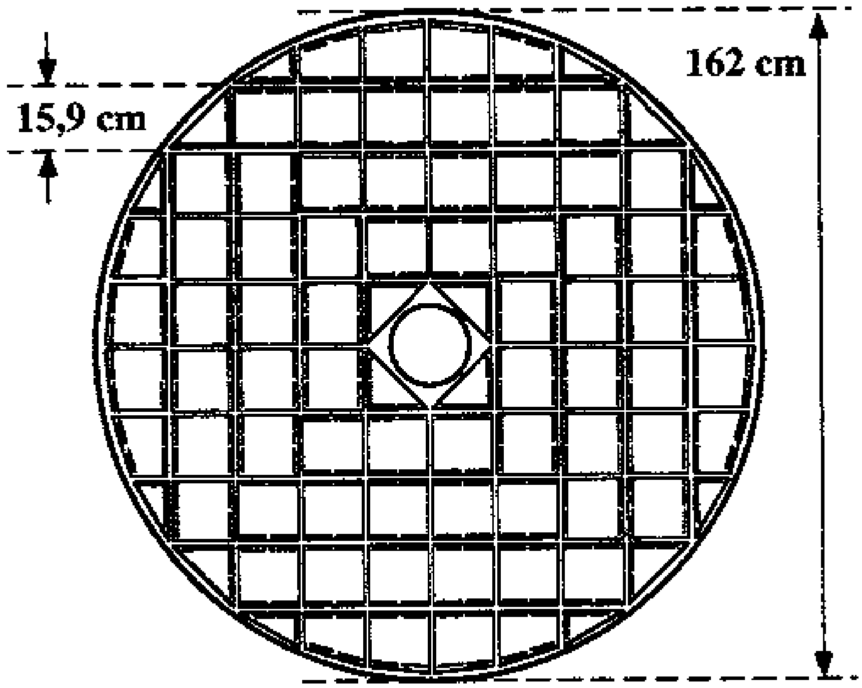

Figure 4.13: Radial view of the BEMC.

rectangular detectors at the edges. The detectors of the final two planes of the plug are combined into towers, so a total of 336 channels are read out. The plug has an energy resolution of about $\frac{\sigma}{E} = \frac{150\%}{\sqrt{E}}$.

4.5 Instrumented iron

The iron yoke is in the form of an octagonal barrel, composed of 10 layers of iron separated by gaps. This is shown in Figure 4.15. There are octagon-shaped caps at both ends with the same laminar structure. Within the gaps are modules of eight

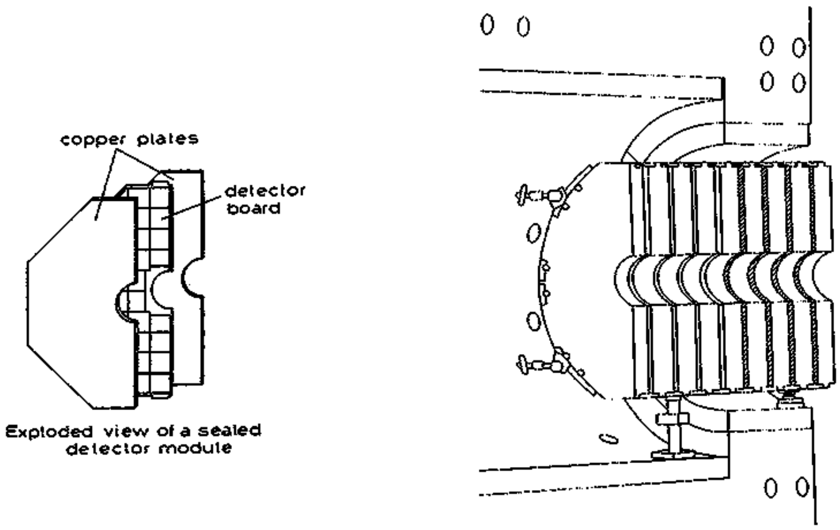

Figure 4.14: View of the plug calorimeter, showing exploded view of single module (left), and entire subdetector (right).

limited streamer tubes (LSTs) composed of u-shaped extruded Luranyl coated with low-resistivity graphite paint and closed with a high-resistivity cover of Luranyl. Either strips or pads are glued onto the high-resistivity plane shared by several modules, or profiles. A detailed view of an LST module is given in Figure 4.16.

Eight of the nine iron gaps hold a single module layer, while one holds a double layer. In addition, there are triple layers just in front of and behind the iron, giving a total of sixteen LST layers. The triple layers, the so-called muon boxes, have two strip layers and one pad layer, while the double layer has one strip and one pad layer. The remaining single layers are all pad layers. This gives totals of five strips and 11 pads.

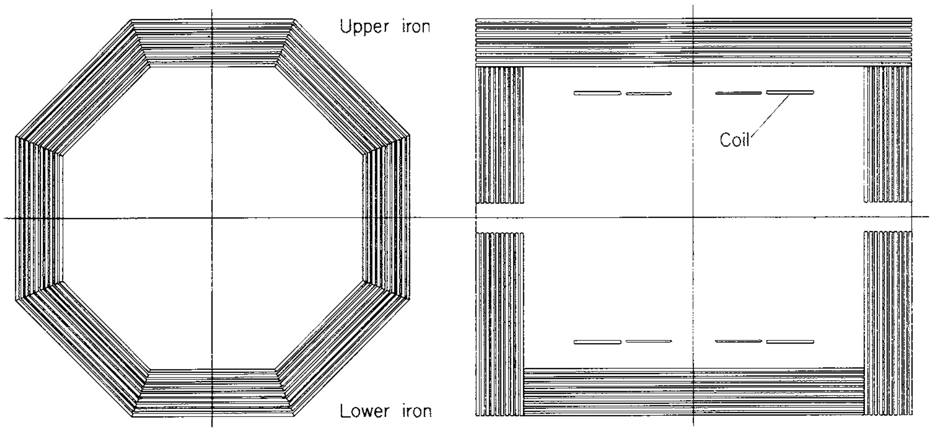

Figure 4.15: Radial (left) and side (right) views of the iron yoke.

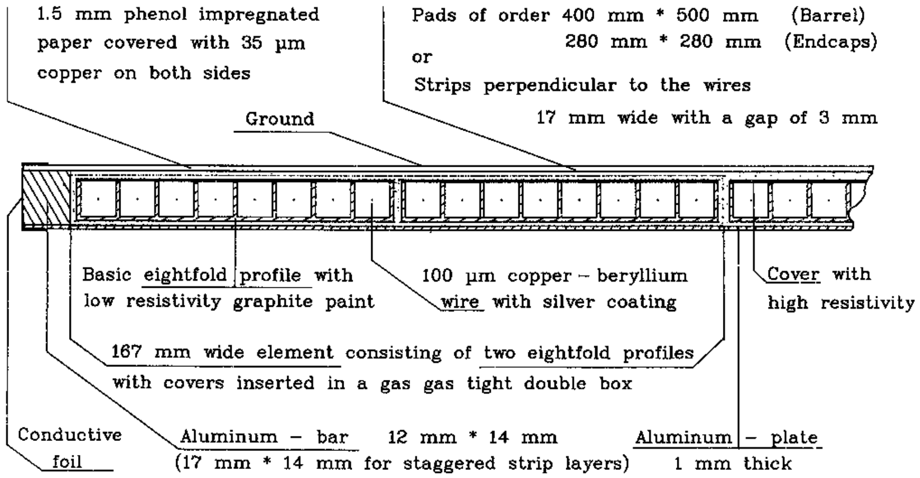

Figure 4.16: Construction of a limited streamer tube module.

The system of strips and wire is read out digitally and provides three-dimensional space points for tracks passing through the instrumented iron. Track reconstruction uses the hierarchy of wires, strips, and pads, with resolutions of 3–4 mm, 10–15 mm, and 10 cm, respectively. A reconstructed track must have at least three wires associated with it, one of them within the iron.

The pad system forms a supplemental calorimeter called the Tail Catcher [38]. The pads, which vary in size depending on their distance from the center of the detector, are summed into front and back towers. Measurements using a test beam at CERN give an energy resolution of about $\frac{\sigma}{E} = \frac{100\%}{\sqrt{E}}$.

4.6 Veto System

For the purposes of background rejection, two separate scintillation veto systems have been installed at H1. The first, the time of flight (ToF) device, is located between the BEMC and the backward iron endcap. It consists of two scintillating planes, each a sandwich of NE102A plastic scintillator and lead mounted on non-magnetic steel. The planes are segmented into individual counters (8 in ToF0, 16 in ToF1), and the inner counters may be remotely pulled away from the beampipe during injection. Signals from the counters pass into high-field Hamamatsu photomultipliers and are amplified. The counters have a time resolution of about 2 ns, and allow gating of the detector using a background window of 25 ns and an interaction window of 13.1 ns immediately (1 ns) thereafter.

The second veto system is called the veto wall. It is actually two separate double scintillator walls, sitting outside the detector at 6.5 m and 8.1 m upstream ($-z$ direction). Figure 4.17 shows the location of the TOF and veto walls with respect to the detector. The 'outer' wall is actually closer to the detector, but starts 0.8 m from the beampipe, surrounding a quadrupole magnet. The 'inner' wall closes to 11 cm of the beam. The outer wall, consisting of 10 individual counters, is approximately the same width as the iron shell of the detector, while the inner wall of 4 counters is only about 1 m wide. The scintillators (NE 114) are shielded with lead and are coupled to shielded VALVO photomultipliers. They identify background particles in coincidence with a time resolution of 8 ns and 3 ns, respectively, allowing a veto on background events.

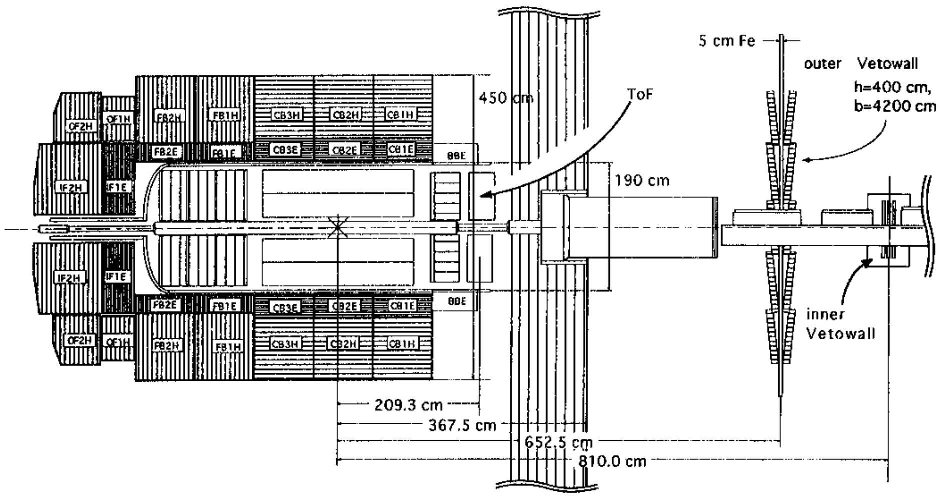

Figure 4.17: Side view showing the location of the TOF and veto walls with respect to the main detector.

4.7 Luminosity System

The luminosity system at H1 consists of an electron tagger (ET) and a photon detector (PD), located far upstream (at about 30 m and 100 m in the -z direction, respectively) of the main detector. Figure 4.18 shows the layout of the luminosity system. Both the electron tagger and the photon detector are Čerenkov calorimeters made of KRS-15 crystals, with a depth of 20 cm, corresponding to about 20 radiation lengths X_0. They are subdivided into arrays of 7x7 (5x5 for the PD) cells, giving position resolutions of 0.3–1.2 mm. The energy resolution of the crystals is $\frac{\sigma}{E} = 1\% \oplus \frac{10\%}{\sqrt{E}}$. The cells are read out by FEU-147 photomultipliers, with a total time resolution of less than 3 ns.

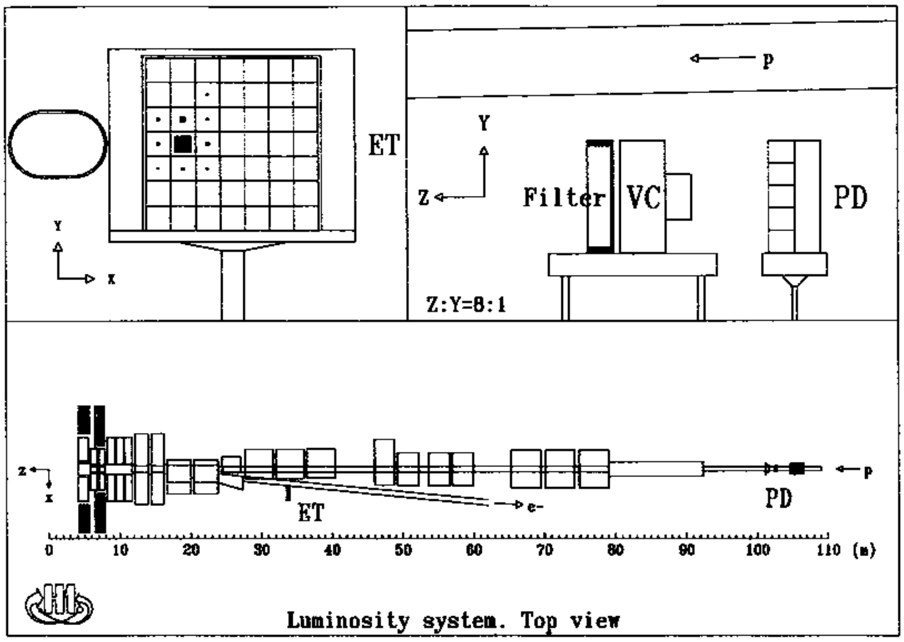

Figure 4.18: Layout of the luminosity system.

The luminosity system measures the luminosity seen by the main detector by detecting Bethe-Heitler events,

$$e + p \to e' + p + \gamma, \tag{4.1}$$

where the scattered electron and the photon are detected in coincidence. The primary background to this process is bremsstrahlung from the residual gas in the beampipe. The rate of this process can be calculated by using electron pilot bunches, where there is no colliding proton bunch. Due to the speed of the luminosity system with respect to the event rates, it is not necessary to eliminate background coincidence events by requiring $E_{ET} + E_{PD} = E_{e-beam}$. Rather, this relation is used to calibrate the two detectors to better than 1% in energy.

The PD is protected from the high synchrotron flux of the HERA machine in the electron direction by a lead filter of 2 X_0, followed by a water Čerenkov counter of 1 X_0, and in the proton direction by a 2 m iron wall. The water counter (VC) is used as a veto to select bremsstrahlung photons, and the energy deposited into it is added to that of the PD for trigger purposes. In addition, the luminosity system can be used to detect photoproduction events where the electron has a small scattering angle, with both the PD and the VC used as vetos.

Chapter 5

Data selection

5.1 Triggers

Events in the H1 detector must trigger at least one of many (128 in 1994) subtriggers in order to be kept for further processing. Subtriggers are built out of logical trigger elements (also numbering 128 in 1994), typically combining elements from separate subdetectors in order to reduce background and triggering rate. Five subtriggers were used in this study. They were chosen for their low prescale (often no prescale), high rate, and coverage of the H1 detector.

5.1.1 DC_RPHI trigger element

The DC_RPHI trigger is a fast track-finder [39] that operates in the $r - \phi$ plane of the central drift chamber. It uses a predefined set of bit masks requiring hits in 4 out of 5 layers in 1 out of 2 two groups for each ϕ segment. Each of these 'trigger roads' is validated in time with a reference wire, which is the wire closest to the crossing point of the track with respect to the wire plane. The DC_RPHI trigger makes available the number of positive and negative track candidates, as well as distinguishing between high- and low-transverse momenta tracks. It becomes efficient for tracks with a transverse momentum greater than 400 MeV/c and with a distance of closest approach (DCA) to the z-axis of less than 4 cm.

5.1.2 z-vertex trigger element

The z-vertex trigger operates in the $r-z$ plane, using pad hits from multiwire proportional chambers to reconstruct the primary vertex of the event [40]. Hits from the CIP, COP, and FPC MWPCs, each of which consists of two independent layers, are used. The trigger constructs rays from groups of 4 MWPC hits, finds their origins on the z-axis, and enters them into a 16 bin wide histogram. This process is repeated for each of 16 ϕ segments, and the resulting histograms are summed into a single z histogram, which is then used for vertex-finding, as well as other triggering elements. Additionally, rays found by the z-vertex trigger are binned into coarse geometrical areas that match the bigtowers in the LAr, and are called bigrays. The z-vertex trigger is efficient for transverse momenta greater than 500 MeV/c.

5.1.3 BEMC subtrigger

Subtrigger 0 is a BEMC trigger that makes use of the Single Electron Trigger element [37]. This trigger performs cluster recognition on the summed analog signals from the BEMC stacks. Subtrigger 0 requires a single cluster using a threshold energy of 7.7 GeV, and is gated with a ToF background veto. The BEMC subtrigger is designed to flag the scattered electron from low Q^2 DIS events, but it will also fire on high-energy decay electrons from the J/ψ. It is fully efficient for electron energies above 10 GeV.

5.1.4 Iron subtriggers

Subtriggers 18 and 19 are muon triggers in the instrumented iron. Subtrigger 18 requires hits in 3 out of 5 planes in any one module in the backward endcap. For the forward endcap, 4 out of 5 planes are required. The barrel part of the iron is covered by subtrigger 19, which has a 3 out of 5 requirement for its modules.

Both of these subtriggers require at least one DC_RPHI-triggered track in the CJC. They also have a ToF veto, an FToF veto, and a requirement of a z-vertex-triggered track or a forward track, with the z-vertex histogram either being low-multiplicity or having a significant peak. Because of the amount of material in front of the barrel part of the iron, only muons with momenta greater than about 1.5 GeV/c will reach this subdetector. For the endcaps, the amount of material is somewhat less.

5.1.5 J/ψ subtriggers

Subtriggers 52 and 54 are specially-designed J/ψ triggers [41] introduced in 1994 with the lowering of the LAr trigger thresholds. Subtrigger 52 requires an LAr bigray, which is formed between a bigtower in the LAr and a geometrically matched bigray in the proportional chambers. The threshold for the bigtower varies with theta, ranging between 1.5 GeV and 10 GeV, in addition to an analog trigger tower threshold which ranges from 0.8 GeV to 2.4 GeV. As a comparison, subtrigger 54 is purely topological, requiring two bigrays that are back-to-back in the $r - \phi$ plane. It does not require any information from the LAr system.

Both subtriggers have the requirement of a small cluster (3 adjacent bins) in the z-vertex histogram and at least one DC_RPHI-triggered track (which must be negatively charged for subtrigger 54). They also have a ToF veto. In addition, subtrigger 52 requires no activity in the inner forward part of the LAr.

5.1.6 Level 4 filter farm

Events that pass the H1 trigger are reconstructed on a fast RAID farm (level 4 filter). Here they must pass a series of logical statements designed to reject background events. Reconstruction modules are called only as needed by the filtering statements, so that events are often rejected early, without requiring full reconstruction. A small fraction, typically 1%, of rejected events are kept for monitoring purposes. The filter farm also provides on-line histograms for monitoring of detector subsystems and calibration data for the main database. Events passing the filter farm are saved on tapes in raw form, and are then reconstructed onto Primary Output Tapes (POTs).

5.2 Class selection

Events are given physics classifications by the offline reconstruction code, during the production of Data Summary Tapes (DSTs) from POT data. Events that do not meet the criteria of any of the physics classes, or that are classified as background, are not used in later analysis. For the 1994 data, several processing runs were required due to bugs in the reconstruction code. During the last processing, selected classes of events were written to separate data streams in order to reduce the volume of data in later analyses. This work makes use of the so-called rho physics class, which is designed to select very-low-multiplicity events for the study of elastic ρ (and other vector meson) production.

5.2.1 Motivation for rho-class code

Ideally, when studying elastic photoproduction, one should be able to select all events with exactly two tracks in the central jet chamber. However, two-track events are not always reconstructed as such. The biggest problem is that of track splitting, which is due to multiple scattering, inefficient regions of the central tracker, and track reconstruction that does not fully compensate for these problems. Thus two-track events may be reconstructed as having three or more tracks. Also possible, though not as common, is a one-track event that is reconstructed as a two-track event. The problem is further complicated by the physics interest of high-Q^2 elastic production, where the electron appears in the BEMC, and possibly has a small track segment in the CJC. The rho physics class code, heavily modified by UCD researchers including the author, attempts to remedy some of these problems. Namely, it attempts to link split tracks, flags events with short track segments in the front of the CJC as possible dissociative events, and allows a track segment in the backward direction for a high-Q^2 scattered electron.

5.2.2 Details of rho-class code

For processing of the 1994 data, the rho physics class code resided in the H1PHAN (H1 physics analysis) program. The code consists of three routines:

`erbmin`, `erho`, and `erotrk`. The subroutine `erbmin` calculates the minimum starting radius for a track in the CJC, based on sick wire maps. It looks for the first 5 consecutive layers with an efficiency of greater than 50%, and sets the minimum radius to that of the first of those layers. Most of the actual work is done in `erotrk`, which will now be described. `Erotrk` makes use of the KTKX bank, which contains both vertex-fitted and non-vertex-constrained tracks in both the central and forward trackers. It also contains central-forward combined tracks, which are vertex-fitted. The subroutine first classifies tracks as good or bad. A forward track is considered good if it has passed the standard software routines and made it into KTKX. Central tracks, however, have the following additional requirements in order to be good: it must have a good starting radius as given by the `erbmin` routine (within 10 cm of the minimum radius), the difference between its start and end radii must be large, it must have a good DCA, it must have an origin close to the z-vertex, and it must have a transverse momentum large enough that it will exit the central tracker. This selection effectively marks as good all tracks except for the small track segments associated with split tracks and tracks that just clip the forward and backward ends of the central jet chamber. The subroutine then requires 2 or 3 good tracks (but not three forward), which must have a total charge between -1 and +1, inclusive. Next, it attempts to link the remaining bad tracks to the good ones. If the parametrization errors of the bad track are too large, then the bad track remains bad. If the bad track seems to originate from the CJC1/CJC2 interface (a result of multiple scattering), the track is ignored. If it is in the far backward direction, and there are only two good tracks, then it is ignored, as it may be the scattered electron clipping the back end of the CJC. Otherwise, the subroutine compares differences in ϕ, transverse momentum, and DCA between the bad track and good ones to their associated parametrization errors. If the differences are all less than the combined errors, then a link is made and the track is removed from the bad track list. When the linking procedure is completed, any remaining tracks with large transverse momentum or small number of hits are ignored as artifacts. Finally, if there are more than two remaining bad tracks, or if there is more than one track in the far-backward direction, the event is not selected. If the good tracks have a common z-vertex consistent with their errors, then the event is selected. The subroutine `erho` takes the information from `erotrk` and makes the final selection cuts. If the event has been flagged as a cosmic by a software cosmic-finder (LCOSF), or if the event has more than two forward tracks, it fails the class selection. Otherwise, the number of bad tracks is checked. Events with no bad tracks pass the selection, while the others are downscaled by a factor of 100. Table 5.1 summarizes the cuts made in the rho classification routine.

Rho class cuts		
Description	Variable(s)	Accepted range
Good starting radius	RBEG $\leq$ RBMAX	$r_{beg} \leq r_{b_{min}} + 10\,\mathrm{cm}$
Large radial span	ABS(REND-RBEG) $\geq$ DRMIN	$\lvert r_{end} - r_{beg}\rvert \geq 10\,\mathrm{cm}$
Small DCA	ABS(DCA) $\leq$ DCACUT	$\lvert dca\rvert \leq 5\,\mathrm{cm}$
Good z-vertex	ABS(Z0) $\leq$ Z0MAX	$\lvert z_0\rvert \leq 50\,\mathrm{cm}$
Large p_t	PT $\geq$ PTMIN	$p_t \geq 0.5\,\mathrm{GeV/c}$

Table 5.1: Summary of track cuts made in rho-classification code.

5.3 J/ψ finder

All rho-class events were then passed through a custom J/ψ finder, which created a text n-tuple for import into PAW. A total of 147 cartridges were processed, each cartridge holding 200 MB, or about 4000 rho-class events. The J/ψ finder was designed to perform fast and simple lepton identification and linking of tracks to lepton candidates in order to select the dileptonic decay mode of the J/ψ. It provides extensive diagnostics and is configurable via control codes passed to it. The code for the finder is distributed across five program files: `runmat`, `match`, `dilepton`, `histos`, and `misc`.

5.3.1 Control codes

The `runmat` file contains the main program. Upon running, the program opens the standard input and attempts to read any control codes. A code consists of an 8-character string followed by a number. Only one code per line is allowed.

These codes, summarized in table 5.2, will now be described.

Control codes			
Code	Values	Default	Description
OUTCODE	1 or 2	1	specifies n-tuple output format
OUTPUT1–3	0–2	0,1,2	specifies event output format
OUTEARLY	0–2	0	filter events for selected triggers
NTRIG	0–5	0	number of selected triggers
ATRIG(x)	0–128	none	selected trigger numbers, x from 1–5
ONLYMC	0 or 1	0	select Monte Carlo Jψ dilepton decays
DSTSEL	0 or 1	0	perform DST selection
PHCLSEL	0–30	0	selected physics class number
TRIGVER	0 or 1	0	verify level 1 triggers with level 4 data
VERTEX	0 or 1	1	use vertex-fitted tracks
NEWTRK	0 or 1	1	use new track bank scheme
NEEDREC	0 or 1	0	perform cluster reconstruction
BEAMTYP	0–3	3	type of beam crossing desired
****STOP****	none	none	stop reading in control codes

Table 5.2: Summary of control codes used in the `runmat` program.

OUTCODE is a flag used to control the format of the output of `dilepton`. The default value is 1, which is a text n-tuple. However, using a value of 2 allows the output of a zebra file, for direct use in other applications such as PAW. Note that this control code was not used, as the author found it easier to concatenate 147 text files and then create one zebra file, rather than having to link that many zebra files together for analysis.

OUTPUT1, **OUTPUT2**, and **OUTPUT3** control the output of events from `dilepton`. Available options are 0, 1, and 2, which mean no output, output the full event, and output the event via an FPACK index file, respectively. The three different control codes are for increasingly strict selections on the events. **OUTPUT1** is for any event that `dilepton` selects as having a J/ψ candidate with a mass within 1 GeV of the standard value. **OUTPUT2** also requires the event to be elastic, having a total of less than 4 central and forward tracks. **OUTPUT3** further requires a value of $W_{\gamma p}$ of greater than 40 GeV. Note that these requirements parallel the cuts imposed in the analysis section of this work.

OUTEARLY is a flag that tells the program to filter the input events and only output those which have a selected trigger bit set. No other processing of the data is performed. This option is useful in reducing a large data set down to only those events that are of interest. Note that this control code uses the same output file as **OUTPUT3** would. The default value of this code is 0; set it to 1 to output full events, and 2 to output an FPACK index file.

NTRIG gives the number of selected triggers. Up to five separate triggers may be selected for analysis. The default is 0 for no selected triggers, which disables **ATRIG**(x).

ATRIG(x) are the codes that designate the selected triggers. The character x is a digit from 1 to 5. Note that this code must be used in conjunction with **NTRIG**. Otherwise, unpredictable results may follow.

ONLYMC is a flag that tells the program to filter input Monte Carlo events and only output those which have a J/ψ decaying into a dilepton pair. No other processing of the data is performed. This option is useful in reducing a generic J/ψ

Monte Carlo file that includes all of the J/ψ decay modes. The default value of this code is 0; set it to 1 to use it. Note that this control code uses the same output file as **OUTPUT1** would, and that full events are output.

DSTSEL is a flag that tells the program to call the DST selection code from the H1REC module. This is only useful for input files which have not been completely processed, *i.e.* Monte Carlo files or raw data tapes. The default value of this code is 0; set it to 1 to use it. Note that, by definition, if an input event does not pass the DST selection code, if will be rejected and will not be processed further.

PHCLSEL gives a physics class number to select. If this number is non-zero, then the input events will be filtered and only those events with the specified physics class will be processed. This control code is useful for eliminating the processing of unwanted events, and for studying class code efficiencies. The default value for this code is 0. The value for the rho-class is 18.

TRIGVER is a flag that tells the program to verify the level 1 trigger bits that it uses with data from the YTL4 bank, which is created on the level 4 filter farm. Use of this code is recommended for data, but it may cause problems with Monte Carlo files. The default value for this code is 0; set it to 1 to use it.

VERTEX is a code developed at time when vertex-fitted tracks were just beginning to be used, during the 1993 data taking. It tells the program to use the vertex-fitted tracks from the KVKR bank during the J/ψ reconstruction in `dilepton`, instead of the KTCF bank, which is normally used in both `match` and `dilepton` for 1993 data. This code is only useful for 1993 data, and is overridden by the **NEWTRK** code. It has a default value of 1; set it to 0 to disable it.

NEWTRK is a code developed for the new track bank scheme first implemented in 1994. It tells the program to use the KTKX bank, which includes both vertex-fitted and non-vertex-constrained tracks in the forward and central trackers, instead of the KTCF bank, in both `match` and `dilepton`. It is recommended to use this code at all times, as the program will default back to the KTCF bank if it can not find the KTKX bank. The default value of this code is 1; set it to 0 to disable it.

NEEDREC is a flag that tells `runmat` to call the cluster reconstruction code from H1REC before calling `match` and `dilepton`. It was developed in order to recover the LAr cluster banks from reduced data sets in 1993, but it may have other uses. The default value of this code is 0; set it to 1 to use it.

BEAMTYP specifies what beam interaction should be selected. Values of 0, 1, 2, and 3 correspond to no beams, proton bunches only, electron bunches only, and proton-electron collisions, respectively. This selection is performed in `dilepton` as opposed to all other event filters, which are performed in `match`, allowing some amount of diagnostics to be run even on non-desirable events. The default value of this code is 3.

****STOP**** is the only code that is not followed by a number. It immediately terminates the reading of codes from standard input, and allows the processing loop to begin. This code is required at the end of the input to `runmat`. Failure to include it will result in error messages and program abort. Note that this is an intentional feature, as it allows control codes for other modules, such as H1REC, to be appended to standard input following ****STOP****.

Note that several of the above codes are used for filtering the input data, and terminate processing for events that fail selections. Therefore there is an inherent override hierarchy present, which runs **ONLYMC**, **TRIGVER**, **DSTSEL**, **PHCLSEL**, and **OUTEARLY**. Thus an event which fails the DST selection will not be tested for physics class, for example. It is also very important to note that **ONLYMC** and **OUTEARLY** skip all processing in `match` and `dilepton`, even for events which pass their selections. Therefore **TRIGVER**, **DSTSEL**, and **PHCLSEL** are of dubious utility when **ONLYMC** or **OUTEARLY** is being used.

After reading the control codes, the main program initializes the diagnostic histograms by calling `histos`, then loops over the events passed to it by FPACK. For each event, it performs reconstruction (if requested by **NEEDREC**) and calls `match` and `dilepton`. Those subroutines access the control codes via a common block, CNTRL.

5.3.2 Lepton identification and linking

The `match` program file contains code for the first part of the J/ψ finder. The code selects lepton candidates, selects 'good' tracks, and makes links based on a chi-squared estimate of the goodness of the link. It then passes the link information to the `dilepton` code for reconstruction of the J/ψ.

When `match` is called, it first performs any filtering tests that are requested via the control codes. If the event passes, the program begins searching for lepton candidates. The first candidates for muons are tracks in the instrumented iron, stored in the ITKR bank. Aside from checking for bad track parametrizations, the only requirement placed on the tracks is that they have at least five hits.

Next, the program looks at clusters in the LAr and BEMC, using the generalized cluster bank RCLU. Both muons and electrons can create clusters in the LAr system. Electrons are stopped rapidly in the electromagnetic section of the calorimeter, whereas muons can leave a trail of hit cells in their wake as they pass through the hadronic section or even come to a stop there. At this point, the only requirements placed on the clusters is that they be completely contained in either the LAr or the BEMC, that they have reasonable parameters, and that they have a theta greater than 0.25. The theta cut is required in order to eliminate the confusion in the very forward direction caused by diffractive events. Note that the cut only applies to the search for lepton candidates; it is not a rapidity cut. Clusters are assigned to be electron candidates if they are in the BEMC or the EM portion of the LAr calorimeter. Clusters in the hadronic part of the LAr are designated as muon candidates.

Having assembled a preliminary list of candidates, the program next tries to eliminate redundant candidates. For example, a muon may leave both a good cluster in the LAr and a good track in the iron. Or, occasionally there may be two or more clusters associated with a particular particle. Therefore the program must look outwards from every good cluster to see if there is another one farther out. This is done in a double loop over the list of lepton candidates, consisting of first the iron tracks, then the clusters, sorted by energy. For each pair of candidates, the following check is made: if they have a distance between them of greater than 25 cm, and if the more distant candidate lies within a $\theta - \phi$ sector centered about the nearer candidate, then the more distant candidate is kept, and the nearer candidate is eliminated from the list. The size of the $\theta - \phi$ sector depends on the combination of candidates, the general idea being that two associated tracks will be very close to one another, but a track associated with a cluster will not be on the vertex-cluster line due to bending in the magnetic field and scattering.

The candidate elimination procedure is demonstrated in Figure 5.1, which shows the pattern of clusters in the LAr that two tracks might generate. Clusters 1 through 3 are made by the first track, which has scattered in the calorimeter. The fourth cluster is due to the second track, which leaves no EM cluster because of the

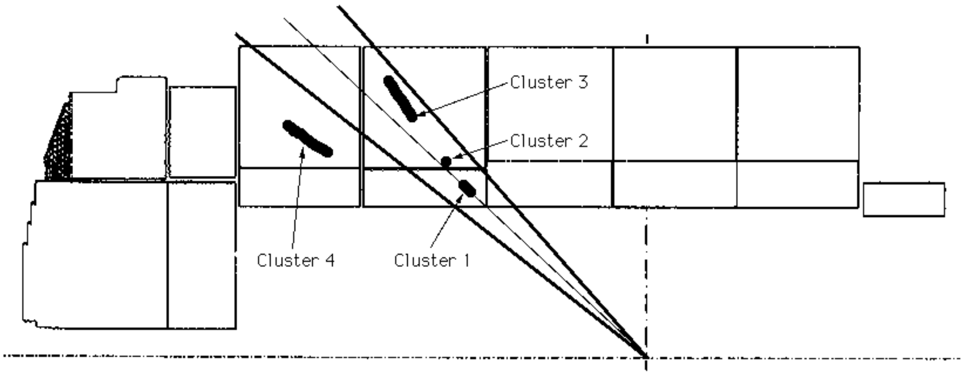

Figure 5.1: A sketch of a possible cluster scenario. In this case clusters 1 and 2 are eliminated in favor of cluster 3, while cluster 4 is also kept.

crack. Assume that the clusters are already ordered by energy. Then the program takes the first cluster and checks if any other clusters are in the same $\theta - \phi$ sector centered about it, depicted by the lines originating at the origin. In this case it finds cluster 2, which is ignored due to its being too close to the first cluster, and cluster 3, which is farther out. Cluster 3 is thus taken as the candidate, while clusters 1 and 2 are dropped from the list. Cluster 4 is sufficiently removed from the others that it is taken as another candidate. Note that the assumed energies of the clusters are not important, as all pairs of clusters are eventually examined. Also note that this is a simplified picture, as there might be iron tracks beyond the clusters. This could possibly cause all of the clusters to be eliminated in favor of the iron tracks.

Once the redundant candidates have been removed, particle-dependent cuts are applied. These cuts are designed to discriminate the leptons from pions. For electron candidates in the BEMC, the hadronic fraction of the energy must be less than 10%. For those in the LAr, a large fraction (greater than 15%) of the energy must be deposited in the first layer and the cluster must have a large length/width ratio. Both LAr and BEMC electrons must have a cluster energy greater than 1.25 GeV. Muon clusters in the LAr must have an energy less than 2.0 GeV because if the muon had had more energy than that, it would have reached the iron. Muon clusters must also have a large length/width ratio since they are minimum-ionizing until energies well below the threshold of the LAr, resulting in long, thin clusters. Table 5.3 summarizes the cuts used to select lepton candidates.

Lepton candidate cuts		
Description	Variable(s)	Accepted range
Distance between candidates	(distance) $\leq$ MINCCDIS	$distance \leq 25\,\text{cm}$
BEMC e^-: Small E_{had}	EBHF $\leq$ HFCUT	$ebhf \leq 0.1$
LAr e^-: Large first-layer energy	EAK0 $\geq$ EAK0CUT	$eak_0 \geq 0.15$
LAr e^-: Large length/width ratio	EAL/EA1 $\geq$ LWCUTE	$eal/ear \geq 1.2$
All e^-: Large cluster energy	CLE $\geq$ CECUT	$cle \geq 1.25\,\text{GeV}$
LAr μ: Large length/width ratio	EAL/EAR $\geq$ LWCUTM	$eal/ear \geq 1.8$
LAr μ: Small cluster energy	CLE $\leq$ CHCUT	$cle \leq 2.00\,\text{GeV}$

Table 5.3: Summary of lepton candidate cuts made in `match`.

Having completed the list of lepton candidates, then program next builds a list of all 'good' tracks. The tracking bank that it uses is determined by the **NEWTRK** control code. Central, forward, and combined central-forward tracks are examined. A good combined track must have a large total momentum, a significant transverse momentum, a good DCA, and a good z_0. A good central track must satisfy the above requirements, plus it must have a good starting radius as given by the `erbmin` routine, just as in the rho-class code. Good forward tracks must have more than one segment and at least 15 total hits in the radial and planar chambers, as well as satisfying the requirements on transverse momentum, total momentum, DCA, and z_0. Finally, a good forward track must have a good χ^2/ndf. Table 5.4 summarizes the cuts used to select 'good' tracks.

Track cuts		
Description	Variable(s)	Accepted range
Large p	P $\geq$ PCUT	$p \geq 0.75\,\mathrm{GeV/c}$
Large p_t	PT $\geq$ PTCUT	$p_t \geq 0.2\,\mathrm{GeV/c}$
Small DCA	ABS(DCA) $\leq$ DCACUT	$\|dca\| \leq 2\,\mathrm{cm}$
Good z-vertex	ABS(Z0) $\leq$ Z0CUT	$\|z_0\| \leq 50\,\mathrm{cm}$
Good starting radius (central)	RBEG $\leq$ RBMAX	$r_{beg} \leq r_{b_{min}} + 10\,\mathrm{cm}$
Good χ^2/ndf (forward)	FCHSQ/FNDF $\leq$ MFRAT	$\chi^2/ndf \leq 5$

Table 5.4: Summary of 'good' track cuts made in `match`.

Once the list of good tracks has been completed, the program attempts to link each lepton candidate to a track. For each lepton candidate, each track is extrapolated outwards until it reaches the target surface of the candidate. For tracks in the iron endcaps, clusters in the forward section of the LAr, and clusters in the BEMC, this surface is a plane given by the z-coordinate of the candidate. For tracks in the iron barrel or the LAr barrel, the surface is an axial cylinder with radius given by the radial distance of the candidate. Figure 5.2 gives a sketch of this track extrapolation.

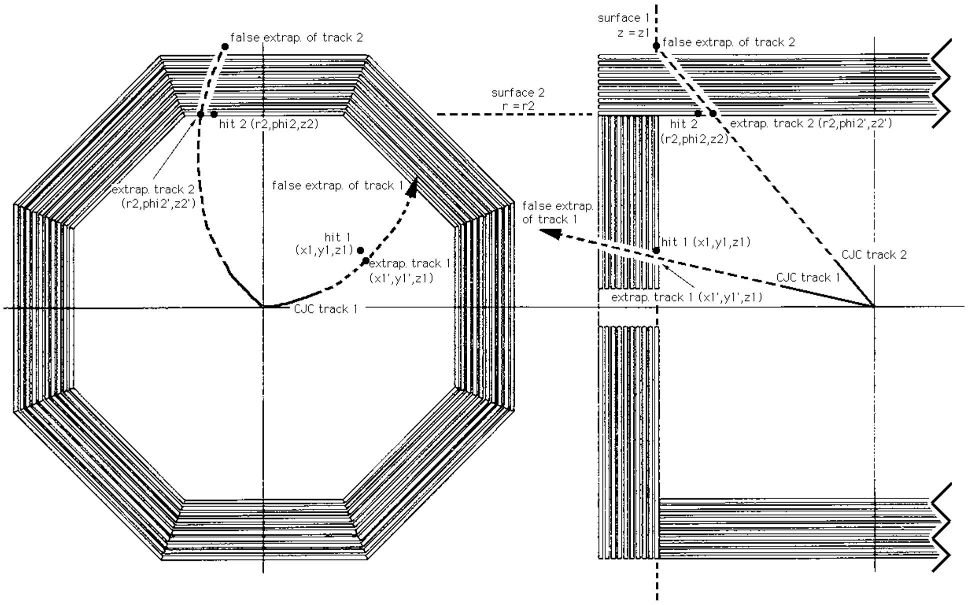

Figure 5.2: A demonstration of how tracks are extrapolated to the target surface of candidates. Note how the wrong combinations of track and candidate typically give very bad matches.

At the point of intersection both the distance and error are calculated. The error includes the positional error of the lepton candidate, the parametrization error of the track propagated to the target surface, and a theta-dependent scattering term. From the distance and error a χ^2 value is formed for the linking of the track to the lepton candidate. Additional penalties are imposed on unlikely links, such as a target surface outside the boundaries of the detector or a track pointing away from the lepton candidate, by adding to the value of χ. No cuts are made on the value of χ. However, there is a maximum distance cut imposed. It is 15 cm for electron clusters, 25 cm for hadronic clusters, 50 cm for iron endcap tracks, and 100 cm for iron barrel tracks. As a final restriction to the linking, the cluster-track pair must have an E/p ratio of between 0.5 and 2.0 for electrons and 0.0 and 2.0 for muons. These final cuts are summarized in table 5.5.

Lepton candidate-track link cuts		
Description	Variable(s)	Accepted range
track-e^- cluster distance	DIST $\leq$ MAXDIS1	$dist \leq 15\,\mathrm{cm}$
track-μ cluster distance	DIST $\leq$ MAXDIS2	$dist \leq 25\,\mathrm{cm}$
track-endcap μ distance	DIST $\leq$ MAXDIS3	$dist \leq 50\,\mathrm{cm}$
track-barrel μ distance	DIST $\leq$ MAXDIS4	$dist \leq 100\,\mathrm{cm}$
E/p ratio for e^-	EEPCUTL $\leq$ CLE/P $\leq$ EEPCUTH	$0.5 \leq E/p \leq 2$
E/p ratio for μ	MEPCUTL $\leq$ CLE/P $\leq$ MEPCUTH	$0.0 \leq E/p \leq 2$

Table 5.5: Summary of cuts on possible lepton candidate-track links in `match`.

After all candidate-track links are considered, the program has a matrix of χ^2 values. It then creates a link for the pair with the best χ^2 and eliminates the candidate and cluster from further linking. Then it chooses the next best χ^2 and so on.

This completes the linking procedure in `match`. The routine provides a large common block of data, MTCH, for subsequent use in `dilepton`. The block contains information on the numbers and types of candidates and good tracks found, the results of the linking procedure, and some miscellaneous triggering information.

5.3.3 J/ψ reconstruction

The `dilepton` routine takes over from `match` in the event processing. It first extracts general information for the event. This includes downscaling factor, event T_0, and bunch type, current, and luminosity. If the bunch type is not that selected by the control codes (see **BEAMTYP**), the program exits. It also looks for tagged particles such as an electron in the Etagger, a photon in the photon tagger, and an electron in the BEMC. Minimum energies of 10 GeV, 5 GeV, and 5 GeV, respectively, are required for these to be flagged. If a tagged electron is found, then the program reconstructs the electron side of the kinematics. In any case, a Jacquet-Blondel computation of y is performed using calorimeter information, and a quasi-JB computation of Q^2 is made using the good tracks. The program also checks the plug calorimeter for clusters.

Next, it takes the data from the MTCH common block and attempts to reconstruct a J/ψ and its associated kinematics. This is a fairly straightforward procedure of taking all pairs of tracks and forming an invariant mass. The program uses pairs in which each track has a lepton associated with it and pairs in which only one of the track has a lepton linked to it, with the other track satisfying the 'good' track cuts. The only cut that is imposed is that the tracks must have their z_0 parameters within 25.0 cm of each other. There is a cosmic finder that flags collinear pairs of tracks: if the tracks have a difference in both θ and ϕ of less than 0.2 radians they are flagged. Reconstruction of the J/ψ candidate allows completion of the event kinematics such as momentum transfer t. For a BEMC-tagged electron, the program checks that the cluster is not linked to one of the good tracks.

N-tuples for both unlike-sign and like-sign pairs are output. The n-tuples contain the track and cluster parametrizations, reconstructed kinematics, and event information. All variables in the n-tuple are present in a common block called OUTCOM. In addition to the n-tuples, `dilepton` also can output three separate data streams of increasing selectivity. See the control codes section for more information on these outputs.

5.3.4 Diagnostics and miscellany

Throughout the processing, both `match` and `dilepton` generate numerous diagnostic histograms in LOOK. These are printed in the program log file, at the end of processing. The histograms allow one to observe the distributions of important quantities (essentially all variables that have cuts placed on them) and the efficiencies of the cuts. Many of these histograms have been disabled in the working version of the program because of the large amount of output they create. However, it is possible to activate them by uncommenting the relevant lines in both `histos` and either `match` or `dilepton` and recompiling. Unfortunately, there is no easy way to select histograms without recompiling.

The final file in the set, `misc`, contains a variety of often-used routines for unpacking or extracting data from the event banks. These routines should be altered only in the event of a change in the data bank structures. They have no physics content.

Chapter 6

Simulation

Monte Carlo studies are vital to the understanding of acceptances, efficiencies, and reconstruction techniques. Of these, it is foremost in importance to determine that the kinematic variables of an event can be reconstructed with sufficient accuracy. Efficiency issues will be returned to later in the analysis. There are several Monte Carlo generators available and applicable to the study of J/ψ photoproduction, corresponding to the different models described in the chapter on theory. For analysis, each of the generated files was fully reconstructed and passed through the complete event selection process described in the previous chapter.

6.1 DIFFVM 1.0

The Monte Carlo program DIFFVM generates events based on the VMD model of photoproduction. It can be configured to generate purely elastic events or diffractive events in which the proton dissociates. A total of 10,000 elastic events were produced for both of the J/ψ leptonic decay channels. The same number of diffractive events was also generated. For elastic production, the events were produced at a fixed $\hat{s} = m^2_{J/\psi}$, having an energy dependence (Eq. 3.3) $W^{4\epsilon}_{\gamma p}$ with $\epsilon = 0.225$ and a exponential t distribution (Eq. 3.4) with $b = 4\,\mathrm{GeV}^{-2}$. The exponent to the VMD propagator (Eq. 3.2) was set to 2.5. For the diffractive events, the value of b was $2\,\mathrm{GeV}^2$. Proton dissociation was done by JETSET 7.4[43], which uses the Lung string model of fragmentation.

6.2 EPJPSI 3.3

EPJPSI is a Monte Carlo generator [42] based on the photon-gluon fusion process (Eq. 3.9). It can produce events using one of several models, including the color singlet model [31] and the open charm model of Jung [33]. A total of 10,000 elastic (open charm) events were produced for both of the J/ψ leptonic decay channels. A set of 10,000 inelastic (color singlet) events were also generated, with the J/ψ decaying to muons. The corresponding electron channel events were generated but never reconstructed. For the elastic events the gluon distribution of the MRS D- set was used, while the inelastic events used that of the MRS D0 set[45].

6.3 LPAIR 2.0

The background of QED-produced lepton pairs is simulated using the Monte Carlo program LPAIR [44]. Four different processes were studied: the elastic process,

$$e + p \to e + p + l^{+} + l^{-}, \tag{6.1}$$

and the inelastic process,

$$e + p \to e + X + l^{+} + l^{-}, \tag{6.2}$$

which was broken into three kinematic regions: $Q^2 > 5\,\mathrm{GeV}^2$, $Q^2 < 5\,\mathrm{GeV}^2$ with $m_X > 2\,\mathrm{GeV}$, and $Q^2 < 5\,\mathrm{GeV}^2$ with $m_X < 2\,\mathrm{GeV}$. Acceptance cuts were applied at the generator level. The calculated cross sections for each of the processes were approximately 1900 pb, 40 pb, 340 pb, and 170 pb, respectively, and the total number of generated events corresponded to $10\,\mathrm{pb}^{-1}$ of luminosity.

6.4 Kinematic reconstruction

6.4.1 Mass reconstruction

Figures 6.1a and 6.1b show the reconstructed mass for the DIFFVM generated events, elastic and proton dissociative, respectively. In both cases, the peak has a gaussian shape due to the momentum resolution of the central tracker. The slight tail to lower masses is due to decay electrons losing energy in the volume of the detector. Almost all accepted events are reconstructed correctly, even in the dissociative sample.

a) 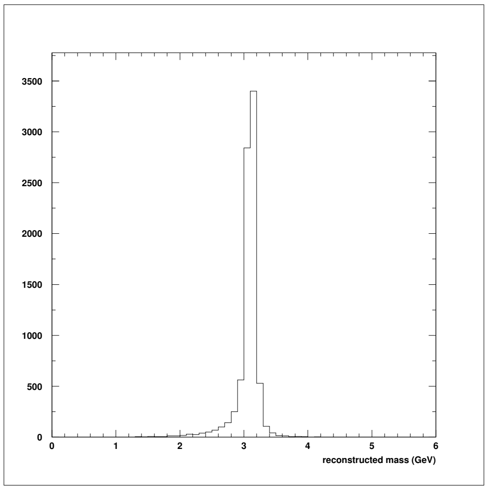

b) 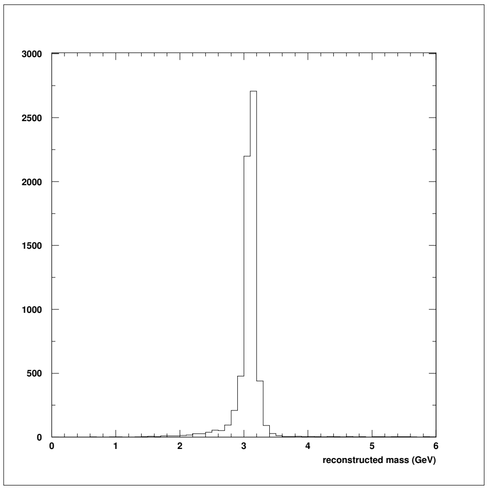

Figure 6.1: Reconstructed mass for a) elastic events, and b) proton dissociative events from the DIFFVM Monte Carlo.

6.4.2 $W_{\gamma p}$ reconstruction

After mass, the most important kinematic variable to this study is the photon-proton center-of-mass energy, $W_{\gamma p}$. Figures 6.2a and 6.2b show the reconstructed vs. generated $W_{\gamma p}$ for the DIFFVM events, elastic and proton dissociative, respectively. The reconstruction was performed using Eq. 2.10 with Q^2 set to 0. Only in the dissociative case are there any events with a poorly reconstructed $W_{\gamma p}$, and those represent just a small fraction of the sample.

a) 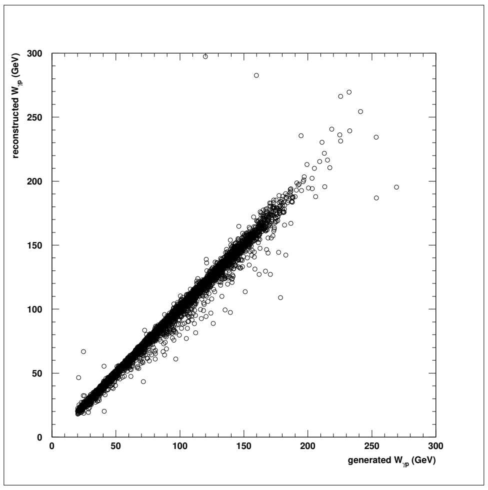

b) 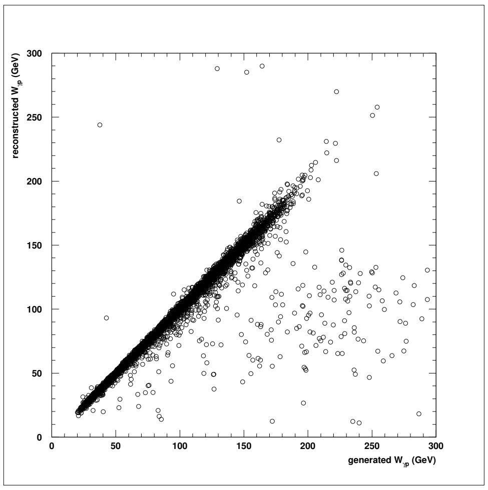

Figure 6.2: Reconstructed vs. generated $W_{\gamma p}$ for a) elastic events, and b) proton dissociative events from the DIFFVM Monte Carlo.

6.4.3 Low-Q^2 y and t reconstruction

As Eq. 2.14 shows, once $W_{\gamma p}$ is known for a low-Q^2 event, then we have a good approximation for y. This is demonstrated in Figures 6.3a and 6.3b.

Even more accurate is the reconstruction of E_γ (see Eq. 2.18) under this model, as shown in Figures 6.4a and 6.4b.

However, this does not lead to a corresponding accuracy in the reconstruction of t. The reason for this is that the transverse components of the photon's momentum are still unknown and unaccounted for. Figures 6.5a and 6.5b show the results of using the approximation of p_t^2 of the J/ψ for t. Fortunately, we are not

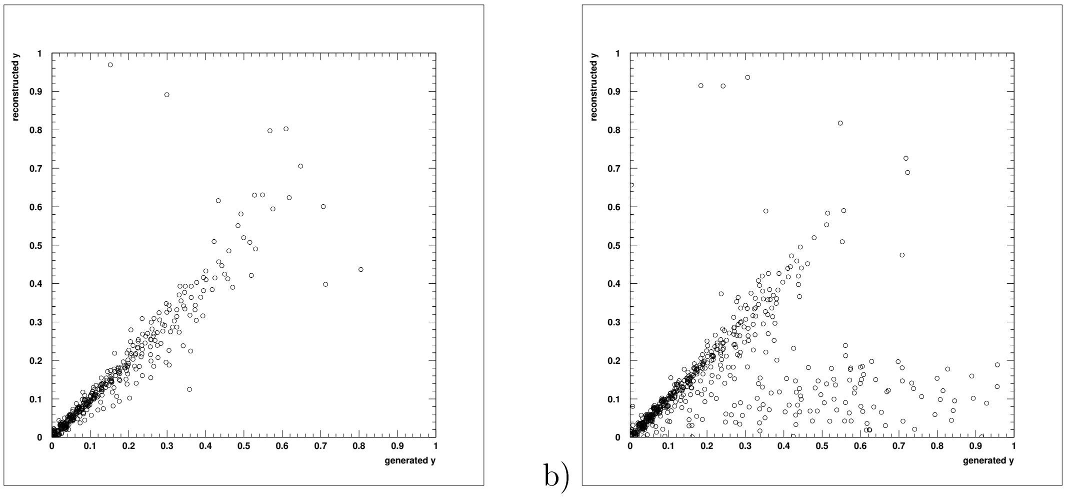

a) b)

Figure 6.3: Reconstructed vs. generated y for a) elastic events, and b) proton dissociative events from the DIFFVM Monte Carlo.

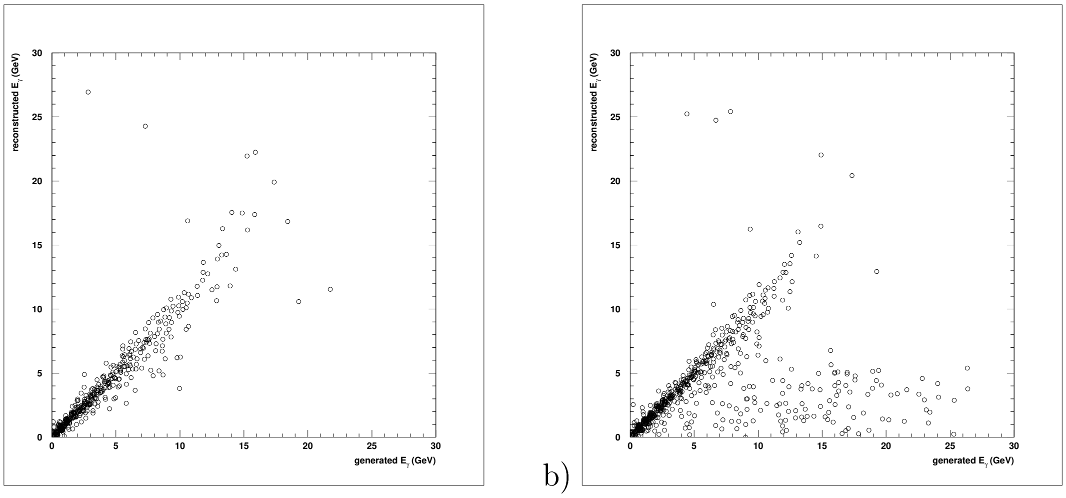

a) b)

Figure 6.4: Reconstructed vs. generated E_γ for a) elastic events, and b) proton dissociative events from the DIFFVM Monte Carlo.

concerned so much with the value of t on an event-by-event basis as we are on the shape of the distribution, which can then be corrected for according to the Monte Carlo.

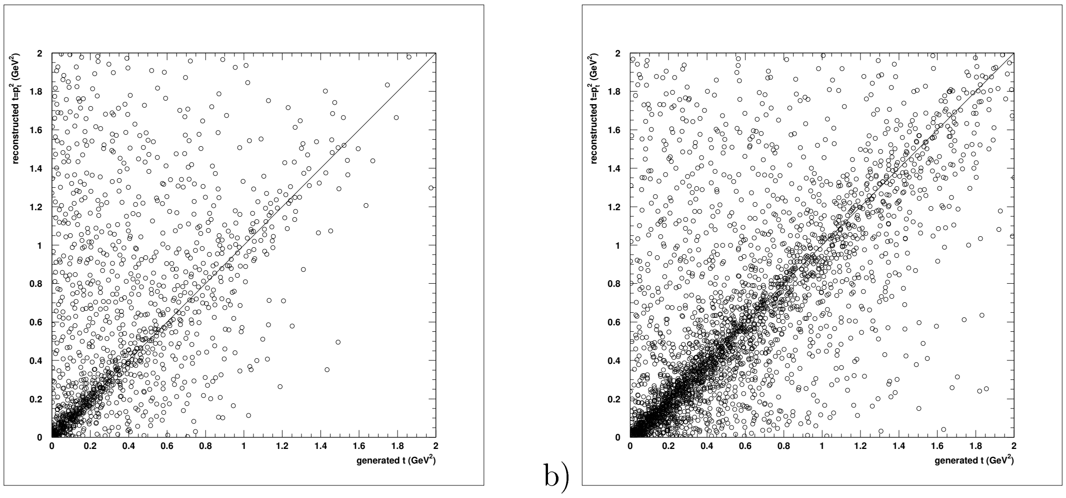

a) b)

Figure 6.5: Reconstructed vs. generated t for a) elastic events, and b) proton dissociative events from the DIFFVM Monte Carlo.

6.4.4 High-Q^2 Q^2 and y reconstruction

For events in which the beam electron is scattered into the BEMC, there is additional information available for kinematic reconstruction. For example, Figures 6.6a and 6.6b show the reconstructed versus generated Q^2 for events where the beam electron is flagged by the `dilepton` routine. Almost all of the events are reconstructed correctly, given the energy and spatial resolution of the BEMC.

However, in Figures 6.7a and 6.7b we see that the reconstruction of y is worse for these high-Q^2 events than if we had used the $W_{\gamma p}$ approximation.

6.4.5 Bjorken x versus parton x

Finally, it is worthwhile noting the surprisingly dramatic difference between Bjorken x and parton x. Comparison of the two (Eqs. 2.19 and 2.25) shows that

a) 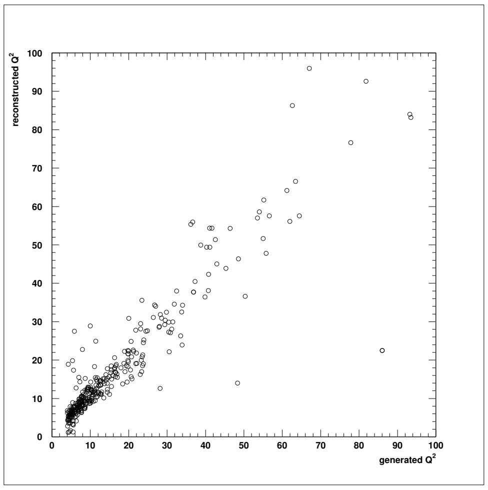 b) 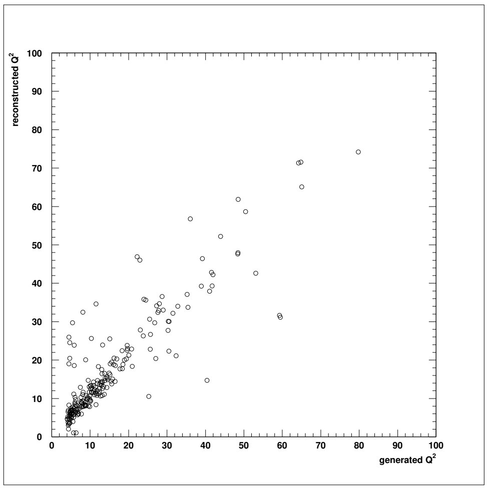

Figure 6.6: Reconstructed vs. generated Q^2 for high-Q^2 a) elastic events, and b) proton dissociative events from the DIFFVM Monte Carlo.

a) 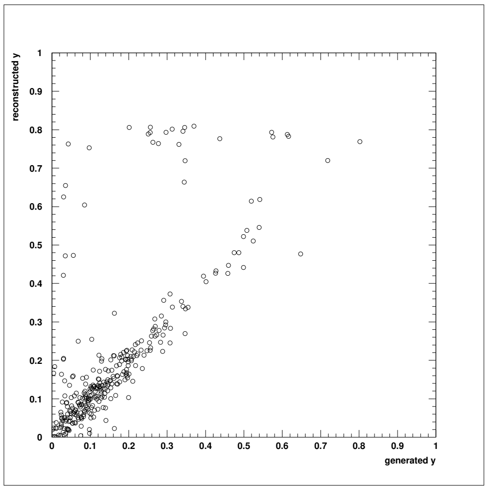 b) 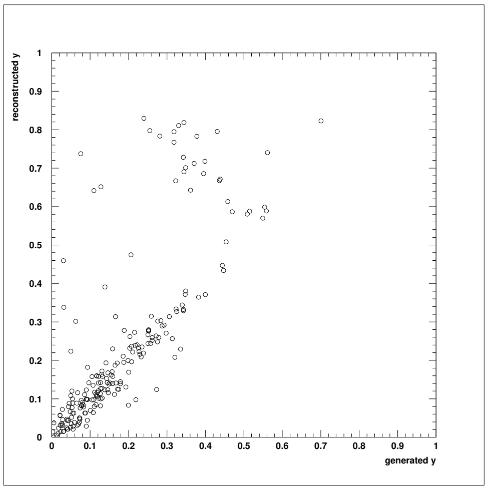

Figure 6.7: Reconstructed vs. generated y for high-Q^2 a) elastic events, and b) proton dissociative events from the DIFFVM Monte Carlo.

they differ only by the $\hat{s}$ in the numerator of $x_{I\!P}$. Therefore, they should be nearly equivalent for values of Q^2 larger than $\hat{s}$, which is set to $m^2_{J/\psi}$ in this model. However, this condition is not often satisfied in elastic photoproduction. Figure 6.8 shows how

x_B and $x_{I\!P}$ compare under the DIFFVM model. This is one case in which the specific definition of x becomes important.

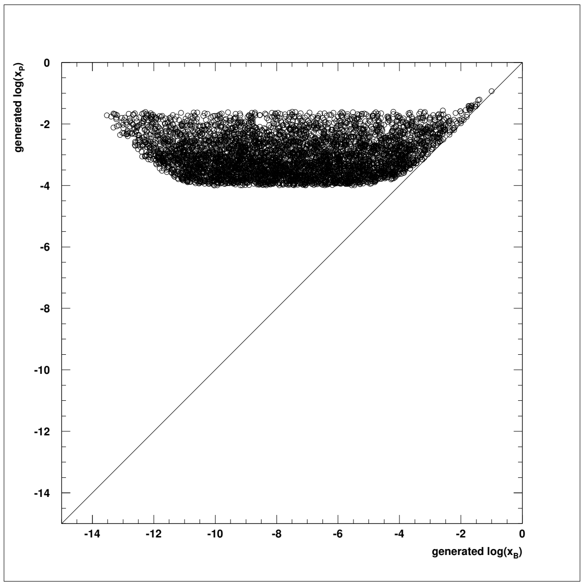

Figure 6.8: Reconstructed $x_{I\!P}$ vs. generated x_B for elastic events from the DIFFVM Monte Carlo.

6.5 Simulation of triggers

At this point it is worthwhile considering how well the Monte Carlo simulation reproduces the behavior of the subtriggers used in this study. This is primarily a matter of the mechanics of the simulation - the specific kinematics should not affect the results, so long as Monte Carlo kinematics reproduce those of the data. However, since a large fraction of the data contains events with a topology dissimilar to that of a generated J/ψ event, care must be taken to isolate the triggering track from the rest of the event.

For example, Figure 6.9 showns the efficiency of subtrigger 18 for the backward iron endcap. The event selection used for both the Monte Carlo and the data plots is the following: the first track must be identified as a muon in the iron and have a θ in the backward direction, while the second track must be linked to no lepton candidate and have a θ in the central barrel region. Selecting a single-track efficiency in this manner should allow direct comparison between the elastic VMD Monte Carlo file and the data.

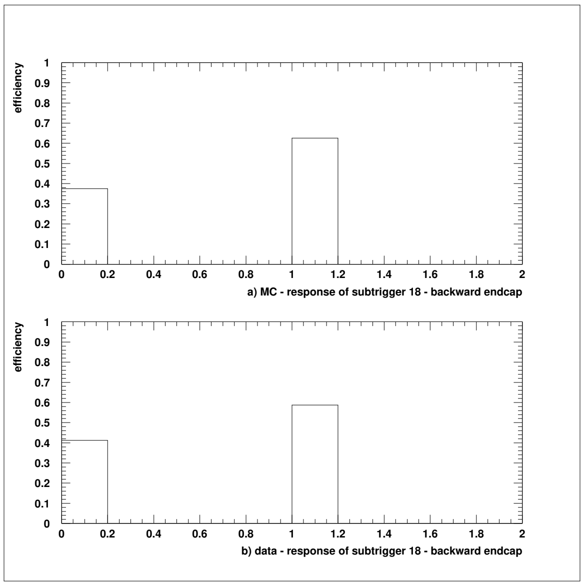

Figure 6.9: Response of subtrigger 18 (iron endcap) for a) Monte Carlo and b) data in the backward direction.

It can be seen in Figure 6.9 that the behavior of the iron endcap trigger is well described in the Monte Carlo for tracks in the backward direction. However, in the forward direction there is some discrepancy, as can be seen in Figure 6.10. The reason for this is unclear, but the question is somewhat moot, as nearly all forward endcap events are removed by the $W_{\gamma p}$ cut in the analysis.

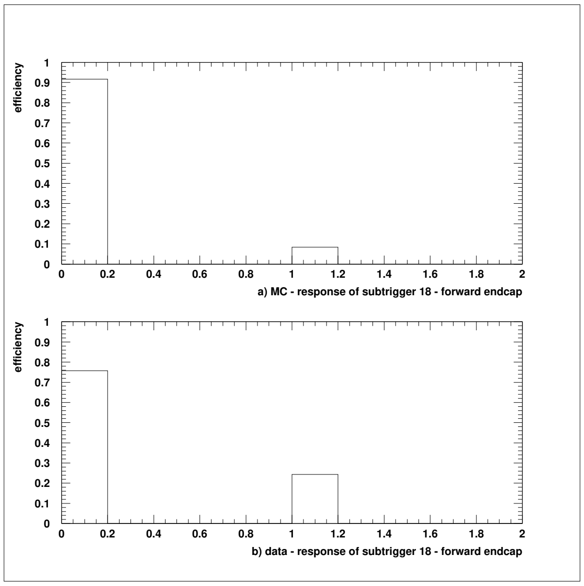

Figure 6.10: Response of subtrigger 18 (iron endcap) for a) Monte Carlo and b) data in the forward direction.

Similarly, subtrigger 19 (central iron barrel) can be checked by requiring the first track to be identified as a muon and having a θ in the central region, while the second track is unlinked and has a θ outside of the central region. As Figure 6.11 shows, the Monte Carlo and the data are in agreement for this subtrigger.

The event selection for the check on subtrigger 52 (LAr bigray) is for the first track to have a θ in the central region of the detector, and for the second track to

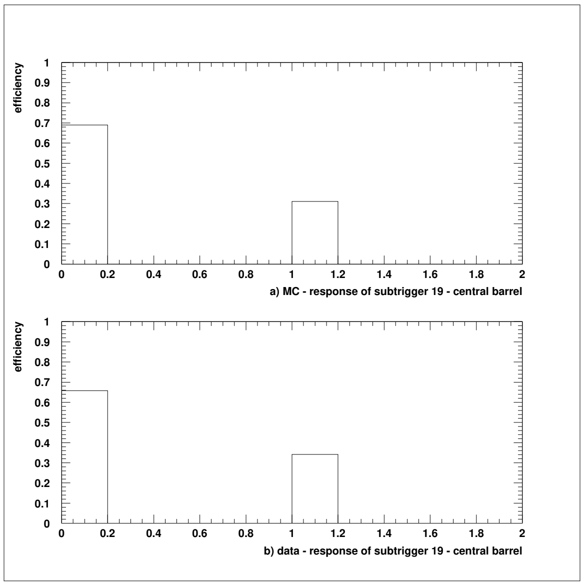

Figure 6.11: Response of subtrigger 19 (iron barrel) for a) Monte Carlo and b) data.

have a θ outside of the central region. No identification requirements are imposed. Figure 6.12 shows the resulting efficiencies. Again, the Monte Carlo and the data agree.

Finally, Figure 6.13 shows the efficiency comparison for subtrigger 54 (topological bigray). Here the selection requires both the first and the second track to point in the central region, since that is the triggering topology. No identification requirements are imposed. In this figure we can see that there is a significant (20%) discrepancy between the Monte Carlo and the data. Once again, the reason for this difference is unclear.

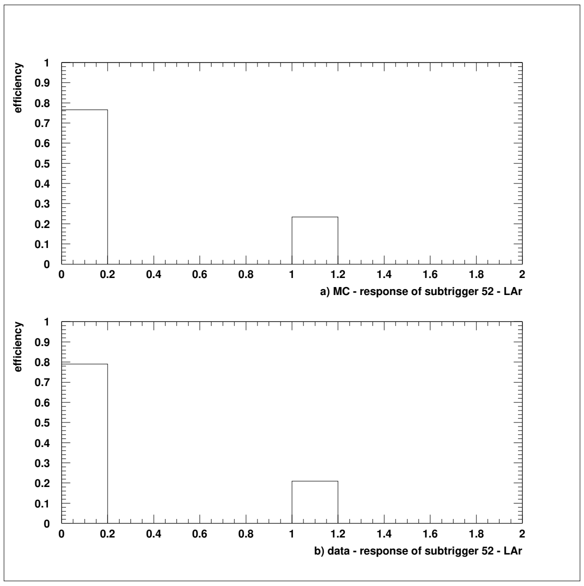

Figure 6.12: Response of subtrigger 52 (LAr bigray) for a) Monte Carlo and b) data.

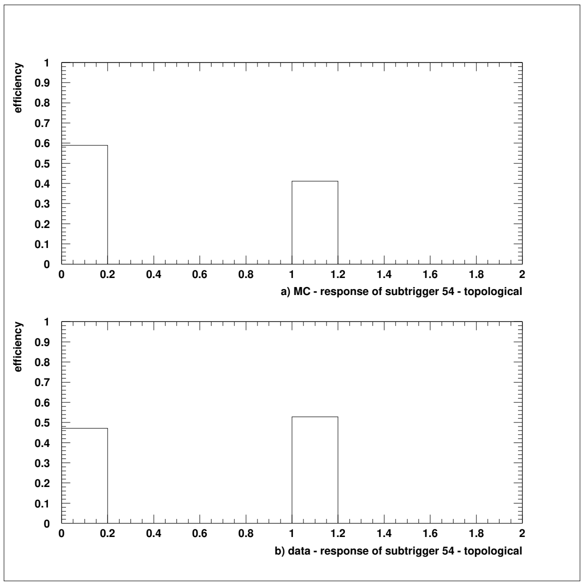

Figure 6.13: Response of subtrigger 54 (topological bigray) for a) Monte Carlo and b) data.

Chapter 7

Analysis

A total integrated luminosity of $6\,\mathrm{pb}^{-1}$ was provided by HERA, with almost $4\,\mathrm{pb}^{-1}$ available for H1 physics. The data run was broken into four periods: electron-proton collisions, positron-proton collisions, positron-proton collisions after repairs of the CJC, and shifted vertex positron-proton collisions. During the shifted vertex runs, the interaction point was shifted by 70 cm along the z-axis in order to provide a different accepted range of y and Q^2. Table 7.1 shows a summary of delivered integrated luminosities for the run periods. These values are not corrected for satellite bunches, absolute normalization, or detector status.

Because some subdetectors were not supplied with high voltage for the entire running period, each physics trigger was exposed to a slightly different luminosity. Table 7.2 summarizes the luminosities taken by each of the triggers considered in this work. These values were determined with the use of the `runlumi` routine, which takes luminosity information from the H1 database (using the `gethl1` routine from H1UTIL) and corrects it on a run-by-run basis using detector high voltage status information, also in the H1 database. Note that the shifted vertex runs are not included in the analyzed data sample. The 'baseline' entry refers to the raw luminosity as stored in the H1 database. The difference between the total baseline luminosity and the total H1 physics luminosity is due to some runs being classified as 'poor', *i.e.* beam conditions or detector status were so poor as to make the runs useless for physics.

Luminosity (nb^{-1})				
Run Period	e^-p Collisions	e^+p Collisions	Shifted e^+p Collisions	Total Lumi Delivered
HERA total	938.21	4977.43	85.79	6001.43
HERA physics	846.21	4664.58	78.33	5589.12
H1 runs	714.23	4111.74	71.67	4897.64
H1 gated	532.03	3509.62	67.38	4109.03
H1 physics	492.51	3424.00	64.98	3981.49

Table 7.1: Summary of luminosity for 1994 data run.

Luminosity (nb^{-1})					
Run Period	e^-p Collisions	e^+p Collisions	e^+p Collisions	e^+p Collisions	Total Lumi Delivered
Run Range	78381 - 82005	82961 - 87556	87586 - 89912	90101 - 90419	
Baseline	348.4	1207	1023	145.9	2724
Subtrigger 0	248.6	1114	972.4	140.9	2476
Subtrigger 18	215.7	884.6	869.6	119.5	2089
Subtrigger 19	215.7	884.6	869.6	119.5	2089
Subtrigger 52	219.7	895.9	891.0	120.1	2127
Subtrigger 54	219.7	895.9	891.0	120.1	2127

Table 7.2: Summary of subtrigger luminosities for 1994 data run.

7.1 Event Selection Criteria

Figure 7.1 shows the resulting dilepton mass distribution from the 1994 data run. The J/ψ mass peak is quite evident. At this point some analysis cuts are made on the data sample in order to reduce the background.

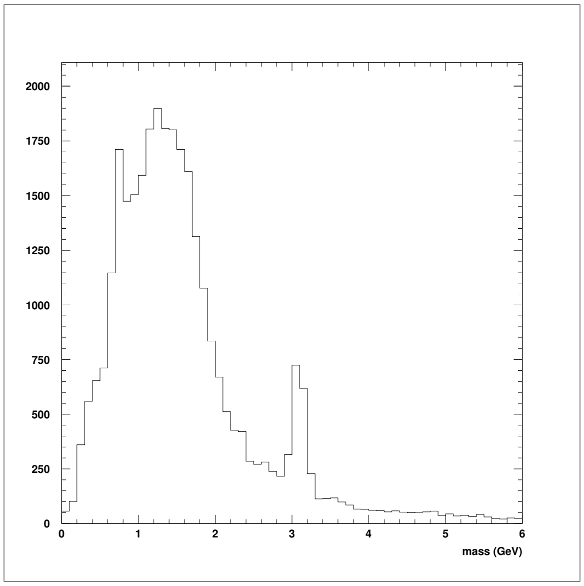

Figure 7.1: Dilepton mass distribution for 1994 data, before analysis cuts.

7.1.1 Cosmic ray cut

One of the most obvious sources of background is cosmic rays. Passing through the detector during the beam crossing gate, they produce what appear to be high momentum back-to-back tracks, much like one would expect from a J/ψ decaying at rest. There are two basic methods for removing cosmic rays: cutting on time of arrival (event T_0) and cutting on track collinearity. The problem with a timing cut is that the distribution of real event T_0 is somewhat broad (see Figure 7.2), and even a strict cut would still leave some contamination from cosmics. A collinearity cut guarantees the removal of all back-to-back tracks (short of badly

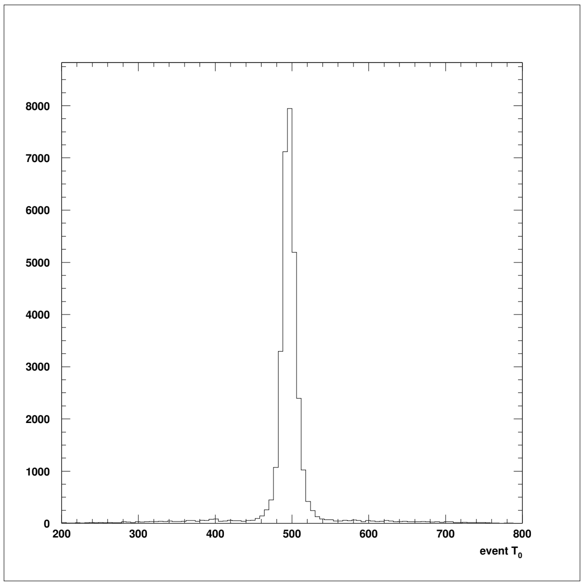

Figure 7.2: Event T_0 for 1994 data, before analysis cuts.

reconstructed ones), but has the drawback that it also cuts some real J/ψ events. A collinearity cut is the better choice, as the complete removal of all cosmic rays is worth the small (about 1%) loss in signal. Given two tracks with momentum vectors $\vec{p_1}$ and $\vec{p_2}$, we define the angle between them as

$$\cos(\Theta) = \frac{\vec{p_1} \cdot \vec{p_2}}{|\vec{p_1}||\vec{p_2}|}. \tag{7.1}$$

This quantity is shown in Figure 7.3 for the raw data sample. The sharp peak at

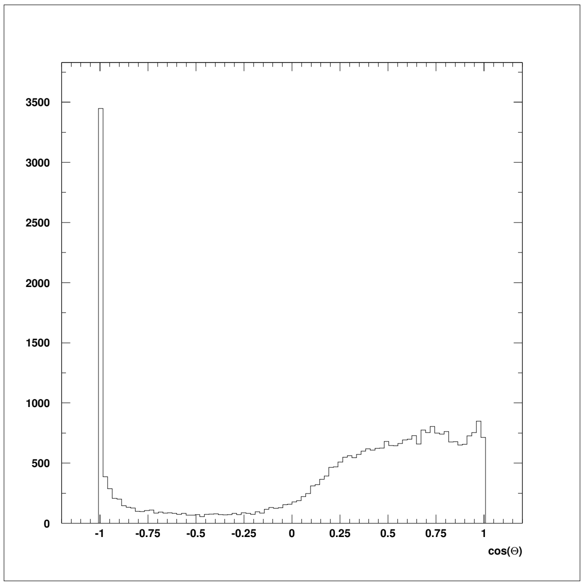

Figure 7.3: The quantity $\cos(\Theta)$ for 1994 data, before analysis cuts.

$\cos(\Theta) = -1$ is due to cosmics. By examination of the correlation of this quantity with timing (see Figure 7.4) and its distribution in events without colliding beams (see Figure 7.5), where cosmic rays are common, it was determined that the optimal cut for the removal of cosmic ray events is $\cos(\Theta) > -0.98$.

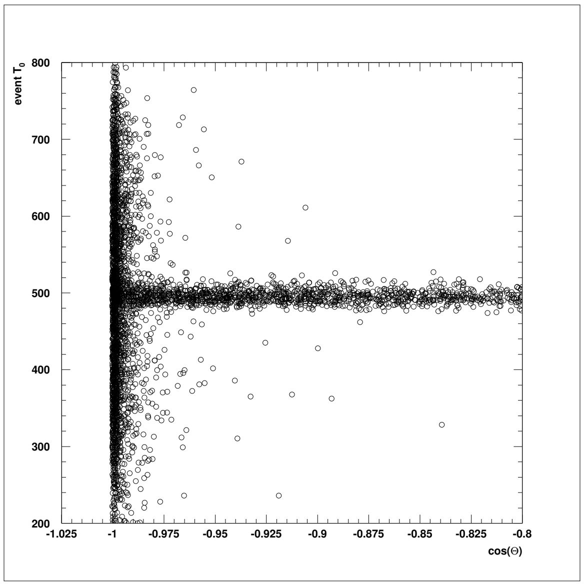

Figure 7.4: Event T_0 vs the quantity $\cos(\Theta)$ for 1994 data, before analysis cuts.

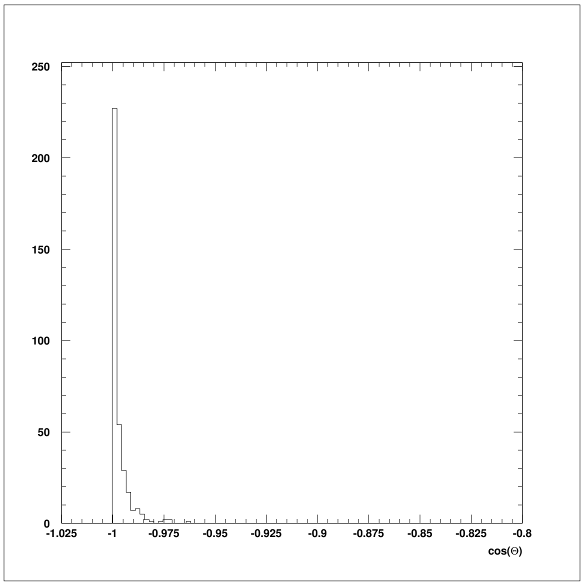

Figure 7.5: The quantity $\cos(\Theta)$ for non-colliding proton bunches (dominated by cosmic rays) in the 1994 data.

7.1.2 Track multiplicity cut

The next cut that is applied is that the total number of tracks in the event must be either 2 or 3. This is a somewhat stricter requirement than is placed on events in the class selection routine. The cut is useful for removing the combinatorial background introduced by having many tracks, and makes a significant reduction in the number of low-mass entries in the data. Figure 7.6 shows the track multiplicity of the data sample before this cut is applied. Note that this is the total number of tracks in the detector, not the number of good tracks as determined by either the class selection or the matching routines.

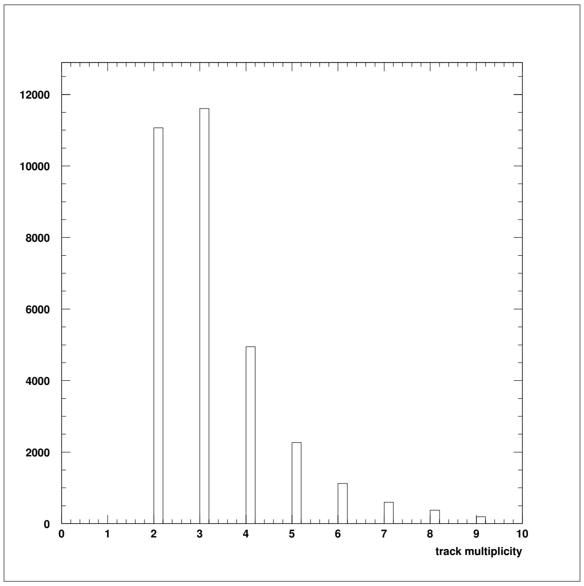

Figure 7.6: Track multiplicity for 1994 data, before analysis cuts.

7.1.3 $W_{\gamma p}$ cut

The most important cut is the cut on $W_{\gamma p}$. Examination of the data shows that a majority of the low-mass background has $W_{\gamma p}$ values below 40 GeV. Figure 7.7a shows the distribution of this quantity for the raw data sample, and Figure 7.7b shows its distribution as a function of mass. Furthermore, one can obtain

a) 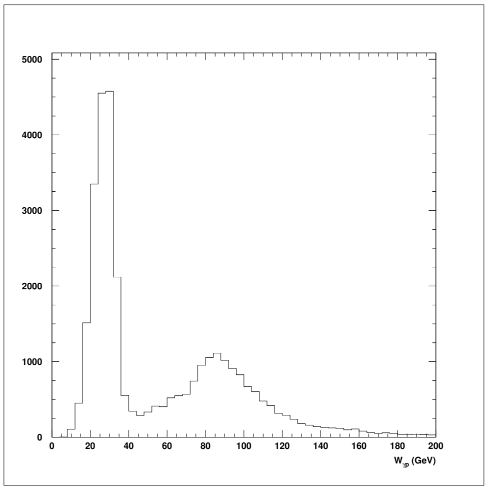

b) 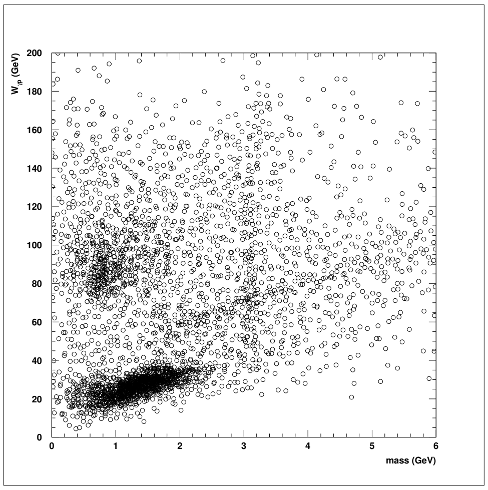

Figure 7.7: a) $W_{\gamma p}$ distribution for 1994 data, before analysis cuts, and b) as a function of mass.

an estimate for the minimum $W_{\gamma p}$ possible in J/ψ production by taking Eq. 2.10 in the high-p_z limit. Doing so, one arrives at the equation:

$$W_{\gamma p}{}_{min}^{2} \simeq 2E_p p_{t_{J/\psi}}. \tag{7.2}$$

Substituting 0.2 GeV/c as the minimum p_t for the J/ψ to be seen in the detector, this evaluates to $W_{\gamma p} \simeq 18$ GeV. The DIFFVM Monte Carlo (see Figure 7.8) shows that the $W_{\gamma p}$ distribution for accepted J/ψ events starts at about 15 GeV and rises sharply to about 35 GeV. The $W_{\gamma p}$ cut, placed at 40 GeV, avoids this region where the acceptance is changing rapidly, as well as removing much of the background.

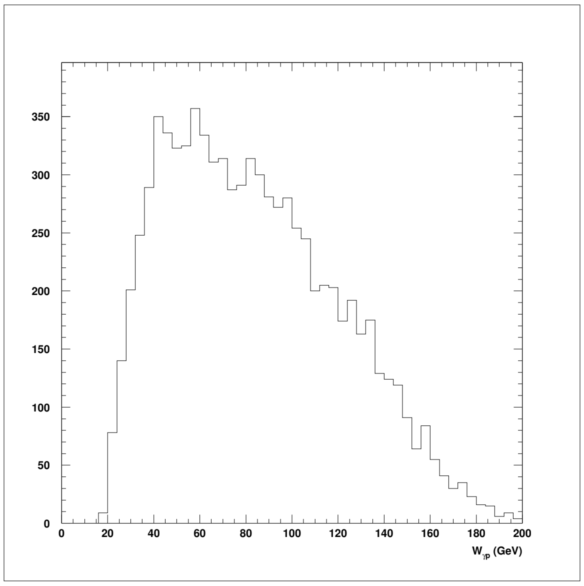

Figure 7.8: $W_{\gamma p}$ distribution for the DIFFVM Monte Carlo, before analysis cuts.

7.1.4 Trigger cut

The final analysis cut that is made is to restrict the events to only those that were triggered by one of the five selected triggers discussed in the triggering section. While this cut reduces the signal as well as the background, it is necessary for a study in which the overall detector trigger efficiency is not well known, and hence normalization of an unselected data set is not possible.

Also applied at this time is a cut on Q^2. Photoproduction is a low-Q^2 process, so we must restrict the events to only those in which the scattered electron is not present in the detector. The minimum Q^2 acceptance of the detector is given by the BEMC, which accepts scattered electrons down to $Q^2 \gtrsim 4\,\mathrm{GeV}^2$. If an electron is detected in the BEMC, its Q^2 is reconstructed. We cut on this reconstructed Q^2:

$$Q^2 < 4\,\mathrm{GeV}^2 \tag{7.3}$$

A decay electron from the J/ψ is unlikely to fake a large Q^2 value, so events that have a decay electron hitting the BEMC will neither give a BEMC trigger, nor be cut by the Q^2 cut. The Q^2 acceptance of the BEMC gives the upper limit on Q^2 for the J/ψ measurement. This limit appears in the flux integral for the cross section (see Eq. 7.6).

Figure 7.9 shows the mass distribution resulting from applying the analysis cuts to the data sample. Now the J/ψ is the dominant feature in the plot, and the underlying background is smooth and nearly linear. Figure 7.10 shows how this distribution breaks down by lepton type and trigger for the subset of events in which both tracks are linked to lepton candidates. The absence of a J/ψ peak in the BEMC-triggered event sample indicates that only low-Q^2 events survive the analysis cuts.

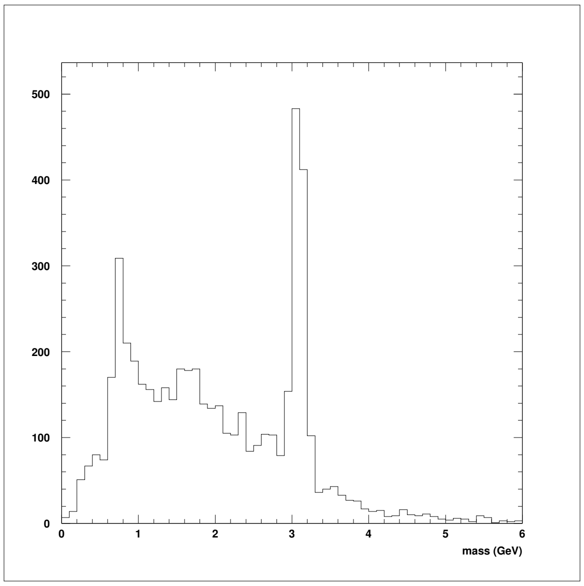

Figure 7.9: Dilepton mass distribution for 1994 data, after analysis cuts.

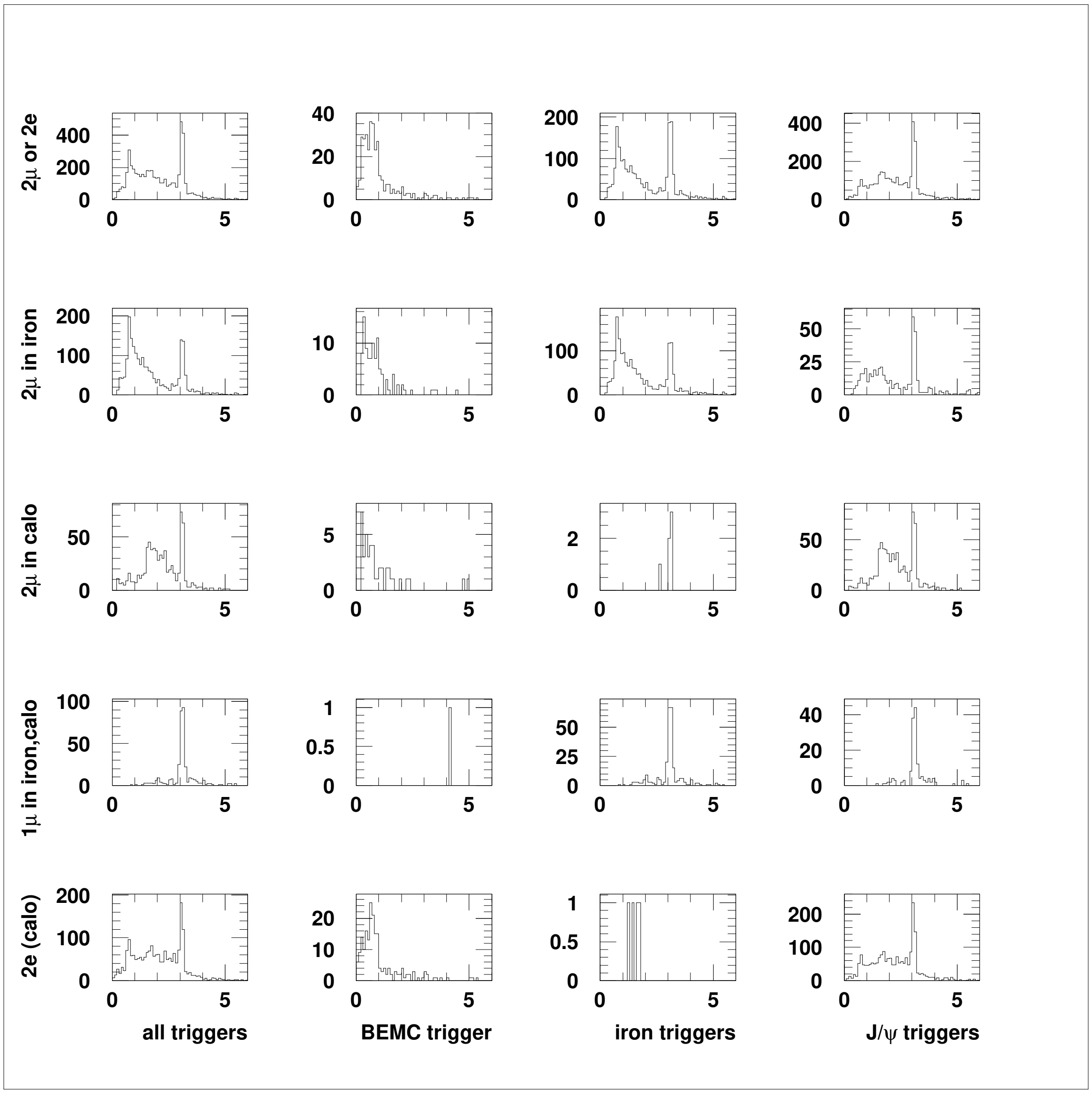

Figure 7.10: Mass distribution for 1994 data, after analysis cuts, by identified leptons and trigger.

7.2 Obtaining a cross section

Before one can extract a cross section from Figure 7.9, the mass distribution must be corrected for known backgrounds, detector acceptance, and trigger efficiencies.

7.2.1 Minimum-bias background

The first background that can be removed is that due to minimum-bias events (generic $\gamma p \to X$ events, which have a cross section of about $160\,\mu$b) that happen to satisfy the trigger, selection, and analysis requirements. Relatively few of these events will have the low multiplicity and tagged lepton that is required. However, these events may enter the data sample via the misidentification of pions as electrons, pions that punch through to the iron yielding false muon signals, and in-flight decays of pions into muons. Fortunately, one does not have to be able to simulate all possible γp events in order to determine their contribution to the data sample. It is a reasonable assumption that oppositely-charged pairs of tracks are generated at the same rate as like-charge pairs by the minimum-bias events. This is not true for genuine two-track events like resonant ρ production, but it should be valid for the high-mass region around the J/ψ. Therefore the mass distribution can be corrected by subtracting the equivalent distribution that uses like-sign pairs of tracks. The like-sign mass distribution is shown in Figure 7.11.

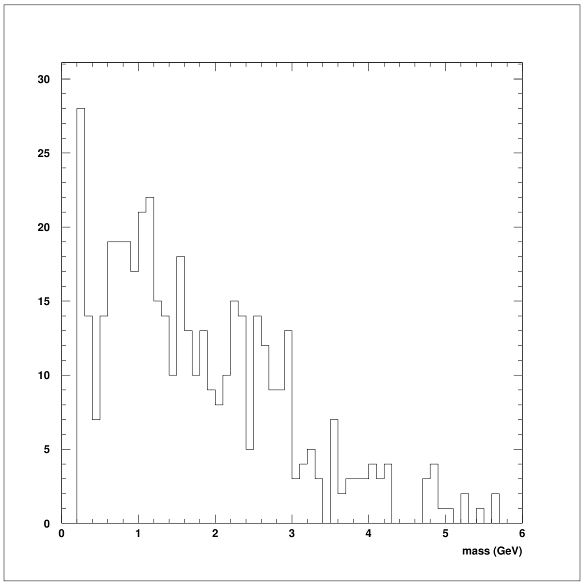

Figure 7.11: Like-sign pair mass distribution for 1994 data, after analysis cuts.

7.2.2 Beam-gas background

The next background that will be considered is that due to the interaction of the beams with the residual gas in the beam pipe of the detector. This is admittedly a small contribution, due to the good vacuum and the lower center-of-mass energy that this essentially fixed-target production has. Thus little background is expected from the electron beam striking the gas. However, the collision of the proton beam with the gas has a center-of-mass energy of 40 GeV (the start of the J/ψ $W_{\gamma p}$ spectrum being studied), and is a pp reaction rather than a γp reaction, giving it a cross section higher by a factor of α_{em}^{-1}. Therefore the beam-gas background must be studied to determine its contribution. It will be an instructive exercise.

Figures 7.12a and 7.12b show the mass distributions for the electron beam on the gas and the proton beam on the gas, respectively, before the analysis cuts are applied. The data come from selecting only pilot (non-colliding) bunches, using the **BEAMTYP** control code. In the 1994 data there were 153 colliding bunches, 15 electron pilot bunches, and 17 proton pilot bunches. Considering that the beam-gas mass distributions would have to be scaled upwards by a factor of 10.2 (9.0 for proton beam on gas) to account for the differing numbers of bunches, it would appear that beam-gas events make a large contribution to the data sample.

a)

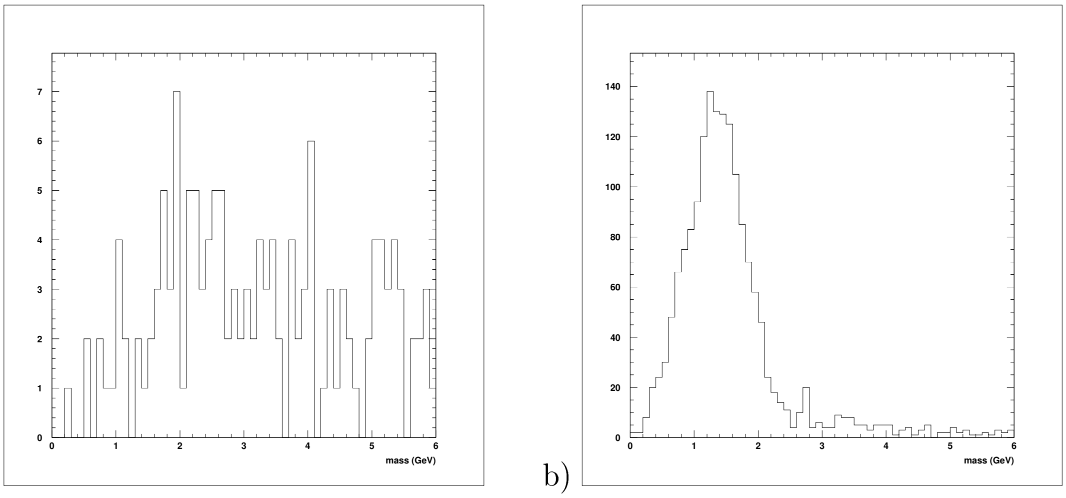

b)

Figure 7.12: Mass distributions for a) electron beam on gas, and b) proton beam on gas, before analysis cuts.

However, Figures 7.13a and 7.13b show the same mass distributions after the analysis cuts have been applied. What has happened? The primary answer is that the cosmic ray cut has removed most of the events. Rather than look at the cos(Θ) distribution, however, it is more instructive to examine a plot of $W_{\gamma p}$ versus mass, as shown in Figures 7.14a and 7.14b.

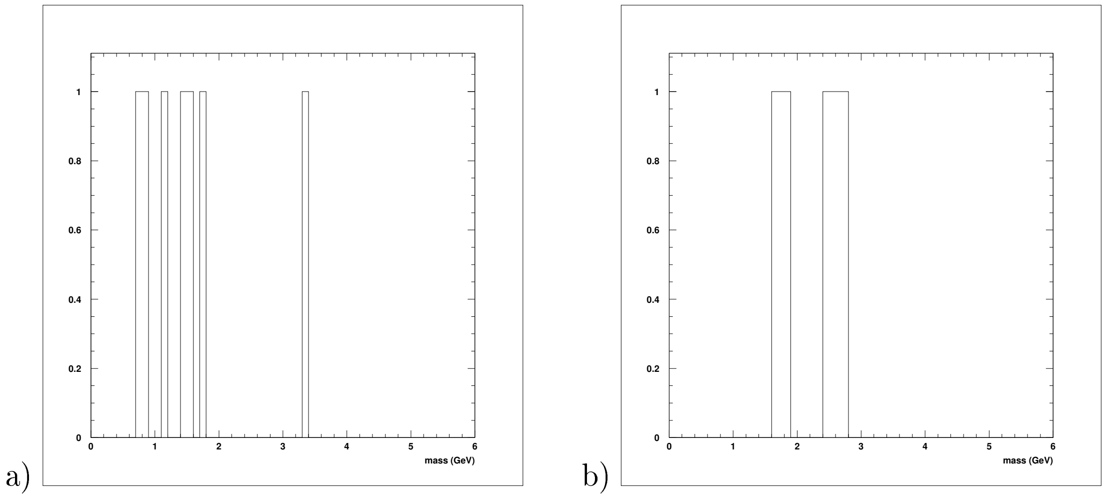

Figure 7.13: Mass distributions for a) electron beam on gas, and b) proton beam on gas, after analysis cuts.

What is striking in these two plots is the band of events extending to high mass. This band can be explained as follows. If we have a cosmic ray passing through the detector, it creates two back-to-back tracks with momenta p_1 and p_2, nearly equal and opposite in magnitude. Thus we appear to have the decay of a body at rest with mass $E_1 + E_2$, or $2E_1$. Likewise, the $W_{\gamma p}^2$ for this body would be $4E_pE_1$, or $2E_pm$. The curve in the plots represents this expected relation for cosmic rays.

The band of cosmic rays is removed by the collinearity cut described previously. The remaining events are either in the backward direction ($W_{\gamma p} > 70\,\mathrm{GeV}$), or in the very forward direction ($W_{\gamma p} < 40\,\mathrm{GeV}$), where they are removed by the

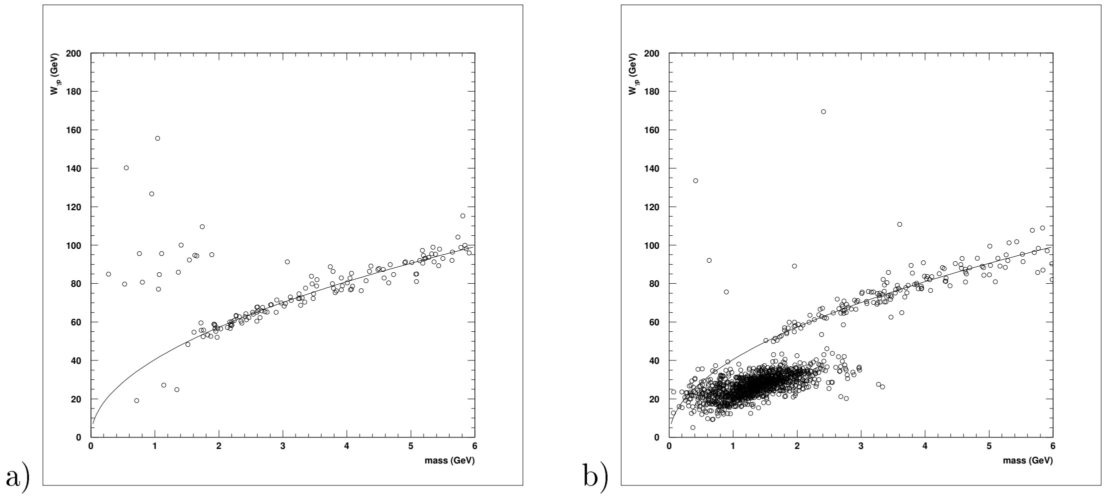

Figure 7.14: $W_{\gamma p}$ vs. mass for a) electron beam on gas, and b) proton beam on gas, before analysis cuts. The curve is the expected relation for cosmic rays.

$W_{\gamma p}$ cut. Since there are essentially no events remaining after all the analysis cuts have been applied, the mass distribution of Figure 7.9 does not need a correction for beam-gas events. However, even no events due to beam-gas will still represent, statistically, a small systematic error, considering the scale factor of 10.

7.2.3 QED background

There is still a significant background left in Figure 7.9, and it is at least partly due to the QED production of dilepton pairs (Eq. 3.10). The cross section for this process can be computed numerically [34], and with the known luminosity the contribution of this process can be calculated. However, since the Monte Carlo provides the shape of the expected background, this expected shape can be scaled and fit to the measured background. Figure 7.15 shows the expected background, after analysis cuts, for $10\,\mathrm{pb}^{-1}$ of luminosity, along with a $1/m^n$ fit. The best fit was achieved with a value of 2.597 ± 0.095 for the parameter n.

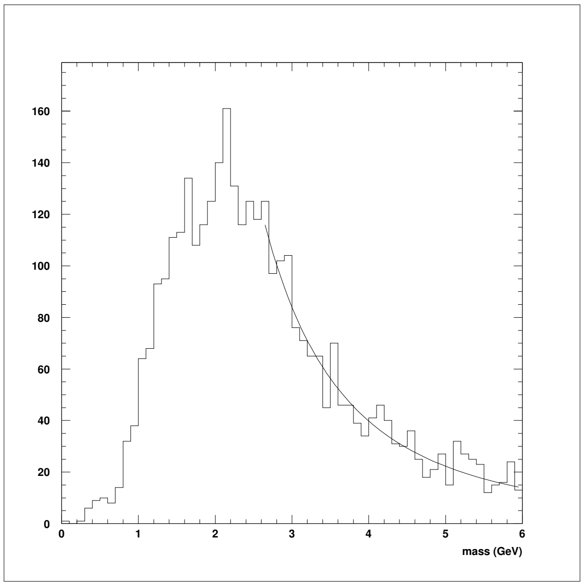

Figure 7.15: Mass distribution, after analysis cuts, for $10\,\mathrm{pb}^{-1}$ of QED pair production. Curve is a fit of the form $1/m^n$.

The fit to the mass distribution is performed in the range of 3.4–6.0 GeV. A χ^2 is computed over the corresponding mass bins as a function of the scale factor. This χ^2 (normalized to the number of bins in the fit) is shown in Figure 7.16. It has a minimum at a scale factor of about 0.27, exactly what is expected for a real luminosity (averaged over the triggers) of $2.7\,\mathrm{nb}^{-1}$.

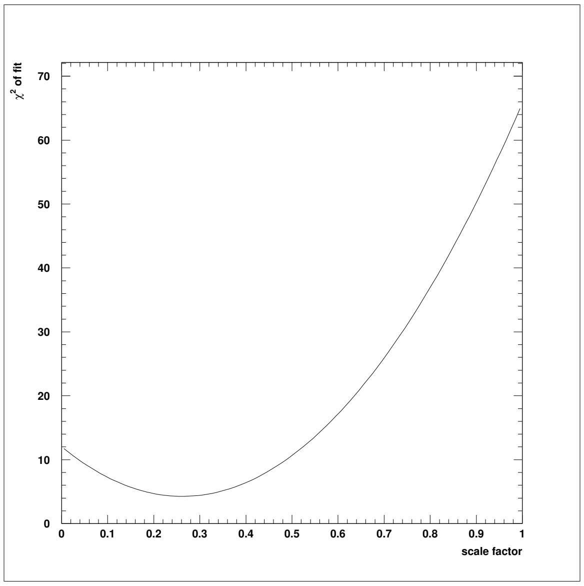

Figure 7.16: χ^2 as a function of scale factor for the fit of the QED (Monte Carlo) mass distribution to that of the data.

7.2.4 Final mass distribution

Figure 7.17 shows the final mass distribution resulting from background subtraction. The high-mass background has been almost completely eliminated. However, there is a significant background remaining under the J/ψ peak. This background is due to a variety of non-quantifiable sources such as pion contamination and muons from in-flight decays. At this point the only thing to do is fit the remaining background (a linear fit is sufficient) and subtract it numerically. It should be noted, however, that in the mass plots for some individual triggers there is no remaining background. The fit peak (a gaussian) has a center of 3.091 ± 0.003 GeV, in excellent agreement with previous measurements [47], and a width of 73.2 ± 2.4 MeV, consistent with that obtained in the DIFFVM Monte Carlo using the known detector momentum resolution.

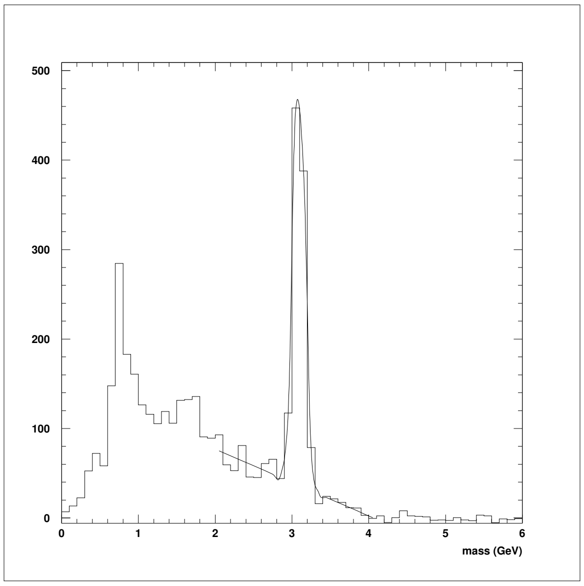

Figure 7.17: Dilepton mass distribution for 1994 data, after analysis cuts and background subtraction. The curve is a fit of a gaussian plus a linear background.

7.2.5 Acceptance and efficiencies

Monte Carlo simulation is used to determine all acceptances and efficiencies. We combine geometric acceptance and trigger efficiency into the products $\epsilon(chan, trig)$, which are calculated for individual triggers and lepton decay channels (e or μ):

$$\epsilon(chan, trig) = \frac{1}{N_{gen}} \sum_i A_i(chan, trig), \tag{7.4}$$

where the sum runs over all N_{gen} events and $A_i(chan, trig)$ is 1 for an event accepted by the specified trigger and 0 otherwise. Global average values of ϵ are also calculated.

Events are binned in $W_{\gamma p}$, which is the most relevant kinematic variable that the acceptance varies over substantially. Figure 7.18 shows how the combined acceptance/efficiency varies over $W_{\gamma p}$. The solid line is the $W_{\gamma p}$ distribution for the generated events, while the dashed line is that for events that are accepted and pass the selection criteria. There are fifty bins in the range of interest ($0\,\mathrm{GeV} < \mathrm{W}_{\gamma\mathrm{p}} < 200\,\mathrm{GeV}$) which can be combined into five bins of 40 GeV width each (the first bin is never used in the analysis).

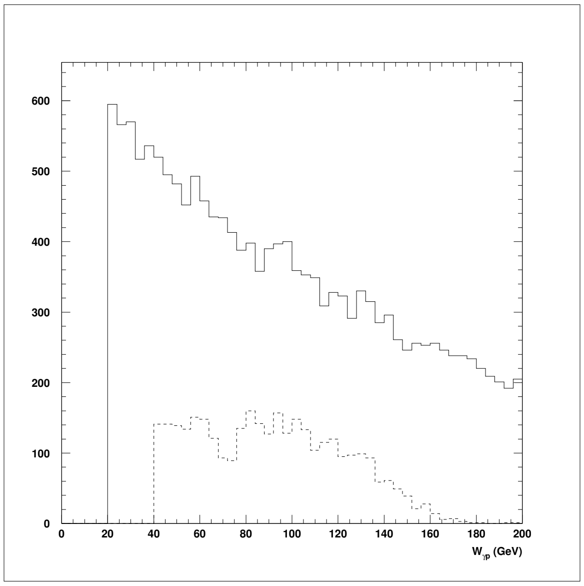

Figure 7.18: $W_{\gamma p}$ distributions from DIFFVM Monte Carlo. The solid line is the generated distribution. The dashed line represents the effects of acceptance and selection efficiency.

7.2.6 Cross section calculation

The total number of events $N_{acc}(chan, trig)$ accepted by a trigger in any particular decay channel is converted to a cross section under the following model:

$$\frac{N_{acc}(chan, trig)}{\mathcal{LB}(chan)} = \int_{y_{min}}^{y_{max}} dy \int_{Q^2_{min}}^{Q^2_{max}} dQ^2 f_{\gamma/e}(y, Q^2)\epsilon(y, Q^2, chan, trig)\sigma_{\gamma p}(y, Q^2) \quad (7.5)$$

where $\mathcal{L}$ is the delivered luminosity, $\mathcal{B}(chan)$ is the branching fraction for the lepton decay channel, and the flux of transverse photons, $f_{\gamma/e}$, is given by

$$f_{\gamma/e} = \frac{\alpha}{2\pi}\frac{1}{yQ^2}\Big(1 + (1-y)^2 - \frac{2m_e^2 y^2}{Q^2}\Big). \quad (7.6)$$

The limits on y are given by

$$y_{min,max} = \frac{W_{\gamma p_{min,max}} + Q^2_{min,max} - m_p^2}{s}, \quad (7.7)$$

and the limits on Q^2 are given by

$$Q^2_{min} = m_e^2\Big(\frac{y^2}{1-y}\Big) \qquad \text{and} \qquad \mathrm{Q}^2_{\mathrm{max}} = 4\,\mathrm{GeV}^2. \quad (7.8)$$

Note that the upper limit on Q^2 is given by the lower edge of acceptance of the BEMC.

If we assume that the γp cross section is independent of y in the specified range, and that its Q^2 dependence is given entirely by the VMD propagator term:

$$\sigma_{\gamma p}(y, Q^2) = \sigma_0\Big(\frac{m^2_{J/\psi}}{m^2_{J/\psi} + Q^2}\Big)^2, \quad (7.9)$$

then we can rewrite Eq. 7.5 as

$$N_{acc}(chan, trig) = \mathcal{LB}(chan)\sigma_0\Phi_{acc}(chan, trig) \quad (7.10)$$

where

$$\Phi_{acc}(chan, trig) = \int_{y_{min}}^{y_{max}} dy \int_{Q^2_{min}}^{Q^2_{max}} dQ^2 f_{\gamma/e}(y, Q^2) \Big(\frac{m^2_{J/\psi}}{m^2_{J/\psi} + Q^2} \Big)^2 \epsilon(y, Q^2, chan, trig) \tag{7.11}$$

is the flux accepted by a specific trigger for a specific decay channel.

Finally, we can approximate Φ_{acc} with the relation

$$\Phi_{acc}(chan, trig) \simeq \epsilon(chan, trig)\Phi, \tag{7.12}$$

where $\epsilon(chan, trig)$ is obtained via Monte Carlo (Eq. 7.4) and the total flux

$$\Phi = \int_{y_{min}}^{y_{max}} dy \int_{Q^2_{min}}^{Q^2_{max}} dQ^2 f_{\gamma/e}(y, Q^2) \Big(\frac{m^2_{J/\psi}}{m^2_{J/\psi} + Q^2} \Big)^2 \tag{7.13}$$

is obtained by numerical integration. Thus we have the cross section

$$\sigma_{\gamma p}(Q^2 = 0) = \sigma_0 = \frac{N_{acc}(chan, trig)}{\mathcal{L}\mathcal{B}(chan)\epsilon(chan, trig)\Phi} \tag{7.14}$$

which can be obtained from each trigger and decay channel combination, or as a global average.

7.2.7 Dissociative contamination

Until this point, what has not been addressed is the issue of contamination of the elastic sample by proton dissociative events in which the proton fragments do not appear in the trackers. However, some fraction of the proton dissociative events will deposit energy in the detector's most forward components, such as the plug calorimeter. Figures 7.19a and7.19b show the predicted distribution of plug energies for the proton dissociative DIFFVM events before and after all analysis cuts. Note that the Monte Carlo simulation does not include noise in the plug, so it is not possible to safely assume that any energy deposited in the plug indicates a dissociative event.

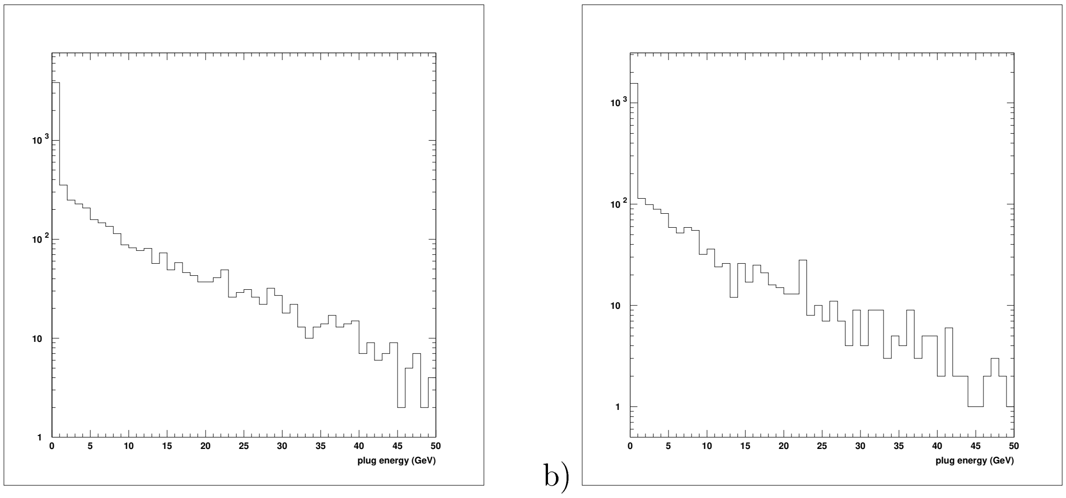

a) b)

Figure 7.19: Plug energy for proton dissociative events from the DIFFVM Monte Carlo a) before analysis cuts and b) after analysis cuts.

However, cosmic ray events can give a good indication of the noise in the plug. Unfortunately, some real dissociative events will look like cosmic ray events and contaminate this sample. This contamination can be minimized by looking at cosmic ray events in the beam-gas samples. Figures 7.20a and 7.20b show the plug energy distribution for the cosmic ray selection in the electron beam-gas and proton beam-gas samples, respectively. These figures show that a cut on plug energy at

5.0 GeV would not disturb the elastic sample, while removing some fraction of the dissociative events.

$$\begin{aligned} E_{plug} &< 5\,\text{GeV} \qquad \text{for elastic plus some diffractive events} \\ E_{plug} &> 5\,\text{GeV} \qquad \text{for pure diffractive events} \end{aligned} \tag{7.15}$$

a) b)

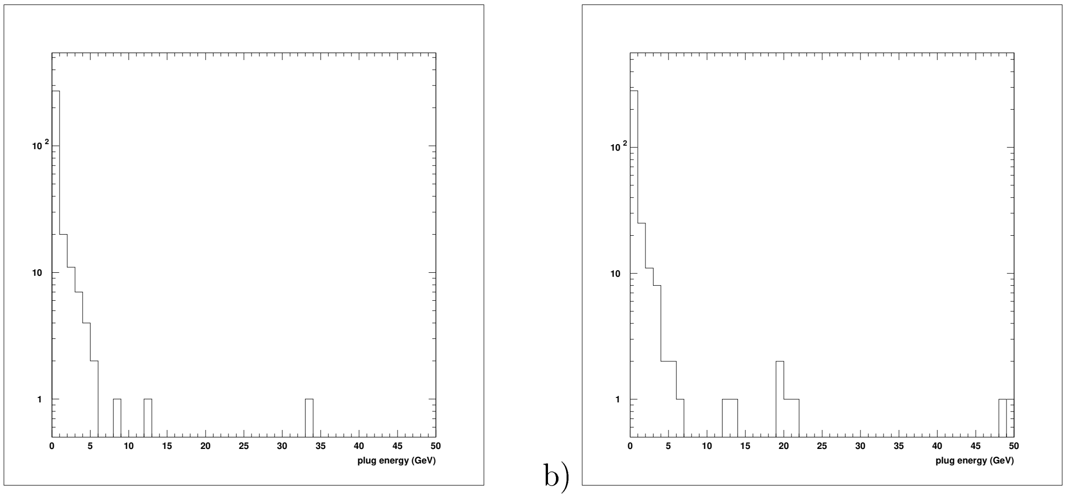

Figure 7.20: Plug energy for cosmic ray events in a) the electron beam-gas sample, and b) the proton beam-gas sample.

Applying this plug energy cut to the DIFFVM Monte Carlo, one finds that the ratio of all dissociative events to cut dissociative events (denoted by R_{cut}) is 3.96 ± 0.10 before analysis cuts are made, and 4.13 ± 0.16 after analysis cuts. Now the following analysis can be made: if there are N_D dissociative events in the data, and the plug energy cut removes N'_D of them, then $N_D - N'_D$ remain. Thus, if we know we have cut N'_D events, we know that there are still $N'_D(\frac{N_D}{N'_D-1})$ dissociative events remaining. If we assume that the Monte Carlo gives a good representation of the plug energy distribution for dissociative events, then the ratio $R_{cut} = \frac{N_D}{N'_D}$ will be the same for Monte Carlo and for data. Examination of the events from Figure 7.9 shows that applying the plug energy cut would remove 608 of the 5315 events. Thus there are a total of $R_{cut}(\frac{N_D}{N'_D}) = 2511$ dissociative events in the sample, or 47%. We define R to be the ratio of dissociative to elastic events, and see that R is nearly one.

Now that we know the amount of dissociative contamination in the data sample, it would be possible to subtract off the corresponding number of events. However, if we wish to extract physics information about the dissociative sample, we can treat each event as if it were a mixture of dissociative and elastic events with ratio R. Thus the definition of $\epsilon(chan, trig)$ from Eq. 7.4 is modified to

$$\epsilon(chan, trig) = \left(\frac{1}{1+R}\right)\epsilon(elas, chan, trig) + \left(\frac{R}{1+R}\right)\epsilon(diss, chan, trig). \quad (7.16)$$

Then each event can be given a weight of $\frac{R}{1+R}$, representing the (averaged) dissociative contribution. Note that this same procedure can be used for the elastic component of the data sample, in cases where simple subtraction of events is not meaningful.

7.2.8 ψ' contamination

Another, albeit smaller, source of contamination of the data sample is the production of the ψ' particle, which can decay into a J/ψ and neutral particles. These events will be impossible to distinguish from J/ψ photoproduction events, so the contamination must be estimated and subtracted. Figure 7.21 shows proof that the ψ' is being produced. It is the final (*i.e.* after cuts) mass plot for dimuon events that are triggered by the iron barrel subtrigger. The smaller peak is the ψ', which has a mass [47] of 3.686 GeV. The fit gives the center of the second gaussian to be 3.676 GeV, in good agreement with that value. The ψ' has a dileptonic branching ratio of about 10% that of the J/ψ, so large numbers of these particles are being created.

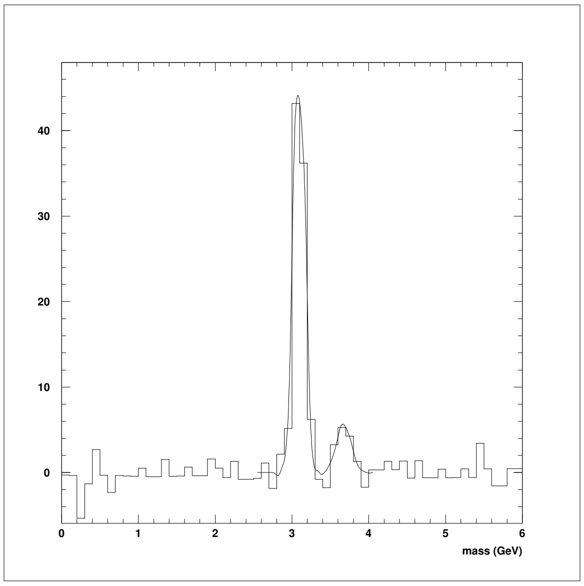

Figure 7.21: Mass of dimuon events triggered by the iron barrel subtrigger. The solid line is a fit of two gaussians.

To determine the amount of contamination from the ψ', assume that N and N' are the number of J/ψ and ψ' particles produced. Then the number of J/ψ particles coming from ψ' decays is $N'' = N'\mathcal{B}''$, where $\mathcal{B}''$ is the branching ratio of the ψ' into a J/ψ plus neutral particles ($23.2\% \pm 2.6\%$). The total number of accepted J/ψ events is $N_{acc} = N\epsilon\mathcal{B} + N'\mathcal{B}''\epsilon\mathcal{B}$, where ϵ is the acceptance and $\mathcal{B}$ is the branching ratio of the J/ψ into dimuons ($5.97\% \pm 0.25\%$). Likewise, the total number of accepted ψ' events is $N'_{acc} = N'\epsilon'\mathcal{B}'$, where $\mathcal{B}'$ is the branching ratio of the ψ' into dimuons ($0.77\% \pm 0.17\%$). So, to recover the correct number of photoproduced J/ψ particles, we must use the formula

$$\begin{aligned}
N &= \frac{1}{\epsilon\mathcal{B}}(N_{acc} - N'\mathcal{B}''\epsilon\mathcal{B}) \\
&= \frac{1}{\epsilon\mathcal{B}}\left(N_{acc} - \frac{1}{\epsilon'\mathcal{B}'}(N'_{acc}\mathcal{B}''\epsilon\mathcal{B})\right) \\
&= \frac{1}{\epsilon\mathcal{B}}\left(N_{acc} - N'_{acc}\frac{\epsilon}{\epsilon'}\frac{\mathcal{B}\mathcal{B}''}{\mathcal{B}'}\right) \qquad (7.17)
\end{aligned}$$

which, if we assume that $\epsilon = \epsilon'$, reduces to

$$N = \frac{1}{\epsilon\mathcal{B}}N_{acc}\left(1 - \frac{N'_{acc}}{N_{acc}}\frac{\mathcal{B}\mathcal{B}''}{\mathcal{B}'}\right). \qquad (7.18)$$

The ratio of branching fractions evaluates to 1.80 ± 0.45. Now, if we assume that the ratio $\frac{N'_{acc}}{N_{acc}}$ is the same for all triggers and channels, then we can correct each mass plot by the ratio obtained in Eq. 7.18 from Figure 7.21, which comes out to be 0.617.

Unfortunately, this last assumption about $\frac{N'_{acc}}{N_{acc}}$ turns out not to be true. As an example, the mass plot in Figure 7.22 (muons in the iron endcap) has much higher statistics than that in Figure 7.21, yet shows no discernible ψ' peak. As a matter of fact, a ψ' peak is not visible in the mass plot for any other subdetector. What makes the iron barrel subdetector special in this case is that its efficiency changes rapidly with respect to the p_t of the decay muons. Recall that a muon needs about 1.5 GeV to pass through the calorimeter and coil to reach the iron. Thus, the decay muons from the J/ψ are essentially at threshold. The extra p_t given to the decay muons of the ψ' (or of the J/ψ from the ψ') is enough to make the detector much more efficient for them.

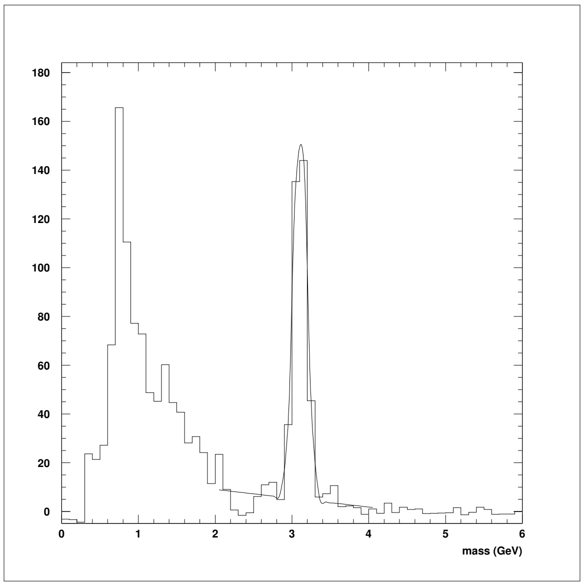

Figure 7.22: Mass of dimuon events triggered by the iron endcap subtrigger.

Therefore, only an estimate of the ψ' contamination can be made. First we assume that ϵ and ϵ' are equal. This is not true for the iron barrel subdetector but it is a reasonable estimate for the detector on average. Second, we assume that the previously measured ratio [5] of diffractive cross sections

$$\frac{\sigma_{\psi'}}{\sigma_{\psi}} = 0.20 \pm 0.05 \tag{7.19}$$

is valid for elastic production at HERA energies. These two assumptions allow us to simplify the previous equations. In short, if N_{acc} J/ψ particles are accepted into the final data sample, then there will be an additional N'_{acc} J/ψ events due to ψ'

production and decay into J/ψ. That number is given by

$$N'_{acc} = \frac{\epsilon'\sigma'\mathcal{B}''}{\epsilon\sigma} N_{acc} = 0.046 N_{acc}. \tag{7.20}$$

Thus the total number of events must be corrected by a factor of $1/1.046 = 0.956$. The uncertainty on that factor is 27%.

7.2.9 Systematic errors

The systematic error on the total number of J/ψ events is due to two sources. First, the shape of the J/ψ peak is assumed to be gaussian, whereas in fact there is a slight tail in the low-mass direction due to decay electrons losing energy within the tracking volume. This tail is well-reproduced in the Monte Carlo, which indicates that the gaussian fit underestimates the number of entries by 6%. The second source is the subtraction of the flat background that remains in the final mass plot. This subtraction is performed by fitting a gaussian plus a linear background to the mass distribution. Thus an error in the linear fit to the background would introduce an additional error in the total number of entries in the peak. A reasonable estimate of this error is given by taking the square root of the number of subtracted entries, which by visual inspection is about 160. There are 900 entries in the peak, so 13 events is less than a 2% error. Thus the total systematic error on the number of J/ψ events is 6%.

The extraction of the number of elastic events introduces additional uncertainty. The number of elastic and dissociative events, N_E and N_D respectively, are determined by the equations

$$\begin{aligned} N_E &= N_T - N_D \qquad \text{and} \\ N_D &= R_{cut} N_{cut}, \end{aligned} \tag{7.21}$$

where N_T is the total number of events and N_{cut} is the number of tagged dissociative events. Thus the statistical error on N_D is governed by the statistical error on N_{cut}, and its systematic error is derived from the uncertainty in R_{cut}. The errors on N_E are given by adding the absolute errors on N_T and N_D in quadrature.

The error in the determination of R_{cut} is small (4% for the global selection) and purely due to Monte Carlo statistics. However, since the efficiency for tagging dissociative events is small, there are few tagged events, and N_{cut} is small, with a large statistical uncertainty. Thus the extracted numbers of elastic and dissociative events have relatively large statistical errors, but small systematic errors.

The statistical error on ψ' contamination is the scaled statistical error on the elastic component of the data sample. The systematic error is given by the uncertainty in the measured cross sections and branching ratios, as discussed in the section on ψ' contamination. These absolute errors contribute to the uncertainty in the corrected number of events by adding quadratically. Since they are so much smaller, they make no difference in the uncertainty.

The global efficiency includes acceptance and efficiency factors (ϵ), as well as the branching ratio $\mathcal{B}$ of the J/ψ into dileptons. Multiplying the corrected number of events by the global efficiency gives the total number of J/ψ particles produced. The uncertainty in ϵ is governed by the number of events used in the Monte Carlo. This is combined in quadrature with the error in the branching ratio $\mathcal{B}$ to give the total systematic error.

The cross section σ_{ep} is given by taking the total number of J/ψ particles produced and dividing by the total luminosity delivered. A systematic error of 5% was given to all luminosity measurements. Thus the errors for the cross section combine those of the corrected number of events, the global efficiency, and the luminosity. Converting to the γp cross section requires division by the flux integral.

The total γp flux integral Φ (Eq. 7.13) is evaluated numerically by dividing the $log(y), log(Q^2)$ area into bins and summing up the individual contributions. With enough subdivisions (typically 1000x1000) the integral can be computed with high precision. Hence the error due to the calculation is essentially zero. However, a more reasonable estimate of the systematic error introduced by the flux calculation is the difference between calculating Φ with and without the VMD propagator included. The VMD factor in Φ comes from assuming the VMD model, which may or may not be valid. The difference due to this factor was calculated to be 4%. That the difference is small is not surprising since for most of the Q^2 range the factor is nearly 1.

7.2.10 Final cross section

Integrating the gaussian peak of Figure 7.17 and correcting for dissociative and ψ' contamination gives a total of $N_{acc} = 533 \pm 48 \pm 56$events. This converts to a photoproduction cross section of $\sigma_{\gamma p} = 69.2 \pm 6.2 \pm 12.4\,\mathrm{nb}$. The equivalent procedure is repeated for three of the four $W_{\gamma p}$ bins (the highest bin had insufficient statistics), yielding the cross section as a function of $W_{\gamma p}$. Table 7.3 summarizes the cross section calculations, and Figure 7.23 shows the cross section measurements with respect to $W_{\gamma p}$.

Cross Section Calculation	
$W_{\gamma p}$ range (GeV)	40–200
Total events	900 ± 30 ± 54
Dissoc. contribution	341 ± 38 ± 13
Elastic contribution	559 ± 48 ± 56
ψ' contribution	26 ± 2 ± 7
Corrected events	533 ± 48 ± 56
Global eff. $\mathcal{B}\epsilon$	0.0267 ± 0.0027 ± 0.1
Cross section σ_{ep} (nb)	8.93 ± 0.81 ± 1.60
Total flux Φ	0.1296 ± 0.0 ± 0.0042
Cross section $\sigma_{\gamma p}$ (nb)	69.2 ± 6.2 ± 12.4

Cross Section Calculation			
$W_{\gamma p}$ range (GeV)	40–80	80–120	120–160
Total events	377 ± 19 ± 23	361 ± 19 ± 22	168 ± 13 ± 10
Dissoc. contribution	188 ± 28 ± 13	102 ± 20 ± 6	78 ± 18 ± 7
Elastic contribution	188 ± 34 ± 26	258 ± 28 ± 22	91 ± 22 ± 12
ψ' contribution	9 ± 2 ± 3	12 ± 1 ± 3	4 ± 1 ± 1
Corrected events	180 ± 34 ± 26	247 ± 28 ± 23	87 ± 22 ± 12
Global eff. ϵ	0.0339 ± 0.0 ± 0.0031	0.0433 ± 0.0 ± 0.0039	0.0254 ± 0.0 ± 0.0032
Cross section σ_{ep} (nb)	2.39 ± 0.45 ± 0.62	2.56 ± 0.29 ± 0.46	1.53 ± 0.40 ± 0.50
Total flux Φ	0.0666 ± 0.0 ± 0.0019	0.0326 ± 0.0 ± 0.0011	0.0192 ± 0.0 ± 0.0007
Cross section $\sigma_{\gamma p}$ (nb)	35.8 ± 6.8 ± 9.4	78.4 ± 8.8 ± 14.2	79.7 ± 20.6 ± 26.0

Table 7.3: Summary of cross section calculations for 1994 data run. The first error is statistical, the second is systematic.

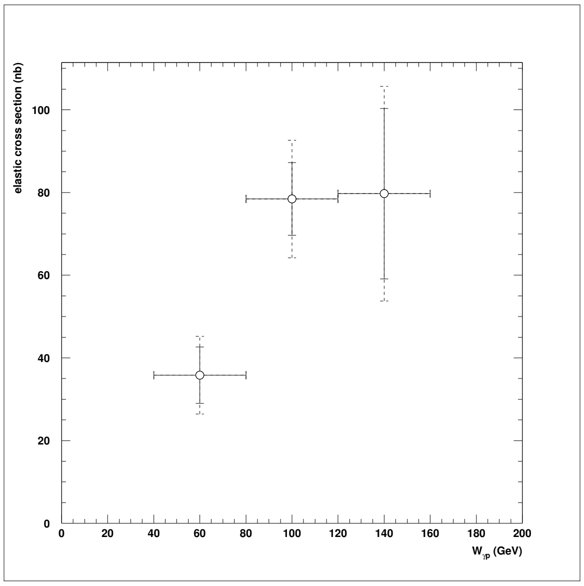

Figure 7.23: Measured J/ψ photoproduction cross section $\sigma_{\gamma p}$ as a function of $W_{\gamma p}$.

7.2.11 Final Analysis

Figure 7.24 shows the new cross section measurements along with results from lower energy experiments [4, 6, 7, 8, 9, 12, 15], which have been summarized in a review paper [16], and the Zeus [17] and H1 [18] collaborations. Also included in the figure are the VMD predictions (see Eq. 3.3) for the behavior of the cross section with respect to $W_{\gamma p}$, assuming a fixed value of b and normalized to the low-energy data point of the E516 experiment. Clearly, using the standard value of $\epsilon = 0.08$, VMD fails to predict the rapid increase in cross section. A much higher value of $\epsilon = 0.19$ is needed to provide a good visual fit to the data. Using this value would lead to a poor agreement with the large set of data below 10 GeV.

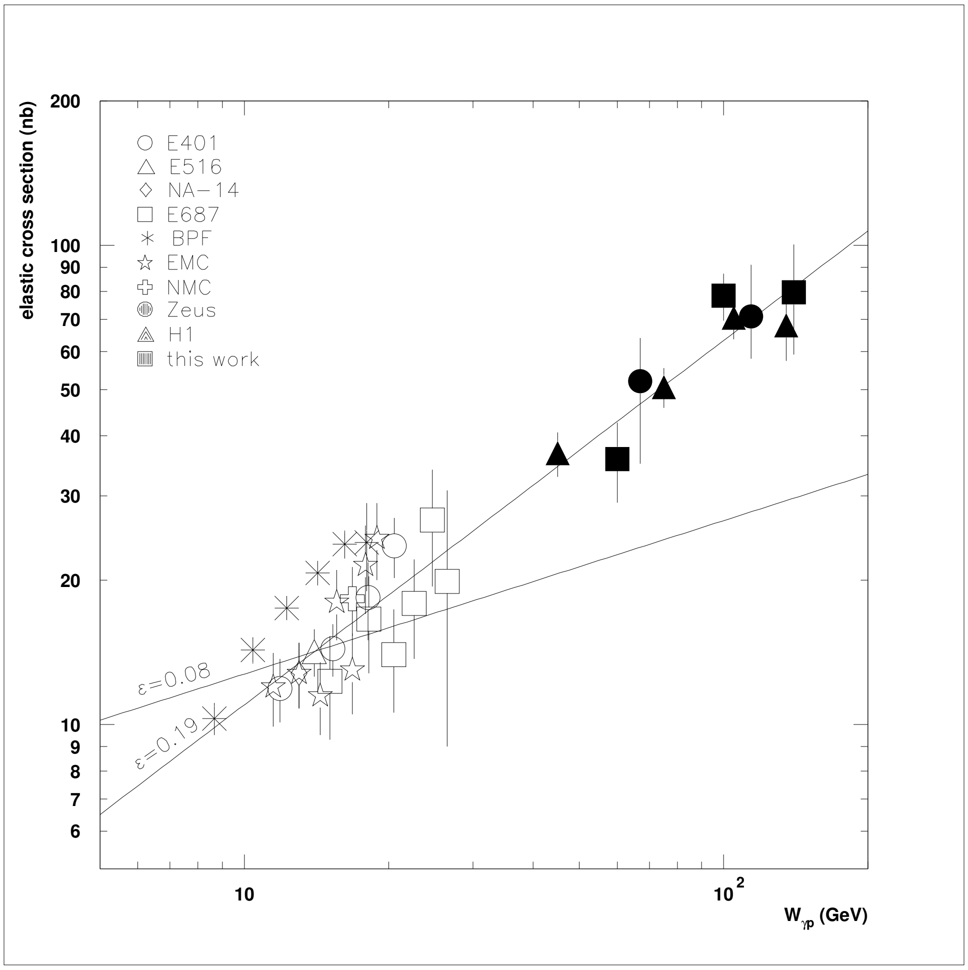

Figure 7.24: J/ψ photoproduction cross section $\sigma_{\gamma p}$ as a function of $W_{\gamma p}$, as measured by several experiments. The solid lines are predictions from VMD, using values of ϵ of 0.08 and 0.19 and normalized to the E516 data point.

Recently, however, a new perturbative QCD treatment [48], using the new gluon structure functions [46] from recent H1 and Zeus data, has been shown to correctly describe the $W_{\gamma p}$ behavior of the photoproduction cross section [18]. Specifically, the MRS(G) gluon distribution appears to be ruled out, while the MRS(A') and GRV sets fit the data, with the MRS(A') gluon slightly favored. This is the first time that the J/ψ photoproduction cross section has been used to discriminate between gluon distributions at the low-x values obtainable at HERA.

7.3 t distribution

The analysis of the t distribution follows much of the analysis for the mass distribution. Figure 7.25 shows the t distribution (calculated using the p_t^2 of the J/ψ) for all selected events that pass the analysis cuts. Note that, with the exception of the first bin, the low-t events are distributed exponentially, as is expected for a diffractive process. As before, this distribution must be corrected for backgrounds, detector acceptance and efficiencies, and contamination from processes other than elastic photoproduction.

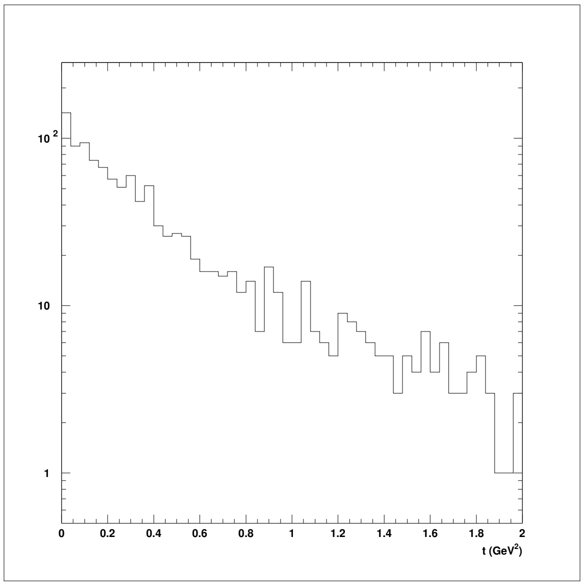

Figure 7.25: Dilepton t distribution for 1994 data, after analysis cuts.

7.3.1 Background subtraction

First, background subtraction of minimum-bias events using the like-sign data sample is performed. As before, beam-gas background subtraction is not performed due to the low number of these events. For the QED background, we do not have the benefit of having two distinct distributions for signal and background, so it would seem to be unclear by how much to scale the simulated QED background for the subtraction. The solution to this problem is to use the same scale factor that was obtained by fitting the mass distribution. Thus if the data indicates that the $10\,\mathrm{pb}^{-1}$ Monte Carlo mass distribution must be scaled by a factor of 0.24 in order to fit the high-mass region, then the t distribution from the Monte Carlo must be scaled by the same factor. The result of the background subtractions is shown in Figure 7.26a, which has an exponential fit to the low-t region. Note that the first bin has now been corrected (by the QED subtraction) and is intersected by the fit.

Next, the t distribution must be corrected for contamination by dissociative events. This is done by generating a t distribution, equivalent to Figure 7.26a, for dissociative-tagged events (see Eq. 7.15). The t distribution for these events is shown in Figure 7.26b. This shape is then scaled by the ratio of total events to cut events R_{cut}, and subtracted from the non-dissociative-tagged distribution, leaving a t distribution for purely elastic events (Figure 7.27).

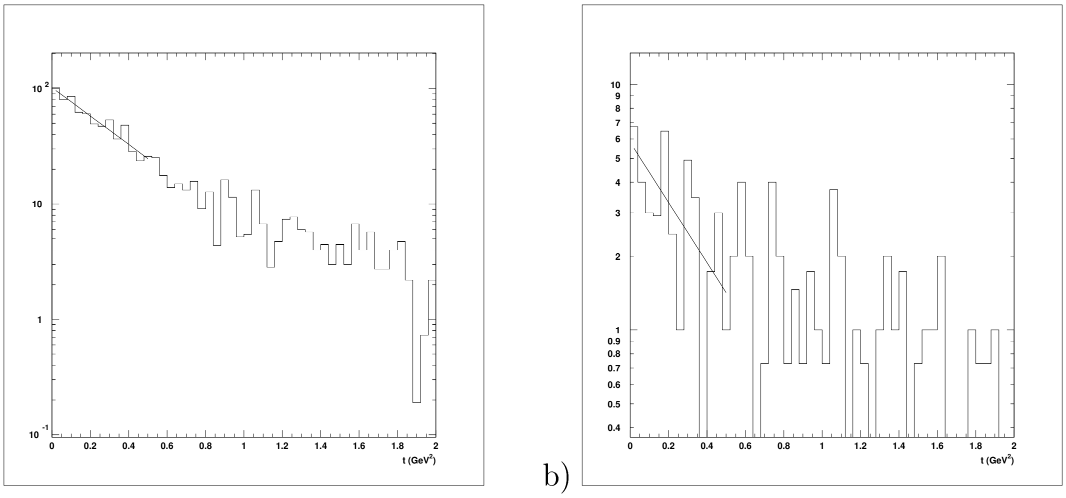

a) b)

Figure 7.26: Dilepton t distribution for 1994 data, after analysis cuts and background subtraction, for a) standard event selection and b) dissociative event selection. The solid lines are exponential fits.

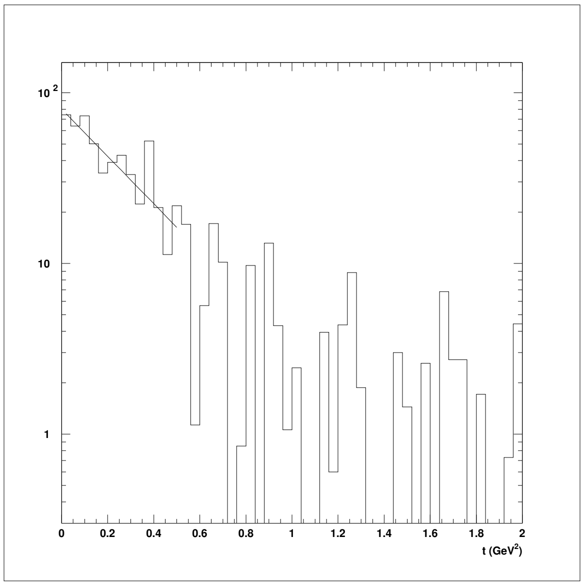

Figure 7.27: Dilepton t distribution for elastic events. The solid line is an exponential fit.

7.3.2 Acceptance and efficiencies

In order to obtain the actual t distribution, the shape of Figure 7.27 must be corrected for detector acceptance and efficiency. This is done in the same manner as

Eq. 7.4, where ϵ is now a function of t as well. Global efficiencies are also calculated. The resulting efficiency curve is given in Figure 7.28.

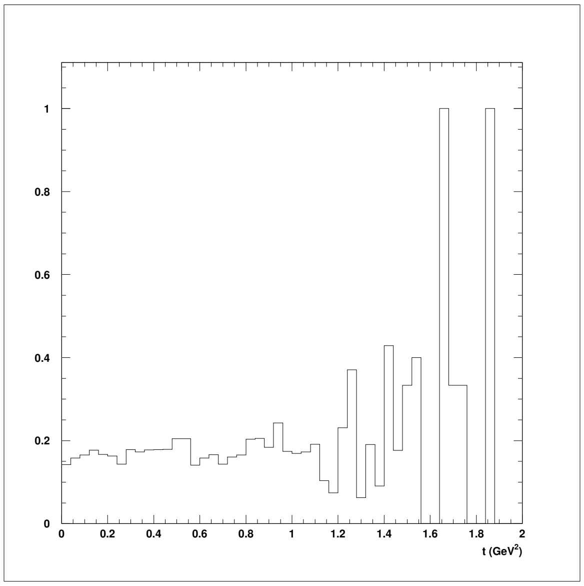

Figure 7.28: Global efficiency for elastic events as a function of t.

7.3.3 Analysis

The final t distribution is given in Figure 7.29. The exponential shape in the low-t region is consistent with a diffractive model of J/ψ photoproduction. An exponential fit to this region gives a slope of $3.67 \pm 0.39 \pm 0.15\,\mathrm{GeV}^{-2}$. The first error is statistical, while the second error is systematic and was obtained by varying the upper range of the fit. The fit is sensitive only in the higher-p_t direction, which has lower statistics. The exponential nature of the p_t distribution indicates the diffractive nature of elastic J/ψ production. Using the 'black disk' model (Eq. 3.6) and the conversion constant of $\bar{h}c = 0.197\,\mathrm{GeV\,fm}$, a radius of 0.755 fm is obtained.

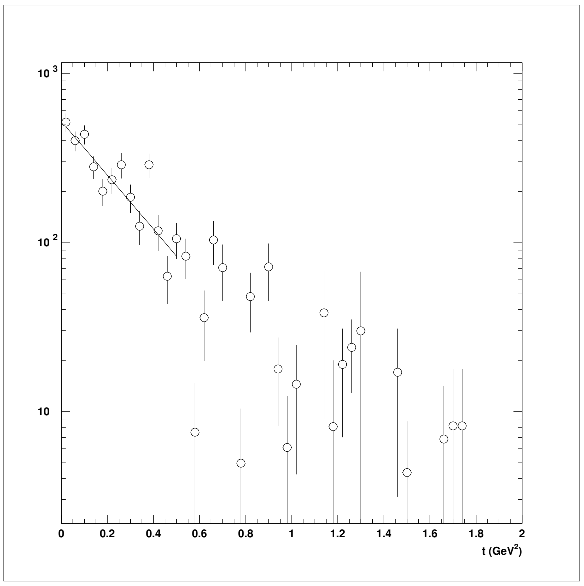

Figure 7.29: Dilepton t distribution for 1994 data, after analysis cuts and background subtraction, and corrected for dissociative contamination. The solid line is an exponential fit.

The slope is also calculated for the t distributions obtained in the separate $W_{\gamma p}$ bins. These results, as well as measurements of b from lower energy experiments [4, 6, 7, 9, 12, 15, 16] and the Zeus [17] and H1 [18] collaborations, are shown in Figure 7.30. As can be seen, the low-energy data is in disagreement, and uncertainties in the high-energy measurements are large enough that no definite statement can be made as to the development of b with respect to energy. Note that Eq. 3.5 predicts an increase of only about $2\,\mathrm{GeV}^{-2}$ over the entire range of $W_{\gamma p}$ of these measurements. This is shown by the solid line in the plot, normalized to the NA-14 data point.

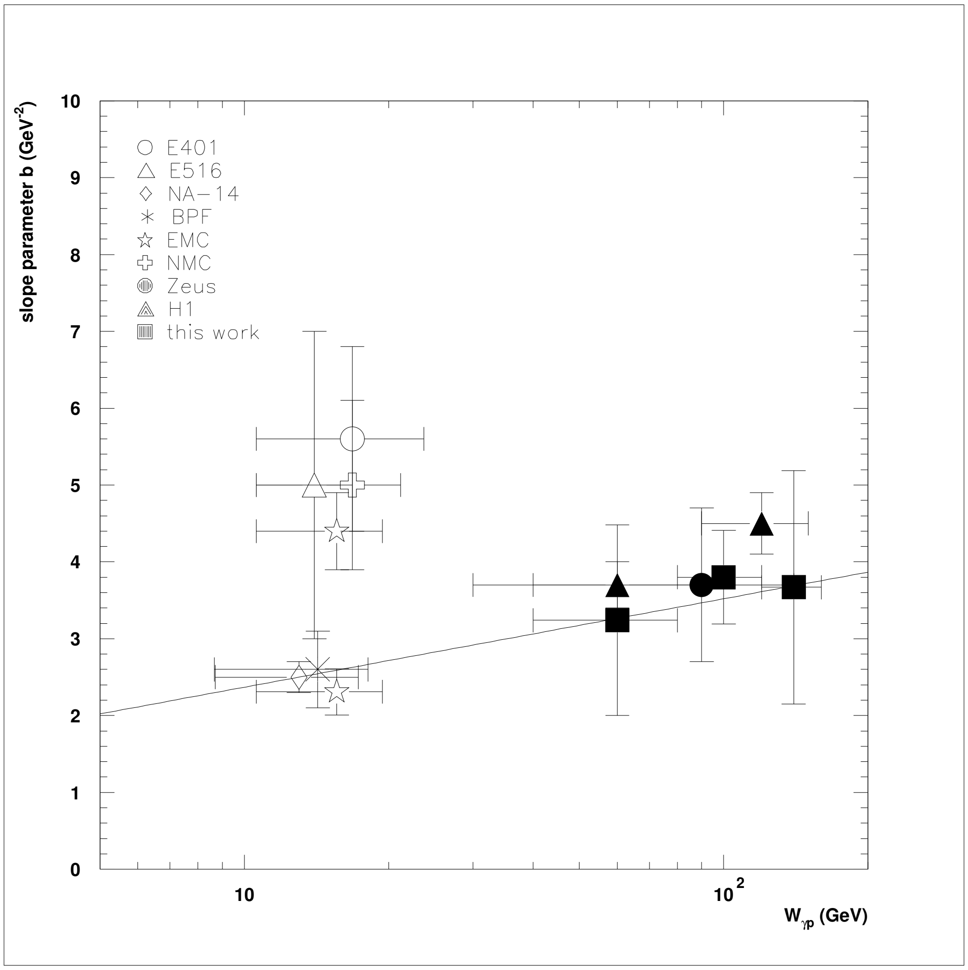

Figure 7.30: The t distribution slope parameter b as a function of $W_{\gamma p}$, as measured by several experiments. The solid line is the prediction of the shrinkage effect, normalized to the NA-14 data point.

7.4 High Q^2 events

It is of some interest to explore the elastic production of J/ψ at large Q^2. This is not strictly speaking the kinematic region of photoproduction, which is a low-Q^2 process. However, it can certainly be described with perturbative QCD methods, and in fact the PQCD model previously discussed in the section on J/ψ photoproduction models should also be valid at large Q^2. In particular, the shape of the high-Q^2 distribution 3.8 is a good prediction to test.

A high-Q^2 elastic J/ψ data sample was extracted following the same procedure as the low-Q^2 analysis, with the sole exception that the cut on reconstructed Q^2 (see Eq. 7.3) was reversed, thereby only accepting events with $Q^2 > 4\,\mathrm{GeV}^2$. Figure 7.31 shows the final mass distribution for the high-Q^2 event sample. The ρ and J/ψ peaks are dominant, with a small low-mass background. Minimum-bias, beam-gas, and QED processes were seen to have negligible contribution to the background.

Figure 7.32 shows the Q^2 distribution for the J/ψ peak (masses of 2.8 GeV to 3.4 GeV) in the high-Q^2 event sample. A fit of the form $1/Q^n$ has been performed for the region above $5\,\mathrm{GeV}^2$. This fit yields a value of 2.17 ± 0.21, which indicates a Q^{-4} dependence.

The Q^2 distribution of Figure 7.32 was corrected for dissociative contamination and the effects of acceptance. The resulting distribution is shown in Figure 7.33.

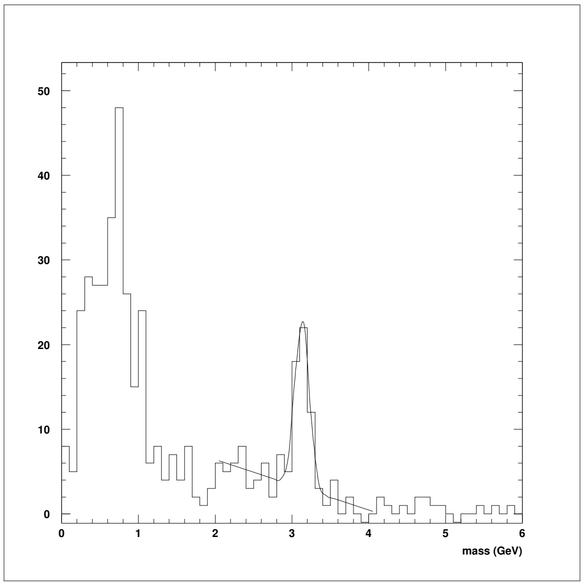

Figure 7.31: Dilepton mass distribution for the high-Q^2 event sample, after analysis cuts. The solid line is a fit of a gaussian plus a linear background.

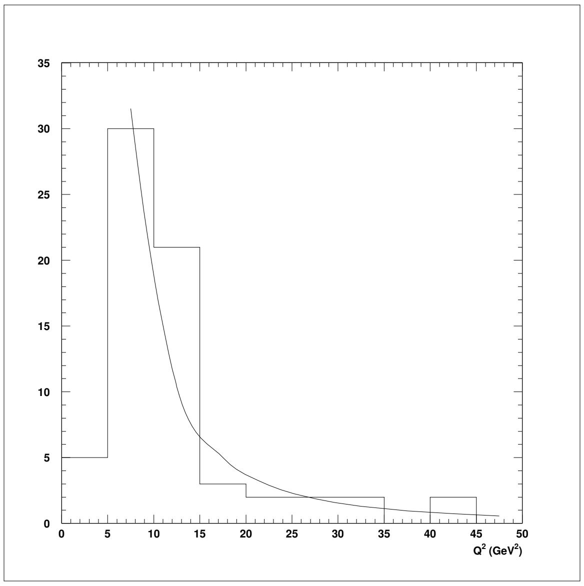

Figure 7.32: Q^2 distribution for the J/ψ peak of the high-Q^2 event sample, after analysis cuts. Curve is fit of the form $1/Q^n$.

The $1/Q^n$ fit has once again been performed, resulting in a value of $2.12 \pm 0.26$for n.

The dashed and dotted lines are fits of the form $1/Q^2$ and $1/Q^6$, respectively. The data clearly favor a Q^{-4} dependence.

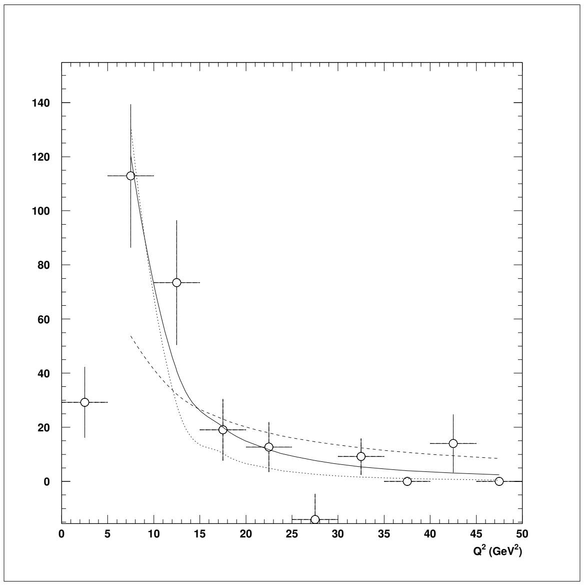

Figure 7.33: Q^2 distribution for the J/ψ peak of the high-Q^2 event sample, after analysis cuts, and corrected for dissociative contamination and acceptance effects. Curve is fit of the form $1/Q^n$.

Chapter 8

Conclusion

The cross section for the elastic photoproduction of J/ψ has been measured and found to be inconsistent with the VMD model, which would require the adjustment of the parameter ϵ to 0.19, in disagreement with the value of 0.08 determined from lower-energy data. A new model of J/ψ photoproduction, based on perturbative QCD convoluted with a gluon distribution having a strong low-x contribution, matches the fast rise of the cross section. This is in good agreement with other studies at H1 indicating a strong low-x gluon distribution. The t distribution of the J/ψ events is consistent with a diffractive production mechanism, and is also consistent with lower-energy data. The new data are not sufficient to make a statement about the effect known as shrinkage.

Given the recent results from H1 on the total photoproduction cross section and ρ photoproduction, both of which are consistent with VMD, these new results on the J/ψ are intriguing. The production of J/ψ is a different situation in that it involves heavy charm quarks instead of light quarks. One way to resolve the discrepancy between the various results is to postulate the existence of a second soft pomeron which would begin to contribute to the production cross section at high energies and the high mass scale of the J/ψ. This can be validated by examining the t distribution in the high-t region. With sufficient statistics, a second pomeron would show up as a change in the slope of the distribution at some transitional value. The current data are inadequate for this, however.

In spite of the success of the digluon model in explaining the J/ψ data, it is a relatively new model, and there is some disagreement as to its application. Also, questions remain about issues such as its absolute normalization. However, it is clear that perturbative QCD models will continue to evolve and be developed. These models may ultimately be proved or disproved based on predictions such as the shape of the Q^2 distribution in J/ψ production. Again, the data is currently insufficient to address these questions.

It may be that there exists a completely non-perturbative explanation for the entire photoproduction data set. Conversely, it may turn out that a perturbative QCD model can be extended to lower mass scales to explain all of the data. This is somewhat appealing, as it makes the pomeron a more familiar object, something made from the standard roster of QCD players, rather than having it remain an enigmatic, mathematical entity. More likely than these two cases, barring a minor revolution in thinking about the pomeron, will be some compromise between the two competing models, with the J/ψ data being explained by some combination of perturbative and non-perturbative mechanisms. Only investigation of higher-statistic data sets will resolve the issue.

Bibliography

[1] J. J. Aubert *et al.*, *Experimental Observation of a Heavy Particle J*, Phys. Rev. Lett. 33 (1974) 1404

[2] J.-E. Augustin *et al.*, *Discovery of a Narrow Resonance in e^+e^- Annihilation*, Phys. Rev. Lett. 33 (1974) 1406

[3] S. L. Glashow, J. Iliopoulos, and L. Maiani, , Phys. Rev. D2 (1970) 1285

[4] E401 Collaboration, M. Binkley *et al.*, *J/ψ Photoproduction from 60 to 300 GeV/c*, Phys. Rev. Lett. 48 (1982) 73–76

[5] E401 Collaboration, M. Binkley *et al.*, *ψ' Photoproduction at a Mean Energy of 150 GeV*, Phys. Rev. Lett. 50 (1983) 302–305

[6] E516 Collaboration, B. H. Denby *et al.*, *Inelastic and Elastic Photoproduction of J/ψ (3097)*, Phys. Rev. Lett. 52 (1984) 795–798

[7] NA-14 Collaboration, R. Barate *et al.*, *Measurement of J/ψ and ψ' Real Photoproduction on Lithium-6 at a Mean Energy of 90 GeV*, Z. Phys. C33 (1987) 505–512

[8] E687 Collaboration, P. L. Frabetti *et al.*, *A Measurement of Elastic J/ψ Photoproduction Cross Section at Fermilab E687*, Phys. Lett. B316 (1993) 197–206

[9] BFP Collaboration, A. R. Clark *et al.*, *Observation of J/ψ(3100) Production by 209-GeV Muons*, Phys. Rev. Lett. 43 (1979) 187–190

[10] BFP Collaboration, A. R. Clark *et al.*, *Polarization of Muoproduced J/ψ(3100)*, Phys. Rev. Lett. 45 (1980) 2092–2095

[11] The European Muon Collaboration, J. J. Aubert *et al.*, *Measurement of J/ψ Production in 280 GeV/c μ^+ Iron Interactions*, Phys. Lett. B89 (1980) 267–270

[12] The European Muon Collaboration, J. J. Aubert *et al.*, *Production of Charmonium in 250 GeV μ^+-Iron Interactions*, Nucl. Phys. B213 (1983) 1–30

[13] New Muon Collaboration, D. Allasia *et al.*, *Inelastic J/ψ Production in Deep Inelastic Scattering from Hydrogen and Deuterium and the Gluon Distribution of Free Nucleons*, Phys. Lett. B258 (1991) 493–498

[14] The European Muon Collaboration, J.. Ashman *et al.*, *Muoproduction of J/ψ and the Gluon Distribution of the Nucleon*, Z. Phys. C56 (1992) 21–28

[15] New Muon Collaboration, M. Arneodo *et al.*, *Quasielastic J/ψ Muoproduction from Hydrogen, Deuterium, Carbon, and Tin*, Phys. Lett. B332 (1994) 195–200

[16] S. D. Holmes, W. Lee, and J. E. Wiss, *High-Energy Photoproduction of Charmed States*, Ann. Rev. Nucl. Part. Sci. 35 (1985) 397–454

[17] ZEUS Collaboration, M. Derrick *et al.*, *Measurement of the Cross Section for the Reaction $\gamma p \to J/\psi p$ with the ZEUS Detector at HERA* Phys. Lett. B350 (1995) 120–134

[18] H1 Collaboration, S. Aid *et al.*, *Elastic and Inelastic Photoproduction of J/ψ Mesons at HERA*, Nucl. Phys. B472 (1996) 3–31

[19] F. Jacquet and A. Blondel, *An ep Facility for Europe*, Proceedings, Hamburg (1979), ed. U. Amaldi, also in preprint form, DESY report 79-48 (1979) 391

[20] A. Donnachie and P. V. Landshoff, *Exclusive Vector Meson Production at HERA*, Phys. Lett. B348 (1995) 213–218

[21] J. J. Sakurai, *Vector-Meson Dominance and High-Energy Electron-Proton Inelastic Scattering*, Phys. Rev. Lett. 22 (1969) 981–984

[22] P. D. B. Collins, *Introduction to Regge Theory & High Energy Physics*, Cambridge University Press (1977)

[23] H. J. Lipkin and F. Scheck, *Quark Model for Forward Scattering Amplitudes*, Phys. Rev. Lett. 16 (1966) 71–75

[24] A. Donnachie and P. V. Landshoff, *pp and $\bar{p}p$ Elastic Scattering*, Nucl. Phys. B231 (1984) 189–204

[25] A. Donnachie and P. V. Landshoff, *Total Cross Sections*, Phys. Lett. B296 (1992) 227–232

[26] Donald H. Perkins, *Introduction to High Energy Physics, Third Edition*, Addison-Wesley Publishing Company, Inc. (1987) 124–137

[27] Donald H. Perkins, *Introduction to High Energy Physics, Third Edition*, Addison-Wesley Publishing Company, Inc. (1987) 138–142

[28] Donald H. Perkins, *Introduction to High Energy Physics, Third Edition*, Addison-Wesley Publishing Company, Inc. (1987) 271–274

[29] M. G. Ryskin, *Diffractive J/ψ Electroproduction in LLA QCD*, Z. Phys. C57 (1993) 89–92

[30] S. Brodsky *et al.*, *Diffractive Leptoproduction of Vector Mesons in QCD*, Phys. Rev. D50 (1994) 3134–3144

[31] E. L. Berger and D. Jones, *Inelastic Photoproduction of J/ψ and Υ by Gluons*, Phys. Rev. D23 (1981) 1521–1530

[32] H. Jung, G. A. Schuler, and J. Terron, *J/ψ Production Mechanisms and Determination of the Gluon Density at HERA*, Int. J. Mod. Phys. A7:32 (1992) 7955–7988

[33] H. Jung, D. Krücker, C. Greub, and D. Wyler, *Relativistic Corrections to Photoproduction of J/ψ*, Z. Phys. C60 (1993) 721–729

[34] J. A. M. Vermaseren, *Two-Photon Processes at Very High Energies*, Nucl. Phys. B229 (1983) 347–371

[35] H1 Collaboration, I. Abt *et al.*, *The H1 Detector at HERA*, DESY report 93-103 (1993) and DESY report H1-96-01, to be submitted to Nucl. Instr. and Meth. A

[36] The H1 Calorimeter Group, B. Andrieu *et al.*, *The H1 Liquid Argon Calorimeter System*, Nucl. Instr. and Meth. A336 (1993) 460–498, also available in preprint form, DESY report 93-078 (1993)

[37] J. Bán *et al.*, *The H1 Backward Calorimeter BEMC and its Inclusive Electron Trigger*, DESY report 95-177 (1995) submitted to Nucl. Instr. and Meth. A

[38] J. Ebert, *The H1 - Tail Catcher, Hardware and Software Performance*, H1 note H1-08/95-448

[39] T. Wolff *et al.*, *A Drift Chamber Track Finder for the First Level Trigger of the H1 Experiment*, Nucl. Instr. and Meth. A323 (1992) 537–541

[40] S. Eichenberger *et al.*, *A Fast Pipelined Trigger for the H1 Experiment Based on Multiwire Proportional Chamber Signals*, Nucl. Instr. and Meth. A323 (1992) 532–536

[41] T. Carli *et al.*, *Performance of the H1 LAr Trigger in 1994*, DESY report 95-445

[42] H. Jung, *Monte Carlo Generator EPJPSI for J/ψ Mesons in High Energy Electron Proton Collisions*, Proceedings of the HERA Workshop, Vol. 3 (1991) 1488–1496

[43] T. Sjöstrand and M. Bengtsson, *The Lund Monte Carlo for Jet Fragmentation and e^+e^- Physics - JETSET Version 6.3 - An Update*, Comp. Phys. Comm. 43 (1987) 367–379

[44] S. P. Baranov, O. Dünger, H. Shooshtari, and J. A. M. Vermaseren, *LPAIR - A Generator for Lepton Pair Production*, Physics at HERA, Proceedings of the Workshop, Vol. 3 (1991) 1478–1482

[45] A. D. Martin, W. J. Stirling and R. G. Roberts, *Parton Distributions Updated*, Phys. Lett. B306 (1993) 145–150, and *Erratum*, Phys. Lett. B309 (1993) 492

[46] A. D. Martin, W. J. Stirling and R. G. Roberts, *Pinning Down the Glue in the Proton*, Phys. Lett. B354 (1995) 155–162

[47] Particle Data Group, M. Aguillar-Benitez *et al.*, *Review of Particle Properties*, Phys. Rev. D50 (1994) 1173

[48] M. G. Ryskin, R. G. Roberts, A. D. Martin, and E. M. Levin, *Diffractive J/ψ Photoproduction as a Probe of the Gluon Density*, preprint hep-ph/9511228